Investigation of Water Permeation through Molecular Sieve Particles in Thin Film Nanocomposite Membranes

by

Pinar Cay Durgun

A Dissertation Presented in Partial Fulfillment
of the Requirements for the Degree
Doctor of Philosophy

Approved October 2018 by the
Graduate Supervisory Committee:

Mary Laura Lind, Chair
Jerry Y. S. Lin
Matthew D. Green
Dong Kyun Seo
Sefaattin Tongay

ARIZONA STATE UNIVERSITY

December 2018

ABSTRACT

Nanoporous materials, with pore sizes less than one nanometer, have been incorporated as filler materials into state-of-the-art polyamide-based thin-film composite membranes to create thin-film nanocomposite (TFN) membranes for reverse osmosis (RO) desalination. However, these TFN membranes have inconsistent changes in desalination performance as a result of filler incorporation. The nano-sized filler's transport role for enhancing water permeability is unknown: specifically, there is debate around the individual transport contributions of the polymer, nanoporous particle, and polymer/particle interface. Limited studies exist on the pressure-driven water transport mechanism through nanoporous single-crystal nanoparticles. An understanding of the nanoporous particles water transport role in TFN membranes will provide a better physical insight on the improvement of desalination membranes.

This dissertation investigates water permeation through single-crystal molecular sieve zeolite A particles in TFN membranes in four steps. First, the meta-analysis of nanoporous materials (e.g., zeolites, MOFs, and graphene-based materials) in TFN membranes demonstrated non-uniform water-salt permselectivity performance changes with nanoporous fillers. Second, a systematic study was performed investigating different sizes of non-porous (pore-closed) and nanoporous (pore-opened) zeolite particles incorporated into conventionally polymerized TFN membranes; however, the challenges of particle aggregation, non-uniform particle dispersion, and possible particle leaching from the membranes limit analysis. Third, to limit aggregation and improve dispersion on the membrane, a TFN-model membrane synthesis recipe was developed that immobilized

the nanoparticles onto the support membranes surface before the polymerization reaction. Fourth, to quantify the possible water transport pathways in these membranes, two different resistance models were employed.

The experimental results show that both TFN and TFN-model membranes with pore-opened particles have higher water permeance compared to those with pore-closed particles. Further analysis using the resistance in parallel and hybrid models yields that water permeability through the zeolite pores is smaller than that of the particle/polymer interface and higher than the water permeability of the pure polymer. Thus, nanoporous particles increase water permeability in TFN membranes primarily through increased water transport at particle/polymer interface. Because solute rejection is not significantly altered in our TFN and TFN-model systems, the results reveal that local changes in the polymer region at the polymer/particle interface yield high water permeability.

To my family, for their love, support, and patience

ACKNOWLEDGMENTS

First and foremost, I would like to thank my Ph.D. advisor, Dr. Mary Laura Lind who has given me the opportunity to pursue my graduate studies. I am grateful for her support, enthusiasm, and guidance over the years. Her endless energy, positive attitude, working discipline, and exceptional mentorship significantly helped me to conclude my studies.

I also would like to acknowledge my committee members, Dr. Jerry Lin, Dr. Matthew Green, Dr. Don Seo, and Dr. Sefaattin Tongay, for their time, valuable feedback and insight regarding my research.

During my studies, I used a variety of equipment from different labs, which were instrumental in my research. Therefore, I would like to individually thank Dr. Jerry Lin, Dr. Paul Westerhoff, Dr. Lenore Dai, Dr. Don Seo, and Dr. Francois Perreault for granting me access to furnace, Dynamic Light Scattering, Thermal Gravimetric Analysis, and high-speed centrifuge instruments.

I gratefully acknowledge the use of facilities in the LeRoy Eyring Center for Solid State Science at Arizona State University for atomic force microscopy and high-resolution X-ray diffraction instrument and the Biodesign Institute at ASU for the use of facilities for Fourier Transforms Infrared, contact angle, and oxygen plasma instruments.

Also, I would like to thank our lab manager Fred Pena for his outstanding help about technical issues over the years. He was always there with a practical solution, whenever needed.

I would like to acknowledge all of the members of Dr. Lind's research group; Heather Jamieson, Tianmiao Lai, Afsaneh Khosravi, Huidan Yin, Stewart Mann, Shawn Fink, John Konecny, Cailen McCloskey, Andrew Shabilla, Tony Nguyen, Alex Maltagliati, Sofia Herrera, Wendy Lin, Andrea Kraetz, and my other colleagues Yi Yang, Ana Barrios, and Bohan Shan for their contributions and support.

Moreover, I would like to thank the Turkish friends in Arizona for being my family away from home. Especially, I will always graciously remember the support of Ayse Gundogdu Senturk, Burhan Senturk, Filiz Kula, Irfan Kula, Gozde Bicer, Alpay Bicer, Cigdem Topcu Uzer, Cengiz Uzer, Aysegul Demirtas, Kerem Demirtas, Didem Yamak, Basak Cetegen, Edvin Cetegen. I would like thank Ezgi, Alp, Selin, Ada, Lina, Deniz for bringing happiness to our lives.

I would like to thank my friends Gulay Oskay, Seda Coskun, Gulbin Aysi Alan, Zeynep Karakaya, Zeynep Sezer, Feride Erdogdu, and Enes Bahar for their long-distance support, and proving that time and distance is not that important for friendship.

Last but not the least; I would like to thank my family Ahmet, Semra, Sevim, Hikmet, Necdet, Sema, Ezgi, and Elif, for always motivating me to explore further. I greatly appreciate their patience, understanding, and sacrifice. I would like to utter my gratitude to my beloved husband, Ahmet Cemal Durgun, I could not have started and completed this study without him.

This work supported by National Science Foundation CAREER award CBET-1254215, National Science Foundation Nanosystems Engineering Research Center for Nanotechnology-Enabled Water Treatment (ERC-1449500) and ASU Graduate College Completion Fellowship.

TABLE OF CONTENTS

Page

CHAPTER Page

LIST OF TABLES

Table Page

LIST OF FIGURES

Figure Page

Figure Page

Figure Page

Figure Page

1. INTRODUCTION AND BACKGROUND

1.1. Pressure-driven membrane desalination: Reverse osmosis

Membranes are porous or dense; organic/inorganic/hybrid barrier materials which can separate phases by selectively allowing passage of penetrants with the application of driving forces such as concentration, pressure, temperature, and electric potential gradients [1]. Water treatment and desalination systems commonly use membrane separation processes because of the mechanical simplicity (compact, modular, scalable systems), high energy efficiency, and low environmental impact. Ultrafiltration (UF), microfiltration (MF), nanofiltration (NF), and reverse osmosis (RO) techniques are the typically employed pressure-driven membrane separation methods for water treatment to remove particles and dissolved contaminants, Figure 1 presents a schematic summary [2]. These processes can separate a wide range of materials from the feed solution with the application of pressure on the feed side of the membrane, then the purified solution (called the permeate) permeates through the membrane while the concentrated solution (called the retentate) is retained on the feed side of the membrane. These processes differ in membrane pore size, separation principles, and applied pressure range which are characterized by the size of rejected materials. There is a spectrum of potential separation applications for these membranes. Commonly, UF membranes have pore sizes of 2–100 nm and MF membranes have pore sizes of 100–10000 nm. UF and MF processes separate based on sieving of different size particles (macromolecules to suspended particles) through the membrane pores in various water applications at low pressures (0.1–5 bar and 0.1–2 bar). NF processes can reject dissolved compounds including multivalent ions mostly based on sieving and charge effects through the small pores

(0.5–2 nm) in the charged membranes at moderate pressure (3–20 bar). Lee et al. and Van der Bruggen et al. reviewed the details of pressure-driven membrane processes in water purification [2, 3].

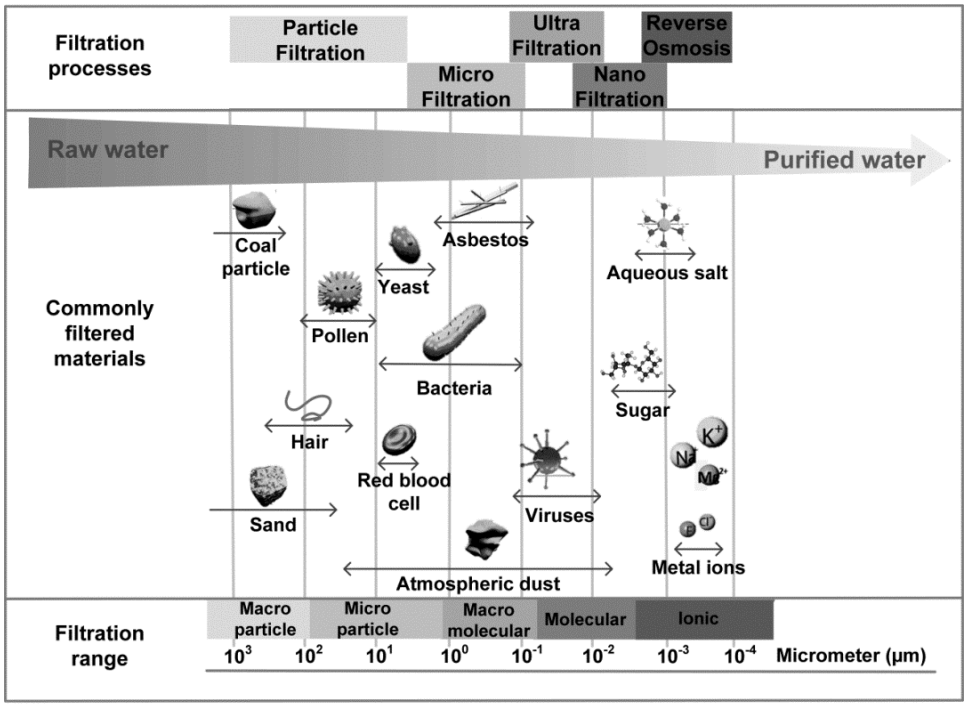

Figure 1: Membrane filtration spectrum for water separation and purification.
The image depicts the conventional particle filtration, microfiltration (MF), ultra-filtration (UF), nanofiltration (NF), and reverse osmosis (RO) and their filtration ability (images represent typically filtered materials) with required average pore sizes of the membrane (at the bottom). There is no clear distinction between MF and UF, UF and NF, and NF and RO. Adapted from Lee et al. [2].

Reverse osmosis is the pressure-driven membrane separation technique in which a dense (considered as essentially non-porous) membrane preferentially permeates water and primarily rejects dissolved salts (including monovalent ions such as sodium and chloride) from pressurized saline sources (such as brackish water and seawater) at applied hydraulic pressure (5–120 bar). Currently, RO is the primary technology for water

desalination owing to inherent lower energy consumption and higher efficiency compared to already available thermal-driven water desalination techniques (in which an energy-intensive phase transition from liquid to vapor occurs) such as multistage flash distillation (MSF) and multi-effect distillation (MED) [4, 5]. In some cases, thermal-driven systems are more feasible because of low thermal energy costs (e.g., geothermal sources or abundant fuels). Moreover, the energy-efficiency of MED and MSF thermal desalination systems can be increased over the individual system by coupling into a hybrid system with RO [5]. However, RO will remain the dominant desalination technique in the near future because of the globally increasing interrelated nature of energy and water demand [6]. There are other types of membrane separation techniques, as well, that are emerging for desalination based on different separation principles [7]. For example, concentration as driving force, forward osmosis (FO) [8] and pervaporation [9]; thermally-driven, membrane distillation (MD) [10, 11] (involves no net phase transition); and electrically-driven, electrodialysis (ED) [12]. Despite the recent advancements in these membrane technologies, currently, they are mostly considered the complementary method to enhance the RO desalination efficiency or applicable when RO desalination fails [13-17] Comprehensive reviews about reverse osmosis desalination status can be found in [5, 7, 18, 19].

1.2. Water and salt transport in an RO membrane

The solution-diffusion theory is the widely accepted phenomenological model in osmotic separation processes to explain water and ion transport through the dense membrane (refer to [20] for experimental verification of this model and [21] for the other transport models). The model considers the membrane as a “black-box” (which describes

the transport regarding membrane performance results) assuming homogeneous and non-porous membrane morphology [21]. According to this model, (1) molecules dissolve in the membrane from the high chemical potential polymer-feed interface (feed side), (2) afterwards, diffuse across the membrane independently because of the individual chemical potential gradient, and (3) desorb from the polymer at the polymer-permeate side, into the low chemical potential permeate, as depicted in Figure 2 and in detail in Figure 3. In general, in the solution-diffusion model, permeability is described as a function of the solubility and diffusivity of the components within the membrane material.

Figure 3 shows the pressure, *P*, chemical potential, μ, and the concentration profile, C, for the water and the salt transport by the solution-diffusion mechanism to summarize the water and salt transport mechanism. The solution-diffusion model assumes the pressure within the membrane is uniform. Therefore, there is a pressure discontinuity on the membrane surface at the low-pressure side (permeate side). The chemical potential gradient occurs owing to concentration and pressure difference across the membrane [21]. The discontinuity of the applied pressure on the different side of the membranes creates a concentration difference for water which is the driving force for water transport (Fickian diffusion) [22]. However, the salt concentration difference between the sides of the membranes creates the concentration difference across the membrane which is the driving force for salt transport (Fickian transport) [22]. The salt transport, unlike water transport, does not significantly affected by the applied pressure difference [20]. The concentration of water and salt components at the feed side of the

membrane surface C_{w0}^{s} and C_{s0}^{s} can be higher or lower than the concentration inside the membrane C_{w0}^{m} and C_{s0}^{m} [21].

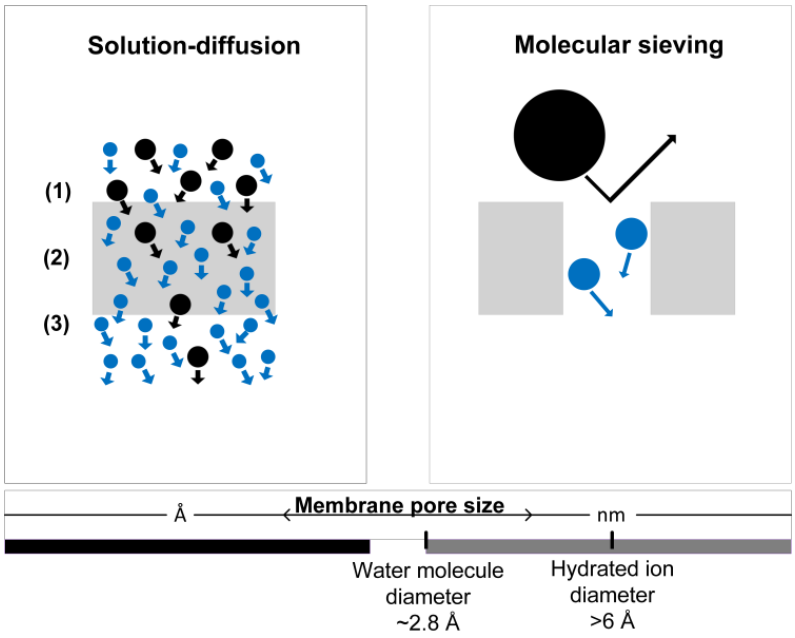

Figure 2: Solution-diffusion and molecular sieving transport mechanisms.
In the solution-diffusion mechanism, ions/molecules transport based on their diffusivity and solubility in the dense membrane. In the molecular sieving mechanism, ions/molecules transport based on the ability of molecular diffusion through the pores. The bottom scale shows the relative membrane pore sizes, water, and hydrated ion diameters. Adapted from Wang et al. [23].

The model may explain the water flux (J_w) and the salt flux (J_s) at steady-state as follows, refer to [20] for fundamentals about the equations:

$$J_w = \frac{D_w}{L}\hat{V}_w \Delta C_w^m = \frac{P_w}{L}(\Delta P - \Delta\pi) = \mathbf{A}(\Delta P - \Delta\pi) \qquad \text{Equation (1.1)}$$

$$J_s = \frac{K_s D_s}{L}\Delta C_s^s = \frac{P_s}{L}\Delta C_s^s = \mathbf{B}\Delta C_s^s \qquad \text{Equation (1.2)}$$

Here, in equation (1.1), D_w is the effective water diffusion coefficient, $\hat{V}_w$ is the specific volume of water, ΔC_w^m is the sorbed water concentration difference in the

membrane between the feed side (C_{w0}^{m}) and the permeate side (C_{wL}^{m}), P_w is the hydraulic water permeability, A is the water permeance (in reverse osmosis membrane literature, it is called the water permeability coefficient), L is the membrane thickness, ΔP and $\Delta\pi$ are the pressure and osmotic pressure differences across the membrane. In equation (1.2), K_s is the salt sorption coefficient, D_s is the salt diffusion coefficient, P_s is the salt permeability, B is the salt permeance, and ΔC_s^s is the salt concentration difference of the solutions at the feed side (C_{s0}^{s}) and at the permeate side (C_{sL}^{s}).

A and B values (in equations 1.1 and 1.2) are the critical material properties for evaluating an RO membrane material. They indicate how fast molecules can pass through the membrane material (A/B ratio, the water-salt perm-selectivity, should be high for desalination). Although A and B values are the primarily reported values to define RO membrane desalination performance, the values are membrane thickness dependent. A/B, P_w and P_s are the intrinsic membrane properties which are independent of membrane thickness.

Another important parameter related to selectivity is the apparent salt rejection in desalination literature. It measures the separation ability of a desalination membrane. However, it is not an intrinsic material property; it can change based on operating conditions such as pressure and feed concentration [20]. The apparent (observed) salt rejection, R, is defined as:

$$\mathbf{R} = \left(1 - \frac{C_{sL}^{s}}{C_{s0}^{s}}\right) \text{x } 100\% = \left(\frac{A/B\ (\Delta P - \Delta\pi)}{1 + A/B\ (\Delta P - \Delta\pi)}\right) \text{ x } 100\% \qquad \text{Equation (1.3)}$$

The real membrane salt rejection can be higher because of the salt concentration polarization on the membrane surface [24]. Models for significant concentration polarization can be found in [25, 26]; at low salinity and pressure, the effect of concentration polarization can be negligible.

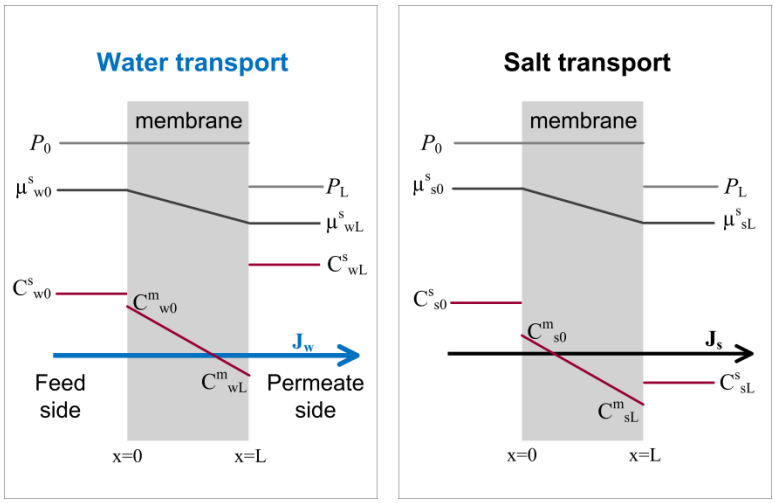

Figure 3: Water and salt transport by the solution-diffusion mechanism.
The image shows the profiles of hydraulic pressure, *P*, chemical potential, μ, and concentration, C. The superscripts s and m represent solution and membrane. The first subscripts w and s are for water and salt. The following subscripts 0 and L refer to the feed and permeate side of the membrane. Adapted from [20].

The separation occurs based on solubility and diffusivity rate differences of permeates in the membrane material [21]. The solubility of the solutes (typically sodium, chloride, magnesium, calcium) and the solvent (typically water) depends on the molecular structure, membrane porosity, and chemical affinity [23]. The diffusivity occurs by the thermally-stimulated rearrangements of the polymer chains which facilitates transport of small size molecules [23]. The water solubility in the commonly used hydrophilic polymer membranes is high so that the diffusivity is mostly the limiting

step for the water permeability. Crosslinking degree of the polymer can prevent the dissolution of the polymer, and flexible polymer chains can enhance the diffusion in the polymer [1]. Thus the model shows the membrane structure profoundly affects the transport properties.

The well-known upper bound, the Robeson plot [27], indicates the limit of a polymeric membrane material for an improved transport property regarding both permeability and selectivity, see Figure 4 (a) for gas separations. At the upper-bound region, tighter polymer chains result in decreasing permeability because of the decreasing diffusion coefficient, however, increasing selectivity [27]. Therefore, at the boundary region, more selective membrane materials generally exhibit lower permeability and vice versa, often called the permeability-selectivity trade-off. Further analysis of the upper bound revealed that the separation mechanism might transit from solution-diffusion to Knudsen diffusion for gas separation membranes on the upper boundary region [28]. Knudsen diffusion separates species based on their very different molecular weights across the porous membrane, and is primarily used to describe gas transport in porous membranes; therefore, in the case of possible transit to Knudsen diffusion at the upper bound, this may indicate the membrane is no longer a dense structure and may have pores or defects. Other studies showed similar trade-off relations existence for desalination membranes [22, 29], Figure 4(b) depicts the upper bound plot for desalination membranes. Thus, the solution-diffusion governed desalination membranes have an empirical limitation for further perm-selectivity improvement. Incorporation of additional transport mechanisms, such as molecular sieving, may overcome the trade-off [23]. Also, Chen at al. recently proposed interfacial salt sieving effects using nanoporous carbon

composites [30] and Shen et al. recently proposed channel-based size exclusion using artificial water channels [31] for overcoming the perm-selectivity trade-off.

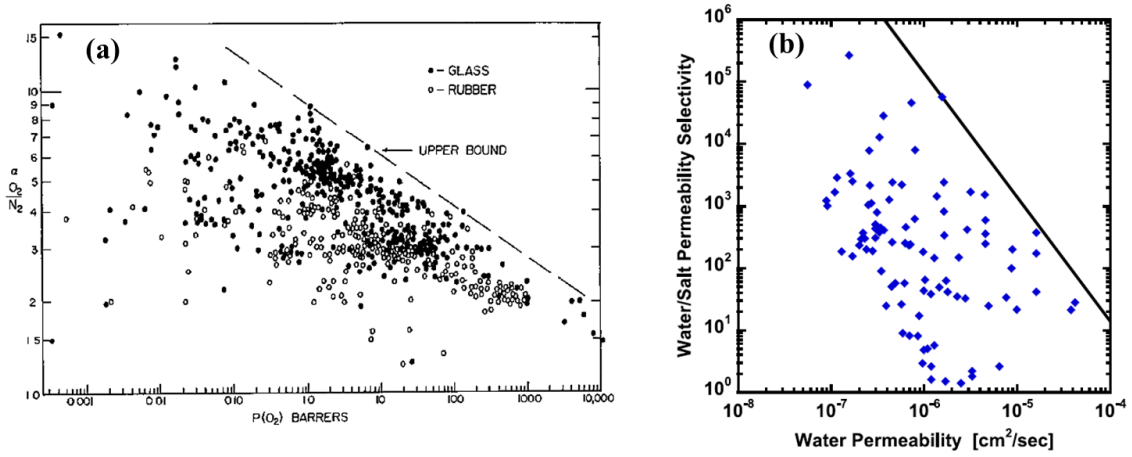

Figure 4: The upper bound plots for gas separation (a) and desalination (b).
(a) (reproduced from Robeson [27]) shows the oxygen/nitrogen selectivity as a function of oxygen permeability and (b) (reproduced from Zhang and Geise [29]) shows the water/salt selectivity to water permeability. Both plots exhibit similar empirical upper bound relations.

Molecular sieving transport mechanism separates species depending on their molecular sizes through pores within the molecular size range, as shown in Figure 2. In this mechanism, the pores allow particles smaller than the pore size to pass and sterically reject particles larger than the pore size. The inclusion of this mechanism in desalination membranes may provide a path for highly selective and highly permeable membranes [32]. For an effective desalination performance, the pore size should be between the diameter of a water molecule (~2.8 Å) and diameter of hydrated ions (typically >6 Å) [33] which can be ~5.5 Å [34]. In water desalination, the size of the nanopores largely determines the water transport (surface property, pore geometry, and pore network also play a significant role in the transport) whereas electrostatic interactions, coordination

with functional groups and charges at the pore edge, and the steric exclusion influence the hydrated ion transport [23]. Theoretically, membranes with uniform, defect-free nano-pores within desalination range can show almost complete salt rejection and can exhibit substantially higher water permeability than the state-of-the-art reverse osmosis membranes. For example, Liu and Chen performed molecular dynamics (MD) simulations for reverse osmosis water transport through single crystal FAU and MFI zeolite membranes and determined the water permeability for 3.5 nm thick membranes on the order of 10 $\mu m^2\ MPa^{-1}\ s^{-1}$ with almost 100% salt rejection [35]. However, there is a discrepancy between the results of simulation and experimental studies for nanoporous zeolite membranes. Experimentally, nanoporous zeolite membranes (i.e., MFI, NaA) exhibited good salt rejection but lower water permeability (0.04—0.1 $\mu m^2\ MPa^{-1}\ s^{-1}$) than commercial polyamide RO membranes (0.6—2 $\mu m^2\ MPa^{-1}\ s^{-1}$) [36]. Fasano et al. proposed that the intracrystalline pore structure (the structure of the pore, not the structure between different polycrystalline grains) in zeolite and surface barriers (pore blockages and/or narrowing) creates significant resistance for water transport [37]. This can lead to large differences between the predictions with MD simulations and experimental results for the water permeability through the nanoporous zeolite membranes [37].

1.3. Thin film composite membrane

Reverse osmosis processes widely use dense, interfacially polymerized (IP) aromatic polyamide (PA) thin film composite (TFC) membranes. The polymerization reaction is a condensation reaction at the interface of an amine in the aqueous phase and acid chloride in the organic phase on microporous support [38]. Figure 5(a) depicts the IP

reaction using the commonly used monomers for TFC synthesis. The polymerization conditions such as the type, concentration, and temperature of the phases, chemical contact time, membrane curing and post-treatment methods, and support conditions profoundly affect the separation performance of the resulting membrane [39-41]. In general, the dense PA active layer TFC membrane structure is highly salt selective (salt rejections are typical >98%) and very thin (~100 nm) which enables high water permeance (1-10 $lm^{-2}h^{-1}bar^{-1}$ (lmh bar^{-1})) [42]. Figure 5(b) depicts the thin film structure. The active layer is so thin it is complicated to synthesize it freestanding; therefore, the characterization of the transport mechanism and structure/property relation is challenging [20]. Studies are ongoing to understand further and improve the polyamide membrane structure. Moreover, as discussed above transport mechanisms, the performance of these membranes in desalination applications is currently limited by an "upper bound." The trade-off inherent in polymeric membranes constrains the maximum performance of these membranes for desalination [22]. Furthermore, the polyamide membranes are susceptible to surface damage inevitably from biological/organic/colloidal fouling and scaling (the precipitation or crystallization of inorganic minerals ions), and free chlorine (the most common, low-cost, effective disinfection agent for water treatment) [43, 44]. There are ongoing studies on monitoring, controlling, and minimizing the fouling and scaling by optimizing the feed pretreatment, membrane cleaning, and operational conditions, and enhancing the membrane anti-fouling/scaling properties through surface modifications and nanomaterials [44-47]. However; the polyamide structure degrades after continuous exposure to trace amounts of chlorine, the PA (at amounts three orders of magnitude lower than the effective chlorine present in disinfected water [43]). The ongoing studies

are tuning the polyamide structure for chlorine resistant; surface coating, surface grafting, adding nanoparticles/nanosheets and exploring new chlorine-resistant monomers/polymer [48, 49].

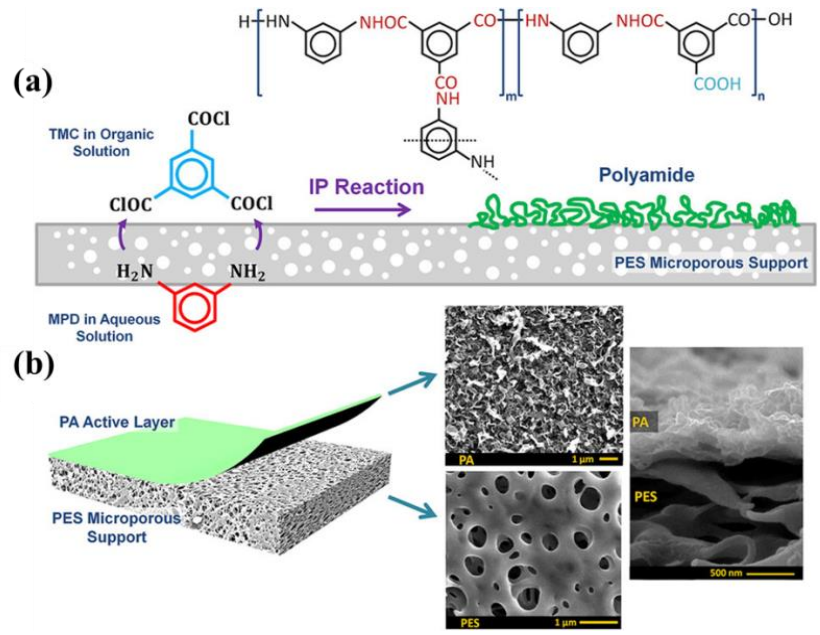

Figure 5: Representation of interfacial polymerization (IP) and thin film composite (TFC) membrane structure.
(a) represents common IP reaction of bifunctional amine monomer in aqueous solution and trifunctional acid chloride in organic solution on a microporous support. The resulting structure is crosslinked polyamide, the polyamide structure in parenthesis m is crosslinked, and n is linear. (b) represents the TFC structure which consists of a thin polyamide active layer on top of the microporous support. The support usually is an ultrafiltration membrane such as microporous polyethersulfone (PES) or microporous polysulfone (PSf) on top of non-woven polyester. The supports have negligible mass transport resistance. However, it has an impact on the resulting polyamide structure and performance [41]. Images show the top views of the active layer (top at the middle) and the porous layer (bottom at the middle), and the cross-section of the membrane (at the right). The figure is taken from Khorsidi et al. [50].

1.4. Thin film nanocomposite membranes

Mixed matrix membranes (MMMs), in which an inorganic filler phase is dispersed in a continuous polymer phase, are promising alternatives to pure polymeric

membranes to address the upper bound problem [51] and bring additional functionalities such as antimicrobial and chemical resistance [52] and heat generation using sunlight [53]. Ideally, the MMM exhibits the desirable characteristics of each component and eliminates their disadvantages. Thin film nanocomposite (TFN) membranes add nanoparticles into the thin polyamide film of the TFC membrane structure during the interfacial polymerization process; TFN membranes were named after the seminal MMM study by Hoek's group for RO desalination in 2007 [54]. The cross-section images of the TFC and TFN membranes for this study are reproduced in Figure 6 (a) and (b), to indicate the place of the particles in the thin polyamide structure. Recent TFN studies have demonstrated improved membrane performance results for water treatment, in which embedded nanoparticles were zeolite [54-61], carbon nanotubes [62-65], silica [66-68], silver [62], metal oxides [69]. However, the performance of TFN membranes varies as a function of the type, size, and concentration of nanoparticles. In addition, there may be some "non-ideal effects" [70] in membranes such as particle aggregation within the polymeric matrix [71] which may reduce membrane selectivity, and the non-selective void or rigidified polymer formation at the polymer/particle interface [70] which may reduce membrane stability, as well as membrane performance.

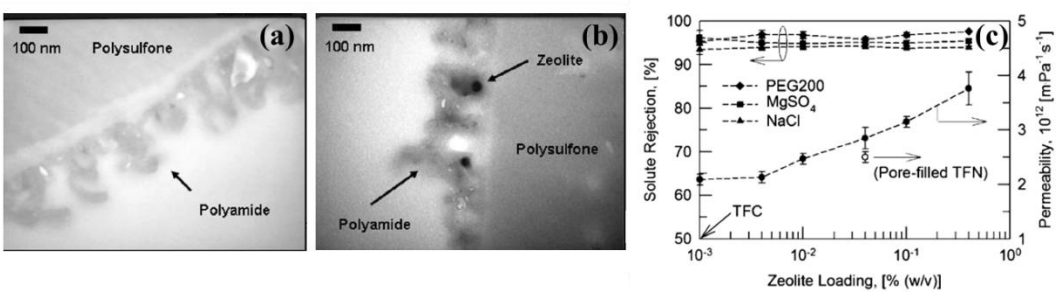

Figure 6: The cross-section images of TFC (a) and TFN membranes (b), and the plot for the effect of zeolite loading on the separation performance of the membranes (c).
The images and the plot are taken from [54].

The super-hydrophilic, molecular sieve Linde type A (LTA) zeolite is a promising candidate for the inorganic filler in TFN membranes. The zeolite has 3-dimensional pores with a diameter of 4.2 Å [72], which is suitable for selecting water, but rejecting hydrated ions and small organic molecules [33, 73]. Also, the 3-D, cubic structure of the LTA pores ensures access to the pore regardless of how the zeolite is oriented in the membrane. Based on the literature [54, 55, 57, 58], polyamide membranes with incorporated LTA nanoparticles have higher flux and similar rejection when compared to commercial membranes.

Recently, we published the long-term separation performance of TFN membranes with 0.15 wt% and 0.30 wt% LTA particles and showed their enhanced, stable desalination performance compared to TFC control membranes [74]. In that study, we synthesized a series of polyamide TFC and TFN membranes, via interfacial polymerization reaction, with different nanoparticle content in the organic casting solution. These membranes were tested for ~3,000 hours in a lab-scale testing system at the United States Bureau of Reclamation's Water Quality Improvement Center in Yuma, AZ. All membranes exhibited relatively stable long-term separation performances. The experimental results showed that TFN membranes with 0.15 wt% LTA content had 1.3 times higher water permeance than the TFC membranes and those with 0.30 wt% LTA content had 1.4 times higher water permeance than the TFC membranes. Moreover, TFN membranes with 0.15 wt% and 0.30 wt% LTA content exhibited 1.4 and 1.8 times higher perm-selectivities than TFC membranes. Figure 7 depicts the water flux, salt rejection, and water-salt permselectivity results of the membranes over time. Our membrane long-term performance data demonstrated that increases in zeolite loading enhanced long-term

separation performance (both water permeance and salt selectivity) for brackish water reverse osmosis desalination. Our results also showed that thin film nanocomposite membranes had stable long-term flux and rejection performance in comparison to thin film composite membranes.

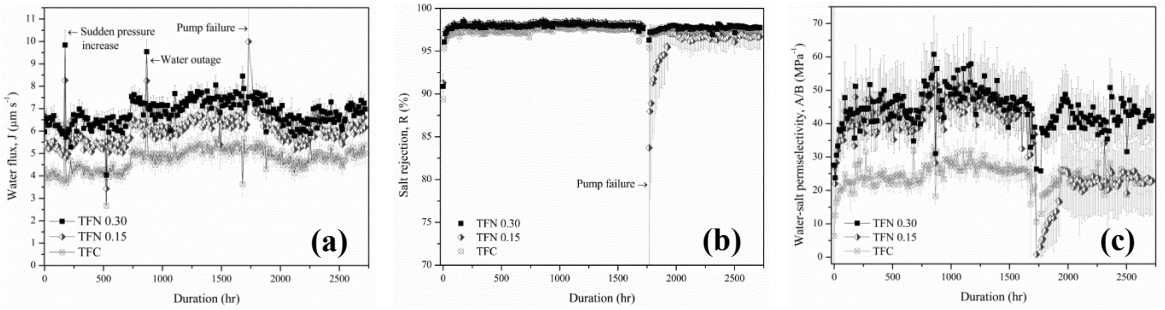

Figure 7: Long-term desalination performance of our TFN membranes.
Average measured performances of TFC, TFN 0.15, and TFN 0.30 membranes under 200 psi. (a) water flux (b) salt rejection (c) water-salt permselectivity. Plots were taken [74].

To understand the water transport of zeolites, Turgman-Cohen et al. performed molecular dynamics simulations for pressure-driven water transport through bulk and thin film membranes of single crystal LTA zeolites simulated with periodic boundary conditions [75]. In that study, the water permeability of the thin film hydrophilic LTA zeolite membrane was estimated as 0.158 μm^2 MPa^{-1} s^{-1}, which is an order of magnitude lower than thin film polyamide membrane permeability [75]. Therefore, they hypothesized that water might preferentially flow around the zeolite particles and not through the zeolite pores in TFN membranes [75]. Another interesting finding of this study was that the water permeability of the particles became stable under high applied pressure, 100 MPa, which is far beyond the pressure range of reverse osmosis (0.5-12 MPa). On the other hand, Jeong et al. hypothesized that the preferential water flow occurs through the zeolite A pores.[54] In the study, they incorporated single-crystal LTA zeolite nanoparticles at various contents into TFN membranes and compared the results

with TFC membranes. Also, they compared the water permeabilities of TFN membranes with a limited study of "pore-closed" and "pore-opened" particles. In pore-closed particles, the templating agent remains inside the central pores of the crystal structure which prevents water flow through internal cages of the zeolite. Their results showed that TFN membranes with pore-opened particles have higher water permeability compared to TFN membranes with pore-closed particles, as shown in Figure 6(c). Hence, they concluded that the zeolite pores provides a preferential water flow pathway. However, this analysis was limited to only one nominal zeolite content of the casting solution and did not control for changes in the different density of pore-close and pore-open particles.

Since the conclusions of these two studies contradict each other, to understand the water transport pathways in TFN membranes, we published an analysis [76] of Cui et al.'s experimental data reported in [77] in the context of published reports on polycrystalline LTA membranes and the Jeong et al.'s experimental data reported in [54], which is also shown in Figure 6(c). In this analysis, instead of modeling transport mechanisms, we focused on quantifying the experimentally measured water flux through the zeolite in aqueous membrane separation applications. We isolated water permeation through the zeolite crystal pores from permeation through the membrane and the polymer-zeolite interface by utilizing a resistance model on the possible transport pathways that are depicted in Figure 8. We estimated the water permeability through the polyamide, through the zeolite pores, around the zeolite to be 0.21±0.11, 81±41, and 95±28 ($\mu m^2\ s^{-1}\ MPa^{-1}$), respectively [76]. Therefore, we hypothesized that the preferential water flow path is both through and around the zeolite particles.

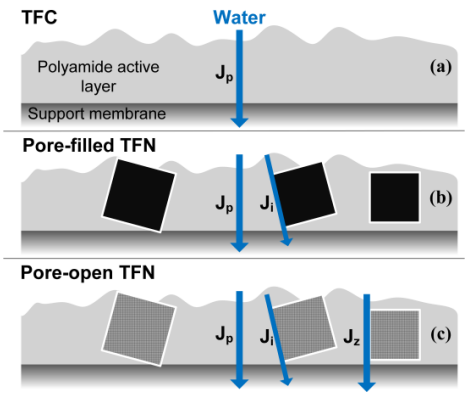

Figure 8: Possible transport pathways through the active layer of membranes.
(a) thin film composite membrane (TFC), (b) thin film nanocomposite (TFN) membranes in which pore-closed zeolites are embedded, and (c) thin film nanocomposite membranes in which pore-opened zeolites are embedded. Polyamide thin film layer (50-200 nm) and zeolite particles (~100 nm) onto the microporous support. The water transport pathways: J_p through polymer; J_i through the polymer-particle interface; and J_z through zeolite pores.

Determining the intrinsic properties of filler particles, the polymer, and the particle/polymer interface are critical to the investigation of MMMs for RO applications. Performance models allow us to design and create improved membranes and explain deviations from the ideal behavior. The reported modeling and the experimental data, and our analysis in [76] may help us to determine the intrinsic properties of each component of TFN membranes. However, in our previous analysis, the utilized experimental data for TFN membranes with pore-closed particles was only at one particle content and size. Moreover, in our analysis, we had five more limitations [76]. We did not know (1) the amount of incorporated zeolite in the tested membrane (we only knew the nominal zeolite content of the casting solution); (2) the extent of particle aggregation above certain loadings; (3) the number of zeolite particles partially covered with a permeable polymer; (4) the water permeance of the polymer after the addition of the particles (e.g., how the polyamide crosslinking structure might change since the particle addition occurs during

the polymerization reaction, the resulting polymer permeance after the particle addition is unknown) (5) the structure of the free-standing polyamide material (because it is very thin). Therefore, in this dissertation, we attempted to address these limitations to investigate the impact of hydraulic water transport of molecular sieve zeolite A in thin film nanocomposite membranes.

1.5. Research goals and experimental plans

The overall goal of this study is to investigate the contributions of the polymer, nanoparticle filler, and polymer/particle interface in TFN membranes for reverse osmosis and to assess experimentally if water permeation occurs in the pores of nanoporous single crystal particles. We aim to overcome the limitations of previous experimental studies and investigate the individual contributions to TFN membrane water transport of porous inorganic single-crystal molecular sieve particles, the polymer/particle interface, and the polymer.

We conducted a recent literature review and analysis to look for any correlations between embedding nanoporous particles in the structure and the performance of TFN membranes (Chapter 2). Also, we performed a TFN experiment to analyze the water permeance of pore-closed (non-porous) and pore-opened (nanoporous) zeolites in TFC membranes synthesized through conventional polyamide-based method (Chapter 3). Figure 8 shows the possible transport pathways through these membranes. The conventional TFN synthesis method is to add particles in the structure during interfacial polymerization [78]. Our experiments described in this dissertation reveal the porous particles' impact on the performance, with some limitations.

Further, we developed two model membrane designs: (1) TFN-model membranes and (2) water impermeable polymer model membranes (Chapter 4).

The first model membrane design is a novel polyamide TFN. In this method, first, we anchored the molecular sieve nanoparticles on the support with a polydopamine polymer adhesion layer. Then, we interfacially polymerized the dense, ultrathin, polyamide onto the polydopamine-particle stabilized layer. Figure 9(a) depicts the possible water transport mechanism in the membranes. This TFN-model synthesis method allows better estimation of the incorporated particle amount. This synthesis also enables easy inclusion of the partially covered particles into the permeability analysis compared to conventional TFN synthesis because we can analyze the particle content of the coated support before the interfacial polymerization reaction. This method provides a more controllable TFN membrane synthesis as opposed to the conventional way where the particles are embedded into the structure during the polymerization reaction. Furthermore, this method enables vigorous dispersion techniques to uniformly disperse the particles on the surface, compared to the conventional TFN synthesis.

For the second model membrane, we developed a water impermeable polymer membrane in which the polymer serves as a continuous matrix material. In this design, theoretically, water transport occurs only through zeolites and/or through the particle-polymer interfaces. In this design, the structure presents a polymer top layer (waterproof), hydrophilic molecular sieve zeolites within the top layer (with or without pore-opened and pore-closed particles), and an adhesion polymer sublayer on a porous support, as shown in Figure 9(b). In both our model membrane designs, we separately studied pore-opened and pore-closed particles in water impermeable and water permeable polymer

matrix. The adhesion polymer layer serves as a matrix material to anchor the zeolites to the porous support membrane. The pore-closed MMM provide information for water permeation through the polymer-zeolite interface, and pore-opened MMM enable us to determine the water permeation through the zeolite pores as well as the polymer-zeolite interface. We confirm the defect-free nature of the model membrane by testing membrane permeability and selectivity in hydraulic filtration. We apply the resistance model to the water permeation results to estimate the individual particle permeability (Chapter 5). With these models and the TFN study, we can determine the zeolite and the interface water permeability, separately.

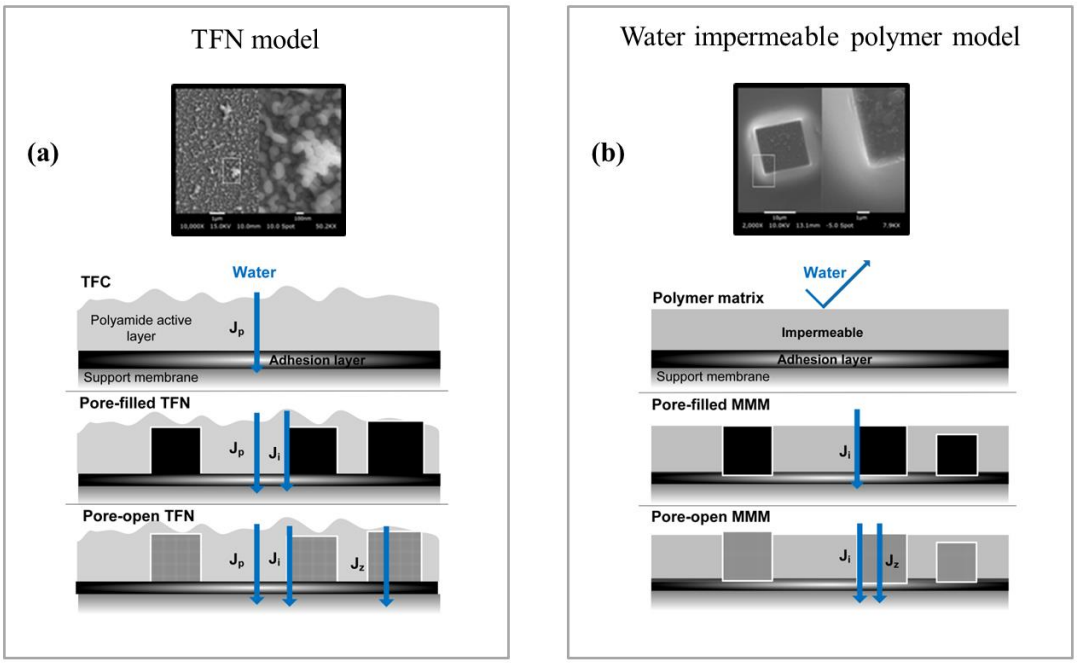

Figure 9: Possible transport pathways through TFN-model membranes (a) and water impermeable polymer model membranes (b).
In both designs, particles stabilized on the support via adhesion layer before the film formation. The water transport pathways: J_p through polymer (for impermeable $J_p = 0$), J_i through the polymer-particle interface, and J_z through zeolite pores. The SEM images show the surface of representative membranes.

1.6. Dissertation overview

Chapter 1, introduces pressure-driven membrane desalination technologies, the water and salt transport mechanism for desalination, the thin film composite, and the thin film nanocomposite membranes. This chapter also includes the motivation for the research on enhancing the performance of the state of the art RO membranes by using molecular sieve particles and the objectives of this study. *Chapter 2* includes a literature review of the nanoporous materials used in TFN membranes with an analysis of their enhancements. *Chapter 3* gives the performance and characterization analysis of polyamide thin film nanocomposite membranes with pore-closed and pore-opened nanoparticles at different sizes to provide an understanding of the effect of nanoporous particles in water transport. *Chapter 4* depicts the development of the model membrane designs, the role of the particle/polymer interface with characterization techniques and performance test results. *Chapter 5* includes the analysis of the zeolite water permeability with the insights from Chapter 3 and Chapter 4. *Chapter 6* provides a summary of the main contributions and future recommendations.

2. LITERATURE REVIEW

2.1. Introduction

The increasing global demand for fresh water drives extensive research to both improve existing water purification techniques and to discover new alternative purification methods. Among available water separation technologies, membrane-based desalination processes are promising to fulfill the increasing water demand because of their inherent high energy efficiency and efficacy and ability to extract water from saline sources [79]. Currently, reverse osmosis (RO) is the primary technology for seawater and brackish water desalination. RO is a pressure-driven membrane separation technique in which a semi-permeable, dense membrane preferentially permeates water and primarily rejects dissolved salts. Nanofiltration (NF) is a similar technique to RO; however, it uses more water permeable/less salt selective – often termed "loose" – membranes under lower pressure. The state-of-the-art, commercially available RO/NF membrane is an asymmetric aromatic polyamide (PA) thin film composite (TFC) produced via interfacial polymerization (IP) on a microporous support membrane. More than four decades have passed since the initial development of the polyamide TFC membrane. However, methods to improve this unique membrane structure and fundamental understanding of the superior mechanism for mass transport are under ongoing investigation in membrane science [50, 80-82]. Nevertheless, the permeability/selectivity trade-off, inherent in polymeric membranes, constrains the maximum performance of these membranes for desalination [29]. Additionally, RO/NF membranes still need improved fouling resistance and chlorine tolerance [42]. Thin film nanocomposite (TFN) membranes, which add nanoparticles into the thin polyamide film of the TFC membrane structure, have emerged to address the challenges over the last decade [78]. In addition to novel functionalities

added by nanoparticles (e.g., antimicrobial, chemical resistance), it is hypothesized that nanoporous particles bring an additional transport mechanism and preferential flow paths through membranes [54]. Here, we review the recent literature from 2015-2017 of nanoporous materials incorporated into TFC polymeric membranes for RO/NF desalination focusing on those that include zeolites, metal-organic frameworks, and graphene-based materials. Beyond the scope of this article, there are many non-porous nanoparticles that can be added to TFC membranes, as well as other types of membranes for desalination processes which incorporate nanoparticles which specific functionalities (e.g., antimicrobial activity, chemical reactivity, and heat generation). For example, Dongare et al. recently developed porous, hydrophobic polymer membranes containing nanophotonic particles for membrane distillation [83]. Furthermore, a recent review summarized the membranes with stimuli-responsive nanoparticles for water purification [84].

Refer to Chapter 1.2 for definitions of membrane performance parameters. Commercial polyamide membranes have permeabilities for RO around 1-10 l m^{-2} h^{-1} bar^{-1} (lmh bar^{-1}) and NF around 10-20 lmh bar^{-1} [42]. Cohen-Tanugi et al. modeled mass transport and fluid dynamics of an RO system to quantify the potential of ultra-permeable membranes [85]. They found that a threefold increase in permeance (1.5 to 4.5 lmh bar^{-1}) may reduce energy consumption 46% for brackish water (BW) RO and also result in the use of 63% fewer pressure vessels [85]. However Cohen-Tanugi et al. calculate a further increase in BW RO permeance beyond >5 lmh bar^{-1} will have a negligible change in energy consumption (because of inherent thermodynamic and process limits) but may continue to lower overall costs [85]. For instance, Werber et al. using their module-scale

modeling study found that a permeance increase from 4 to 10 lmh bar^{-1} may only reduce energy consumption for a single stage by 2.2%, but because of staging effects will result in a 12% reduction for a two-stage brackish water RO [79]. Other opportunities to enhance the desalination membrane performance include: significantly improved efficiency with extremely high rejection, increased membrane performance and lifetime with improved fouling resistance, and lowered pretreatment costs with chlorine tolerance.

2.2. Thin film nanocomposite membranes with nanoporous materials

Nanomaterials with tunable mechanical and chemical properties and with robust porosity offer new possibilities for incorporation into desalination polymeric membranes without significantly altering the scalable, low-cost polymer synthesis process. TFN membrane synthesis involves incorporating nanoparticles into the TFC polyamide film before and/or during the IP reaction [86]. Ultimately, IP of polyamide is a complex, heterogeneous condensation reaction at the interface of a difunctional amine monomer in the aqueous phase and a trifunctional acid chloride monomer in the organic phase [87]. As a result of this reaction, extremely thin (~50-200 nm), highly crosslinked, highly selective, negatively charged, low swelling, hydrophilic polyamide active layer forms on the support. In addition to the dense and thin layer, the final structure also contains voids [82]. The IP reaction is an exothermic reaction, and HCl is a byproduct of the reaction. Ma et al. hypothesize that the heat release decrease the solubility of dissolved gas such as CO_2, N_2, and O_2, and the formation of the acidic byproduct further decreases the solubility of CO_2, therefore, the voids form in the polyamide structure [88]. They, also, show by eliminating or promoting the nanobubble formation for the reaction, the morphology and performance of the polyamide can be tailored. Ukrainsky and Ramon

measured the temperature of the IP reaction zone in a microfluidic device using a microscopic visualization technique that determined the temperature can reach ~85°C (higher than the common organic solvents' boiling temperature) [89]. Therefore, they hypothesize the local boiling can make nanobubble at the interface that can create the voids in the polyamide structure, as an alternative explanation [89]. Moreover, Wong et al. show that void size, content, and location has a significant impact on water transport through the active layer [90]. Polymerization conditions such as phase type, concentration, and temperature; chemical contact time; membrane curing time; and curing temperature highly impact the resultant membrane morphology and separation performance [91, 92].

The most common TFN synthesis method is to add nanomaterials, referred to as "fillers" into the casting solutions during the membrane casting process (different methods are described in the following sections and also are summarized in Figure 10). The addition of the fillers to the casting solution may affect the separation performance of the resulting polyamide phase by changing the crosslinking degree and overall reaction yield [93, 94]. Moreover, the particle presence may alter the surface properties (roughness, charge density, hydrophilicity) and thus the overall membrane separation performance [95]. Furthermore, the performance of TFN membranes varies as a function of the type, size, and concentration of nanoparticles [93, 96]. To fully take advantage of the embedded nanoparticles, they must have the appropriate size and internal structure, as well as surface properties compatible with the polyamide to ensure a suitable polymer-particle interface. Also, the concentration of the filler particles should not be too great to destroy the thin film integrity.

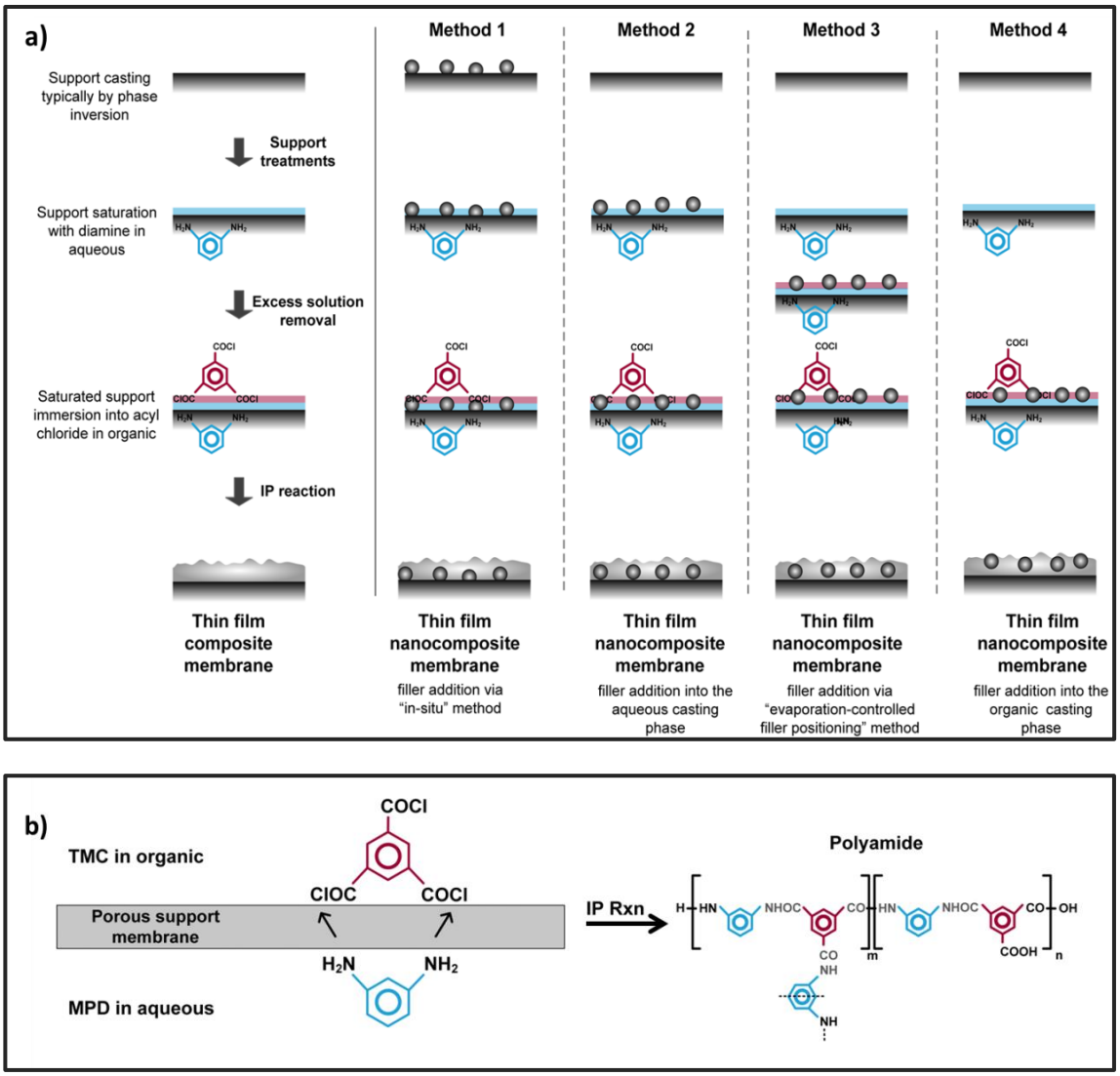

Figure 10: Summary of TFN membrane casting procedures discussed in this review (a) and schematic of a polyamide interfacial polymerization reaction (b).
(a) method 1: filler embedded into the structure via "in situ method" [97], method 2: fillers added into the aqueous membrane casting solution [94, 98-100], method 3: fillers added through "evaporation-controlled filler positioning" method [101], and method 4: fillers added into the organic casting solution [74, 102, 103]. Spherical particles represent nanoporous zeolite and MOF particles and also graphene-based material nanosheets. However, nanosheets addition into the thin film structure occurred only through method 2 [104-109] and method 4 [110] during this review period. (b) the resulting polyamide has a both crosslinked (m) and linear (n) structures. MPD: m-phenylenediamine and TMC: trimesoyl chloride (MPD and TMC are common monomers for polyamide RO membrane synthesis). The figure is taken from [111].

The exact mechanism for the particle-polymer interface and the structure for TFNs is not yet completely understood [78, 112]. In addition to this unknown mechanism, other challenges can arise in TFN formation including particle aggregation in the polyamide layer; non-uniform particle dispersion in the structure; orientation difficulties, especially for non-three dimensional particles; and unknown particle stability during the reaction and the high-pressure filtration [78].

2.2.1. Zeolites

Zeolites are inorganic, crystalline, rigid, hydrated aluminosilicates with a defined general formula and narrow pore distribution (3-8 Å pore size). Zeolites have been a popular nanoparticle included in TFN desalination membranes [78]. Of the 235 possible zeolite framework codes in the International Zeolite Association (IZA) database, only Linde type A (LTA), Faujasite (FAU), Linde type L (LTL), and Zeolite Socony Mobil Five (MFI) frameworks have been investigated to date for TFN membranes.

In 2007, Hoek's group published a seminal work on TFN membranes for RO desalination in which NaA zeolites were added into the organic phase casting solution [54]. This highly hydrophilic zeolite with the LTA framework has 3-dimensional pores (~4.2 Å), which have a suitable pore size for selecting water (2.8 Å) but rejecting hydrated ions (>6 Å) and small organic molecules. In addition, the cubic structure of the zeolite pores ensures water access to the pore regardless of the orientation in the membrane.

We studied the stability of hand-cast NaA-TFN membranes (particle addition into the organic phase) during a 4-month performance test with brackish waters (~400 ppm TDS) at the United States Bureau of Reclamation's Water Quality Improvement Center

in Yuma, AZ. The water permeance of TFN membranes showed 80% higher water-salt permselectivity than the TFC membranes [74]. However, the membranes did not experience high fouling or extreme pH conditions as well as no cleaning or chemical treatments.

Because of dealumination from the framework, aluminum-rich zeolite, such as NaA, are less structurally stable when exposed to acidic solutions in TFN membranes compared to silicon-rich structures, such as MFI [60]. Indeed, our group extensively studied acid environment stability of NaA zeolite and identified that it is not suitable for applications in low pH solutions (pH<2) especially in the presence of phosphate (pH<5) [113].

For BW RO Dong et al. studied TFN membranes synthesized by adding hydrophilic NaY zeolites (150 nm particle size) into the amine casting solution [94]. NaY has the FAU framework type with a larger pore size (~7.4 Å) than the NaA zeolite. The larger pore size may lead to a more preferential water pathway through the zeolite but may weaken size exclusion effects. In the study, however, at the optimum zeolite loading, the membranes showed enhanced water permeation compared to the control TFC membranes but maintained the high salt selectivity [94]. Importantly, this study demonstrated that the reaction time necessary to form a dense zeolite-polyamide layer in the TFN was increased compared to the TFC, suggesting the particle presence was limiting amine diffusion during the IP reaction. Additionally, glycerol-salt solution post-treatment further improves the TFN permeability performance by 16% without any sacrifice in selectivity [94].

Dong et al. developed a TFN "in-situ" method (TFN-I) in which LTL zeolites (~7.0 Å pore size) were added to the support prior to the IP process for NF performance [97]. During the phase inversion preparation of the polysulfone support membrane, they dispersed 80-nm diameter LTL particles into the water bath solution, calling it an "in situ" method. They report this resulted in ~49% particle coverage ratio of the support membrane surface without particle aggregation. Based on their previous study [114], Dong et al. stated the particles are strongly attached to the support. Compared to TFN and TFC control membranes, TFN-I membranes, had a significantly higher surface area difference because of the initially higher support surface area. These TFN-I membranes demonstrated significantly enhanced water permeation but decreased monovalent and divalent salt selectivity (possibly indicating the presence of membrane defects).

Natural zeolites could be a low-cost and environmental-friendly alternative to synthetic zeolites. These materials require treatments to enhance uniformity, purity, hydrothermal stability, and to alter separation characteristics. Unfortunately, treatment methods may also impair the desired characteristics of zeolites. The hydrophilic Clinoptilolite zeolite, which is the most abundant naturally occurring zeolite in the world [115], loses its crystallinity under high temperature and steam treatment [116]. Safarpour et al. studied non-thermal glow discharge plasma treated clinoptilolite zeolite-TFN for RO desalination and fouling resistance [98]. According to the x-ray diffraction pattern, the zeolites retained their crystallinity after the plasma treatment. However, based on the scanning electron microscope images, instead of fine particles, after plasma treatment, the zeolites looked like a big chunk. The TFN membranes were synthesized with 0.01 wt% plasma-treated zeolites incorporated into the aqueous phase IP casting solution. These

demonstrate improvement on hydrophilicity, antifouling property, water permeability, and salt selectivity compared to the controls.

Two-dimensional zeolite nanosheets are an emerging material for desalination which offer a shorter diffusion path-length than 3-D materials. Non-equilibrium molecular dynamic simulations by Jamali et al. identified possible hydrophobic zeolite nanosheets which might have 100% rejection with a pore limited diameter <5.5 Å and estimated 54 lmh bar^{-1} water permeance (for 100 nm thick membrane) [34]. However, there are no experimental reports on two-dimensional zeolite membranes or zeolite nanosheets in TFN membranes.

2.2.2. Metal-organic frameworks

Metal-organic frameworks (MOFs) are hybrid organic-inorganic materials consisting of inorganic metal centers and organic linkers which create crystalline, flexible, and highly tunable pore structures (pore windows 3 Å to ~100 Å). MOFs offer a great variety of nanomaterials for membrane separation applications [117]. Although the structural diversity and highly tunable hybrid structure make MOFs promising fillers for aqueous separations, the majority of the MOF structures degrade upon exposure to ambient moisture [117]. Wang et al. have reviewed the water stable MOFs with potential applications in membranes [118]. Zeolitic imidazolate (Im) frameworks (ZIFs), a well-known subclass of MOFs, have received increasing attention because of their excellent chemical stability.

ZIF-8 is a hydrophobic 3-D material with a $Zn(MeIM)_2$ composition and 3.4 Å nominal aperture size and is the most extensively studied ZIF material in membrane

applications. Zhang et al.'s study reveals that ZIF-8 might provide a molecular sieve in 4-6 Å range, because of the flexible framework [119]. This range makes the material a suitable candidate for desalination. Although Zn releases from the structure when exposed to seawater, the material maintains the crystal structure [120]. Duan et al. state the potential advantages as (1) the hydrophobicity of the material, which may provide fast water transport and (2) the organic linker may enhance the particle compatibility in the nanocomposite [102]. In two studies, nanosized ZIF-8 TFNs, with 80 and 200 nm particles incorporated through the organic phase, demonstrate increased permeability and maintain RO rejection at same particle loading [102, 103].

Van Goethem's report on ZIF-8 TFN membranes introduces a new TFN synthesis method called "evaporation-controlled filler positioning (EFP)" [101]. They developed a two-step process to pre-position the particles at the aqueous/organic interface during the polymerization reaction. First, particles dispersed in an organic solvent are coated on the amine saturated support. Second, the organic solvent was evaporated before submerging the coated support into the organic phase for the polymerization reaction. Van Goethem et al. hypothesizes this method may address TFN particle orientation challenges and reduce expensive particle usage by eliminating waste. Interestingly, at a ZIF-8 loading of 0.005 w/v%, the filler particle size, whether 75 nm or 150 nm, has no significant effect on the membrane performance. A performance difference is expected based on the difference in the diffusion path-lengths of the particles and the actual number of the particles present (8 times more small particles than large ones). This indicates that performance enhancement may be related to the polymer but not the particle

incorporation. However, at higher loadings, the permeability increases with the particle size and decreases with the loading.

Another TFN synthesis method introduces ZIF-8 particles into the aqueous/amine casting solution with an anionic, water-soluble polymer, Poly(sodium 4-styrenesulfonate) (PSS) [99]. Zhu et al. hypothesized that the PSS modifies the ZIF-8 particle surfaces which will improve their dispersion into the aqueous solution. Thus, the final membrane structure may have less particle aggregation. The method involves a similar evaporation step to Van Goethem's to position the particles before IP. The modified ZIF-8 TFN-NF membranes demonstrated increased hydrophilicity, roughness, and negative charge. They also demonstrated double water permeation compared to control membranes and slightly decreased divalent ion retention [99].

Another hydrostable MOF structure is hydrophilic chromium(III) terephthalate Materials Institute Lavoisier (MIL-101(Cr)) with 12 Å pentagonal pore size. Xu et al. embedded ~200 nm MIL-101(Cr) particles in TFN membranes for desalination [100, 121]. They compared TFNs synthesized with particles dispersed in the aqueous IP casting phase and TFNs with particles incorporated into the organic IP casting phase [100, 121]. In the latter study, the TFN membranes prepared with MIL-101(Cr) particles in organic solution showed enhanced, stable RO separation performance, increased roughness and hydrophilicity compared to the TFC membrane [100].

Two-dimensional MOF nanosheets have been recently assembled with a polycationic polymer for nanofiltration. The membranes exhibited very high permeance of ~4000 lmh bar^{-1} (for 48 nm thick membrane) and high selectivity to organic dyes, but

only 20-40% salt rejection [122]. However, there are no reports on the MOF nanosheets incorporated into TFN membranes.

2.2.3. Graphene-based materials

Graphene is a monolayer of carbon atoms with a flexible, hydrophobic, and nonporous structure. Perforated graphene has attracted increasing attention because it has ideal membrane features: it can be as thin as 3.4 Å, has a robust structure under harsh conditions, and has a theoretically near perfect molecular sieving mechanism [23]. Pore creation in graphene experimentally demonstrated a potential for desalination applications [123, 124]. For instance, O'Hern et al. synthesized a defect-free, centimeter-scale graphene membrane on a polycarbonate track etch support [124]. Their creative method included two defect sealing procedures: (1) they filled small defects with hafnia using atomic layer deposition and (2) they sealed large defects with nylon-6,6 via interfacial polymerization [124]. However, an efficient, scalable synthesis creating a narrow pore distribution of a defect-free graphene membrane on an economical support is a significant challenge [23].

Graphene oxide (GO) (graphene with hydrophilic functional groups) membranes have water transport through the tunable interlayer spacing and defects within the sheets [125]. Although recent work showed a great desalination potential of GO membranes, more research is necessary for stability and scalability challenges [126]. Abraham et al. experimentally showed the salt rejection by channel confinement in 100 μm thick, stacked GO-graphene laminates using epoxy. Their method enables control of layer spacing to dimensions <10 Å resulting in less swelling in water. However, the membrane displayed much lower water permeance than the predictions (experimental: ~0.5-1 lmh

bar^{-1} vs. prediction: ~208-1042 lmh bar^{-1} [127]) because of the difficulty of scale-up of the thin structure [125]. Therefore, adding GO nanosheets into polyamide, currently, can be more economical and convenient approach than trying to synthesize pure GO membranes.

Adding graphene oxide in TFN membranes (addition through the aqueous phase) improved permeability with a slight decrease in selectivity for RO [104, 105] and NF [106]. Besides the improved permeability, the membranes exhibited a lower contact angle, enhanced anti-fouling properties [104-106], and more importantly improved chlorine resistance [104, 105]. It is hypothesized that the GO nanosheets prevented chlorine attack of the underlying polyamide. Horizontal GO orientation in the structure is attributed to the Langmuir-Blodget film formation, which commonly results in smooth membrane surfaces [104, 107]. Recently, Chae et al. further improved the membrane permeability and antifouling properties by embedding GO both the active layer and the support layer [128].

Safarpour et al. observed a synergetic effect in RO TFN membranes made with reduced GO and titanium dioxide (rGO/TiO_2) [108]. The membranes showed better separation performances, anti-fouling, and chlorine resistance behavior when embedded with both fillers. Moreover, rGO and TiO_2 dispersed well in water but not in the organic phase; thus particle addition to TFN structure was through the aqueous phase. Carboxylated graphene oxide (cGO) has increased hydrophilicity compared to GO with carboxylic groups added; cGO has been studied for better filler dispersion in the aqueous phase for NF membrane [107]. Compared to control untreated GO-TFN membranes, the cGO membranes have 22% lower contact angle, 7% higher divalent salt rejection, and

87% higher permeability. However, the cGO-TFN membranes have 58% lower monovalent salt rejection than GO-TFN membranes [107].

TFN-RO membranes with functionalized GO nanosheets (polyethyleneimine (PEI) and tannic acid (TA), pTA-f-GO) showed improved permeability and selectivity, chlorine resistance, and antibacterial properties compared to TFC [109]. In this low cross-linked membrane, TA tightly binds GO and PEI allows crosslinking of amine to TA and PA [109]. Wen et al. added acyl chloride-functionalized graphene oxide (GO-COCl) (homogenously dispersed in ethanol) into the organic IP casting phase for the synthesis of TFN-NF membranes [110]. Although the resulting membranes displayed enhanced separation performances, using ethanol as a dispersion phase made the membranes rougher and more susceptible to fouling [110]. Table 1 demonstrates a comparison of the nanoporous filler material groups in TFN membranes, and Table 2 summarizes the recent development of TFN membranes based on the porous filler types and their membrane performances and key features.

2.3. Water-salt permeability vs. water permeance

Park et al. showed that in mixed matrix membrane studies the separation performance might result in three cases of changing the perm-selectivity depending on the polymer-filler compatibility [129]. Figure 11 shows these three cases. In case (1), with molecular sieve presence selectivity increases but permeability decreases. In case (2), the presence of nanosize molecular sieves with possible nanosheet shapes, homogenous dispersion and interfacial compatibility without significant non-selective gaps can yield both permeability and selectivity increases. In case (3), the presence of any

filler often results in interfacial voids that increase permeability and decrease selectivity.

Case (2) is the ideal solution for MMMs to overcome the perm-selectivity upper bound.

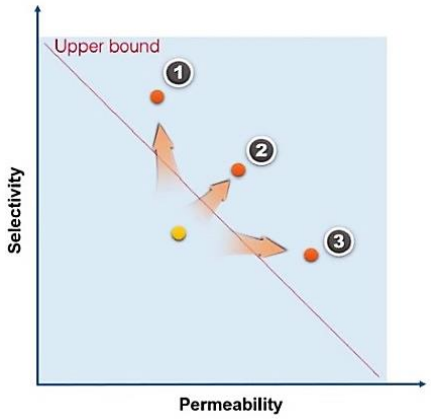

Figure 11: Mixed matrix membrane design paths to overcome the upper bound.
Adding filler materials into the structure requires polymer-particle compatibility and results in one of three cases. (1) selectivity increases, but permeability decreases; (2) both permeability and selectivity increase; and (3) permeability increases but selectivity decreases because of the interfacial voids between the polymer and the filler. The image is reproduced from [129].

Table 1: Comparison of the nanoporous filler materials discussed in this review.
Zeolites are microporous inorganic materials. Metal-organic-frameworks (MOFs) are microporous hybrid organic-inorganic materials. Tunable interlayer spacing graphene-based materials consist of nonporous graphene layers with functional groups. LTA, ZIF-8, and GO accessible pore structures are given as examples of their groups. This qualitative comparison methodology is adapted from [117]. ZIF-8 pore structure is modified from [120]. The table is from [111].

	Zeolites	**Metal-organic frameworks**	**Graphene-based**
	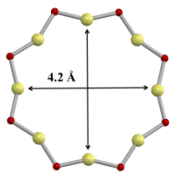 LTA	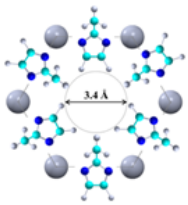 ZIF-8	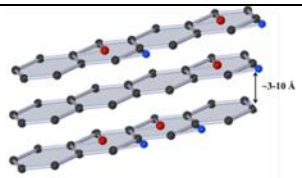 GO
Structural diversity	Medium	High	Low
Pore robustness	High	Medium	Low
Flexibility	Low	Medium	High
Production cost	High	Medium	Low

Table 2: Overview of filler materials in TFN membranes discussed in this review. Rejection of RO membranes in a NaCl test and rejection of NF membrane in a $MgSO_4$ test except [74] in a brackish water test and [99, 110] in a Na_2SO_4 test. The comparison behaviors are based on the reported results, calculated as values of $|\mathbf{TFC - TFN}|/\mathbf{TFC.}$ ↑, ↓, ↔ indicate an increase, decrease, and remain the same. The table is from [111].

	Filler material	Filler size (nm)	Pore size (Å)	RO/ NF	Filler addition (amount and phase)	Permeance (lmh bar^{-1})	R^ (%)	Compared to their corresponding TFC membrane			
								Per.**	R^	F'	C"
Zeolites	NaA [74]	100	4.2	RO	0.30 w% in organic	1.9	97.9	44% ↑	0.5% ↑	n/a	n/a
	NaY [94]	150	~7.4	RO	0.15 w% in aqueous	4.8	98.8	84% ↑	0.4% ↑	n/a	n/a
	LTL [97]	80	~7.0	NF	In situ to the support	8.0	93.4	120% ↑	3% ↓	n/a	n/a
	Clinoptilolite [98]	n/a	n/a	RO	0.01 w% in aqueous	2.7	97.1	39% ↑	2% ↑	↑	n/a
Metal organic frameworks	ZIF-8 [102]	200	3.4	RO	0.04 w% in organic	3.4	98.5	162% ↑	0.4% ↑	n/a	n/a
	ZIF-8 [103]	80	3.4	RO	0.04 w% in organic	1.7	99.4	53% ↑	1% ↑	n/a	n/a
	ZIF-8 [101]	150	3.4	RO	0.005 w% in EFP*	2.7	85	185% ↑	↔	n/a	n/a
	m-ZIF-8 [99]	59	3.4	NF	0.10 wt % in aqueous	14.9	95	115% ↑	↔	n/a	n/a
	MIL-101(Cr) [100]	200	12	RO	0.05 wt% in aqueous	3.2	99	44% ↑	↔	n/a	n/a
		Sheet size (nm)	**Layer space (Å)**								
Graphene-based	GO [104]	70-140	n/a	RO	38 ppm in aqueous	1.1	99.3	80% ↑	↔	↑	↑
	GO [105]	n/a	8.8	RO	100 ppm in aqueous	2.0	97.5	39% ↑	1% ↓	↑	↑
	GO [106]	n/a	n/a	NF	0.2 w% in aqueous	1.5	97	1120% ↑	1% ↓	↑	n/a
	rGO/TiO_2 [108]	n/a	n/a	RO	0.02 w% in aqueous	3.4	99.5	50% ↑	2% ↑	↑	↑
	cGO [107]	n/a	n/a	NF	100 ppm in aqueous	11.7	99.2	185 % ↑	11% ↑	↑	n/a
	pTA-f-GO [109]	n/a	n/a	NF	19 ppm in aqueous	1.8	94.8	69% ↑	13% ↑	↑	↑
	GO-COCl [110]	500-5000	n/a	NF	0.002 w% in organic	3.8	97.1	95% ↑	2% ↑	↑	n/a
Commercial TFC membranes [42]				RO		1-10	~98-99.8 %				
Commercial TFC membranes [42]				NF		10-20	~98-99 %				

*EFP = evaporation-controlled filler positioning
**Per.= permeance
^R = rejection
'F = fouling resistance
"C = chlorine resistance

The water permeance, A, and the salt permeance, B, coefficients define the dense RO membrane desalination performance. However, studies commonly report A values and apparent salt rejection, not the B values. We rearranged equation (1.3) to solve for B, as $B = (A/R)\,(100 - R)(\Delta P - \Delta\pi)$ for RO TFN membrane. Figure 12 shows the water-salt permselectivity compared to the water permeance of the membranes.

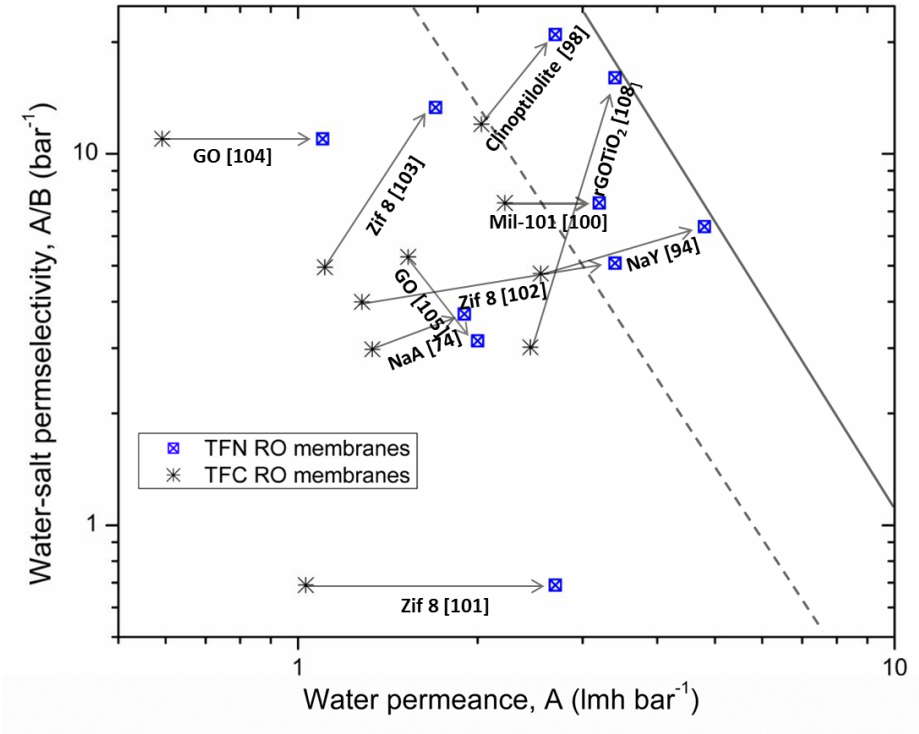

Figure 12: Water-salt permselectivity and permeance of TFC and TFN RO membranes for brackish water desalination.
The permselectivity data were calculated from: NaA [74], NaY [94], Clinoptilolite [98], Mil-101 (Cr) [100], Zif-8 [101-103], GO [104, 105], and rGO/TiO_2 [108]. The star symbol is for TFC membranes, and the arrows indicate the corresponding TFN membranes (in blue square symbols). The black dashed line indicates the upper-performance level for reported TFC membranes and the black line indicates the updated upper-performance level for TFN membranes.

All of the membranes showed improved permeance results but no uniform perm-selectivity results. Of the reviewed fillers, TFN membranes embedded filler particles

Clinoptilolite [98], ZIF-8 [103], and rGO/TiO_2 [108] displayed both significant perm-selectivity and permeance improvement compared to their TFC membranes (the improvement is similar to case (2) in Figure 11). However, the results were scattered even for the similar type of nanoporous fillers. Also, the perm-selectivity results for the lab-made TFC and TFN membranes were significantly lower than the published commercial TFC RO membrane performances [32], as in Figure 13. The results for the reviewed studies are within the permselectivity, and permeability range of chlorine-alkaline treated RO membranes in Figure 13. The IP protocols were different in the TFN studies, and only NaA study applied sodium hypochlorite/sodium bisulfate treatment. The different IP and treatments increase the complexity of the comparison.

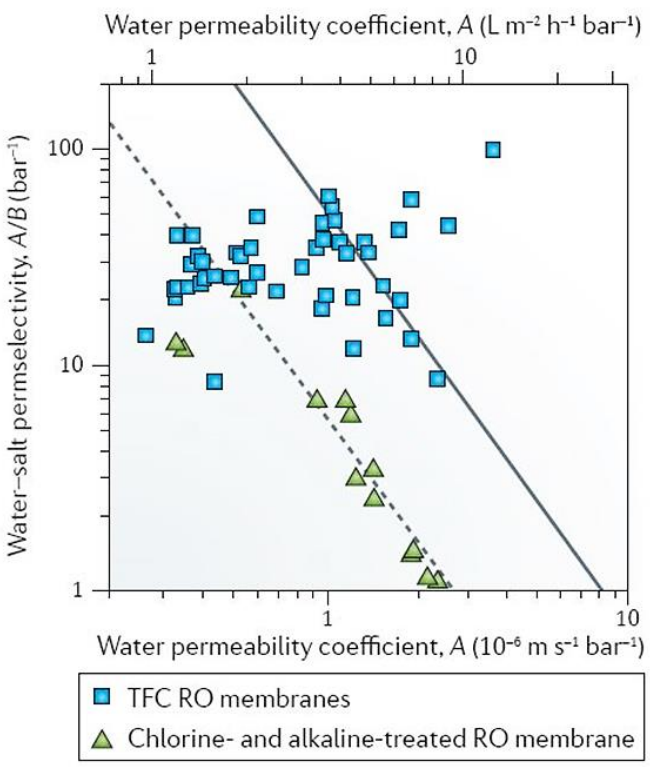

Figure 13: The permselectivity and permeability of commercial TFC RO membranes and chlorine-alkaline-treated commercial seawater RO membranes.
Werber et al. calculated the permselectivity data from manufacturer technical data sheet. The plot is taken from their study [32].

2.4. Conclusion

There is no uniform perm-selectivity result from adding nanoporous materials (zeolites, MOFs, and graphene-based materials) to polyamide-based osmotic membranes. In some rare cases, both the membrane permeability and selectivity are improved significantly, however, in most cases, the rejection only changes from the control of TFC membranes by 2%. Additionally, many of the novel reported TFN membranes do not have performance outside of the range of commercially available TFC membranes. This results from the inherent complexity of the interfacial polymerization reaction, which is compounded by the various researchers' slight change in IP steps, and the actual presence of nanoporous materials during the reaction. To realize the full potential of the nanoporous material in the transport, TFN membrane synthesis may need to be optimized vigorously independently of adding particles into previously optimized TFC membrane synthesis protocols. In mixed matrix membrane for gas separation there has been extensive research modeling and predicting transport properties, there is significantly less in TFN osmotic membranes. The field may benefit from theoretical TFN modeling studies. Additionally, there is significant room for exploration in the emerging area of 2-D materials. Furthermore, TFN membranes exhibit great promise for the addition of new features such a chlorine resistance and fouling resistance.

3. THIN FILM NANOCOMPOSITE MEMBRANES EMBEDDING NONPOROUS AND NANOPOROUS PARTICLES

3.1. Introduction

3.1.1. Zeolite A nanoparticles

Zeolites are crystalline, microporous hydrated aluminosilicates with a general formula of $M_{x/n}((AlO_2)_x(SiO_2)_y)\cdot wH_2O$ where M is a cation (such as sodium, potassium, calcium) and n is the cation valence [130]. The cations compensate the charge balance because of the presence of the negatively charged aluminates in the structure [131]. Accordingly, the ionic forces arrange the aluminates and silicates around the cation [132]. In a well-defined crystalline zeolite framework, the AlO_4 and SiO_4 tetrahedral groups link to each other through sharing an oxygen atom. Nevertheless, AlO_4 tetrahedra can connect to the network only through SiO_4 tetrahedra (Lowenstein's rule [133]). Therefore, the silicon to aluminum ratio (Si:Al) is a distinctive feature for a zeolite. Additionally, the aluminum content in the structure determines the hydrophilicity of a zeolite; increasing aluminum content enhances the hydrophilicity. Thus, the Linde type A (LTA) zeolite is the most hydrophilic zeolite with lowest possible silicon to aluminum ratio (close to one) [131]. Owing to the aluminum-rich structure, LTA tends to adsorb polar molecules such as water [131]. On the other hand, owing to the high aluminum structure, zeolite A may not be stable in an acid environment where dealumination may occur [60, 113]. Moreover, in an aqueous alkaline environment, the structure may not be stable either. Although it is stable for two days under exposure to 1 molar NaOH, the structure converts to zeolite P in 6-10 days (even in a shorter period at an elevated temperature) [130]. In strong aqueous alkaline solution, about 10 wt% NaOH, zeolite A may undergo a phase transformation to hydroxysodalite [130].

LTA zeolite has 24 tetrahedra, 12 SiO_2 and 12 AlO_4, and a characteristic cubic structure with a three-dimensional pore structure. The three-dimensional microporous network ensures access to the pore when embedded in our membranes. Figure 14 shows the cubic unit structure of the LTA zeolite which has large cavity α cages (supercage), ~12 Å, small cavity β cages (also known as sodalite cage), ~6 Å, and eight atom ring forms the window, ~4.2 Å. α and β cages have spaces for 20 and 4 water molecules, respectively, and the ring has space for 3 water molecules. Consequently, a fully hydrated sodium type LTA zeolite has a molecular formula of $Na_{12}((AlO_2)_{12}(SiO_2)_{12})\cdot 27H_2O$ with an accessible pore size of 4.2 Å and a density of 1.99 g cm^{-3} [72] (and accessible volume of 21.4 % [134]). As a result of the narrow pore size, NaA zeolite may be permeable to water molecules (~2.8 Å), but impermeable to hydrated ions such as Na^+ and Cl^- (hydrated diameters > 6 Å [33]).

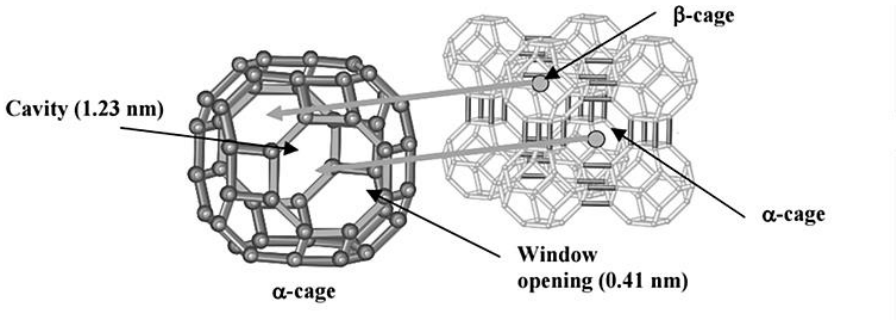

Figure 14: The unit structure of LTA zeolite: α cage, β cage, and eight-membered ring. The eight large α cages are ~12 Å are interconnected through the window openings (eight-member ring) which are ~4.2 Å, and the β cages (~6 Å) are alternating with the α cages. The image reproduced from [131].

The conventional zeolite A synthesis happens in a gel or solution under hydrothermal conditions using templated or template-free methods [135]. In the presence of a template such as organic tetramethylammonium organic cation (TMA^+), the sodalite

cage crystalizes around the cation; and the presence of the template increases nucleation sites for cage creation [136]. Thus, the template usage directs and stabilizes the framework and ensures a narrow particle size distribution [137]. Nonetheless, the zeolite product contains the template inside the intra-crystalline pores, which requires calcination to remove the template and open the pores. However, calcination occurs at an elevated temperature, which may cause particle aggregation [138]. With the templated method, however, we can produce pore-closed nanozeolites, as well as pore-opened nanozeolites (particle sizes less than 500 nm). The particles both open and filled are vital for our study, but particle aggregation may cause a severe problem for the permeability analysis. The pore-closed zeolites could be synthesized with the templated method while the pore-opened zeolites could be synthesized using the template-free method. However, the different synthesis methods might yield differences in particle size distribution and zeolite properties; for example, the aluminum content in the framework and the pore sizes may differ [138], so the hydrophilicity and water permeability may vary. Therefore, we employed the same method for the synthesis. To minimize the particle aggregation during the calcination step, we applied the procedure of introducing a polymer network, reported by Wang et al. in [139]. In this procedure, an organic polymer network acts as a temporary barrier to prevent zeolite nanocrystal aggregation during the calcination [139].

Mintova et al. proposed a crystallization method for LTA type zeolite with a template method depicted in Figure 15 [137, 140]. First, silicate and aluminate precursors and a templating agent are mixed in the presence of an alkaline component, to form an initial amorphous species. After mixing, the 5 nm amorphous particles quickly aggregate to 40-80 nm size particles. The solution type and concentration, time, pH, and

temperature influence the final particle size and structure. Aging the initial solution and increasing the template content decreases the particle size around a narrow distribution [141]. At elevated temperature, the nucleation and crystallization growth takes place. The synthesis temperature and time profoundly affect the particle size and crystallinity during this period. The reaction time favors the product formation and the temperature increases the particle size. The amorphous particles completely transform into the crystalline structure after a particular time, such as two days. Finally, an additional crystal growth mechanism increases the synthesized particle size.

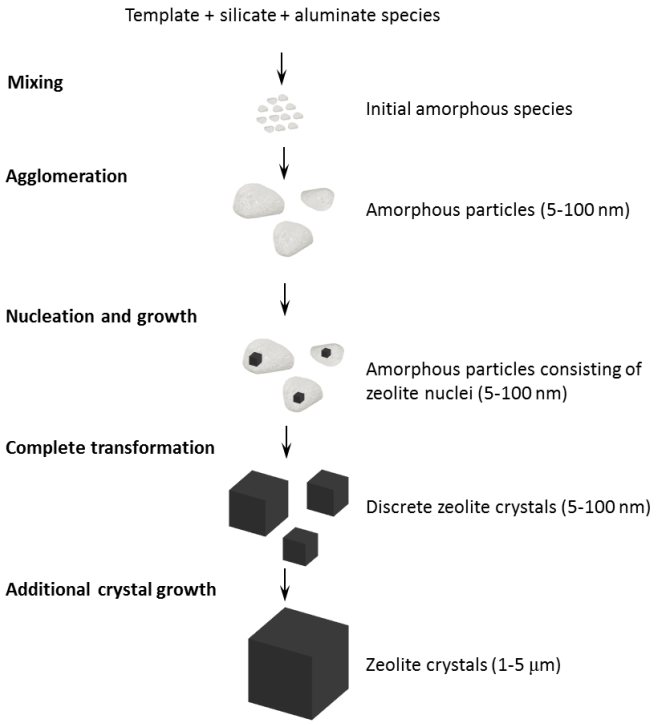

Figure 15: Growth mechanism for LTA nano zeolites from the templated method.
Mintova et al. proposed the growth mechanism [137]. After mixing, initial amorphous gel particles quickly aggregates to amorphous particles in the presence of the template. During the nucleation and growth step, single zeolite crystal forms in an amorphous gel particle. Complete conversion to dense discrete zeolite crystals occurs while maintaining the average particle sizes. Additional crystal growth allows the increase in the zeolite crystal sizes. The image is adapted from [140].

3.1.2. Thin film composite and thin film nanocomposite membrane

TFC and TFN membranes were discussed in Chapter 1 and Chapter 2 in detail, specifically 1.3, 1.4, and 2.2. In this chapter, we investigated the synthesized particles desalination performance in TFN membranes. For this study, we employed the common TFN synthesis method as described in Chapter 2.2. Figure 16 depicts a schematic of the TFN and TFC synthesis in this study.

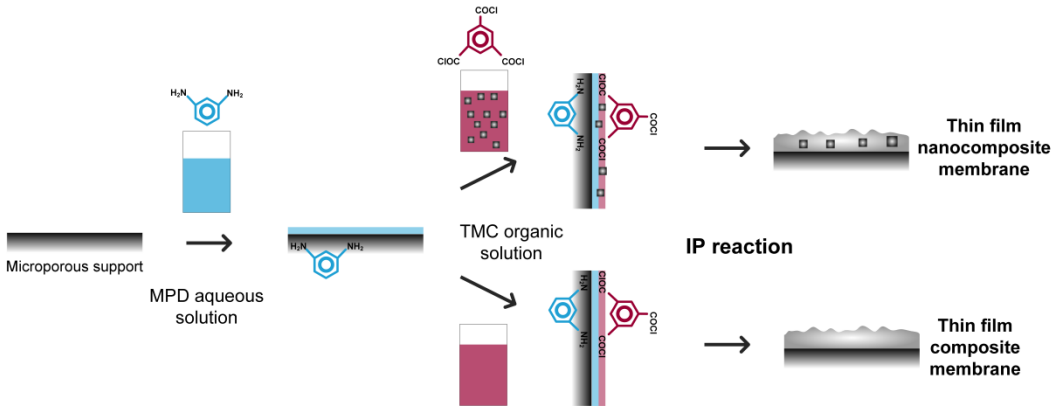

Figure 16: Schematic of TFC and conventional TFN membrane synthesis.
Conventional TFN synthesis involves the addition of nanoparticles to the monomer solutions, MPD or TMC. In this study, we added the particles into the TMC organic solution. TFC membranes procedure was the same with TFN except adding the particles to the organic solution.

In our earlier long-term TFN membrane desalination performance evaluation study, we utilized the same membrane synthesis method explained in Chapter 3.2.3. As also mentioned in Chapter 1.4, in that study, we analyzed the long-term separation performance of TFN membranes with different zeolite contents. The average desalination performance values are summarized in Table 3. The results showed that the maximum

salt rejection for TFN 0.30 membranes was 97.9 ± 0.1 %. We obtained similar salt rejection for TFC and TFN 0.15 membranes, 97.4 ± 0.3 % and 97.2 ± 1.0 %. Also, there was an average of 21% brackish water permeance increase for TFN 0.15 membranes compared to TFC membranes (with no zeolites). Moreover, the permeance improvement for TFN 0.30 membranes was 43% compared to the TFC membranes. As expected, the water permeance increased with the zeolite loading. However, as shown in Figure 17, we observed zeolite aggregation on the surface of TFN 0.30 membranes, which may have an impact on the overall desalination performance of the membrane because of the membrane surface property changes. In the synthesis of these membranes, the hydrophilic LTA particles were dispersed in the hydrophobic organic solution. The particles tend to aggregate in the solution to minimize interfacial free energy since it is thermodynamically favorable. Although the degree of particle aggregation in the solution can be minimized at low zeolite content and can be lowered using ultra-sonication just before the IP reaction, however, particles still aggregate. The particle aggregation may lead to an ambiguous result for the water permeance of an individual single-crystal particle in TFN membrane since we are trying to estimate the individual particle water permeability from the overall water permeability of the entire membrane. Aggregated single-crystal particles have non-selective transport pathways between them.

Table 3: Average long-term desalination performance results of TFN membranes. The membranes were cast with the same method explained in this section [74].

Membrane set	LTA loading (wt %)	Water permeance, A ($\mu m\ MPa^{-1}\ s^{-1}$)	Salt rejection, R (%)	Salt permeance, B ($\mu m\ s^{-1}$)	Water-salt permselectivity, A/B (MPa^{-1})
TFC	0.00	3.7 ± 0.6	97.4 ± 0.3	0.16 ± 0.01	24.2 ± 3.5
TFN 0.15	0.15	4.7 ± 0.3	97.2 ± 1.0	0.21 ± 0.11	34.4 ± 7.4
TFN 0.30	0.30	5.3 ± 0.5	97.9 ± 0.1	0.12 ± 0.02	44.2 ± 8.6

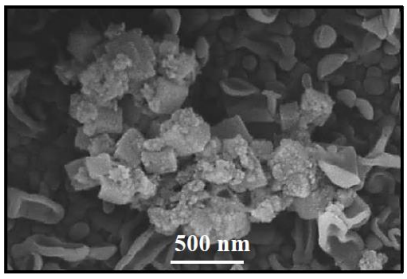

Figure 17: SEM image of 0.30 wt% zeolite content TFN membrane with zeolite aggregation on the surface.

Moreover, the presence of zeolite A particles in the organic solution can change the polymerization reaction because of possible hydration heat release from zeolite when zeolite particles exposed to MPD aqueous solution [55]. The heat release may increase the miscibility of monomer solutions during the interfacial polymerization; the resulting polyamide structure may be less crosslinked [55]. On the other hand, Huang et al. studied the zeolite A particle role during the polymerization reaction of TFN membranes [61]. Their result suggests that the particles in the organic solution have an esterification reaction with the acyl chloride monomer which increases the crosslinking degree of the resulting polymer. Perry's recent dissertation advanced the property-performance relationship in TFN membranes with nanoporous particles to understand the reasoning for the increased water permeance of these membranes [142]. In the study, our zeolite A TFN membranes (synthesized with the conventional method; particles in the organic solution) exhibited no substantial differences in the active layer polymer property (such as water diffusivity, or microstructure) using various advanced characterization techniques [142]. Therefore, the resulting polymer permeability may not change with the addition of particles (it is challenging to characterize the nanoparticle/polymer interface).

To minimize the potential ambiguities resulting from particle aggregation and the impact of zeolite A on the polymerization reaction, in this dissertation, we used 0.15 wt% zeolite A content in organic solution for the TFN membranes. The reader should remember that our primary goal is to estimate the permeability of a single crystal nanoparticle in TFN membrane. The desalination performance improvement of the membranes is of secondary importance.

3.2. Experimental method

3.2.1. Materials

Chemicals used in this study are referred to with the following nomenclature. For particle synthesis we used the following chemicals: for aluminum source aluminum isopropoxide (12.9 - 13.5 % Al, ≥98%, Sigma-Aldrich), for silica source colloidal silica (29-31 % SiO_2, Ludox HS-30, Sigma-Aldrich), for organic cation tetramethylammonium hydroxide solution (TMAOH, 25 wt% in water; Sigma-Aldrich), and sodium hydroxide (NaOH; Sigma-Aldrich). The chemicals used during the removal of the template from the particles procedure were: organic monomer acrylamide (AM, 97%; Sigma-Aldrich), crosslinker N,N'-methylenebisacrylamide (MBAM, 99%; Sigma-Aldrich), and initiator ammonium persulfate (AS, 98%; Sigma-Aldrich).

For the membrane synthesis, a polysulfone coated non-woven polyester ultrafiltration membrane (PSf; NanoH_2O) was used as a support membrane. Monomer solutions: meta-phenylenediamine (MPD, 99%; Sigma-Aldrich) in ultrapure deionized water (UPDI water, Milli-Q Advantage A10; Millipore), and trimesoyl chloride (TMC, 98%; Spectrum) in organic solvent Isoparrafin-G (Isopar-G, technical grade; Gallade chemical) were prepared for the synthesis of the thin polyamide film. The post-cure

rinses consisted of solutions of sodium hypochlorite (NaOCl, reagent grade; Sigma-Aldrich) and sodium bisulfate ($NaHSO_4$, reagent grade; Sigma-Aldrich). The salt rejection performance test was run with sodium chloride (NaCl, ACS grade; Sigma-Aldrich).

3.2.2. Pore-closed and pore-opened zeolite A particles synthesis

The templated zeolite synthesis method was adapted from previously published procedures [143, 144].

The colloidal suspension with the organic template (250 g) was prepared with a molar composition of 1.00 Al_2O_3:6.12 SiO_2:7.17 $(TMA)_2O$:0.16 Na_2O:345 H_2O [143, 144] as follows. One molar NaOH solution (5.55 g) mixed with UPDI water (37.65 g). Next, TMAOH solution (157.25 g) was added to the sodium hydroxide solution. Aluminum isopropoxide (12.55 g) was dissolved in the prepared solution while vigorously stirring. After stirring 4 hours, the silica source (37 g) was added to the clear solution. The resulting solution was aged for 24 hours while stirring at room temperature. The solution was transferred into a polytetrafluoroethylene (PTFE) inner chamber of stainless steel hydrothermal autoclave reactor (CIT-HTC230, COL-INT TECH) and the reactor was placed into an oven for 72 hours, at 110, 130, and 150°C for particles LTA-1, LTA-2, and LTA-3, respectively. After, the particles were washed; centrifuged, decanted, and ultrasonic re-dispersed with UPDI water, until the pH value close to ~ 8. Then, the washed particles were dried for 12 hours at 80 ˚C. The pore-closed particles were ready to use after the drying.

For pore-opened particles, to remove the organic template cation inside the pores, the calcination procedure was applied. First, the washed zeolite particles were mixed with UPDI water for 24 hours (1 g zeolite powder 19 g water). Next, the polymer network which contains; organic monomer AM (1 g) (water soluble), crosslinker MBAM (0.1 g), and initiator AS (0.025 g), was mixed with the aqueous suspension for 5 hours. After the monomer dissolved, the colloidal suspension was sonicated for 30 minutes to maintain uniform dispersion. The suspension was placed in an oven for polymerization and crosslinking into an elastic hydrogel at 50°C for 12 hours. Then the composite was dried at 80°C for 12 hours. The dried composite in a ceramic dish was placed into a furnace and calcined at 500°C for 14 hours (calcination time includes carbonization time of 2 hours). The dried powder of pore-opened zeolites were stored same as the pore-closed zeolites in a desiccator.

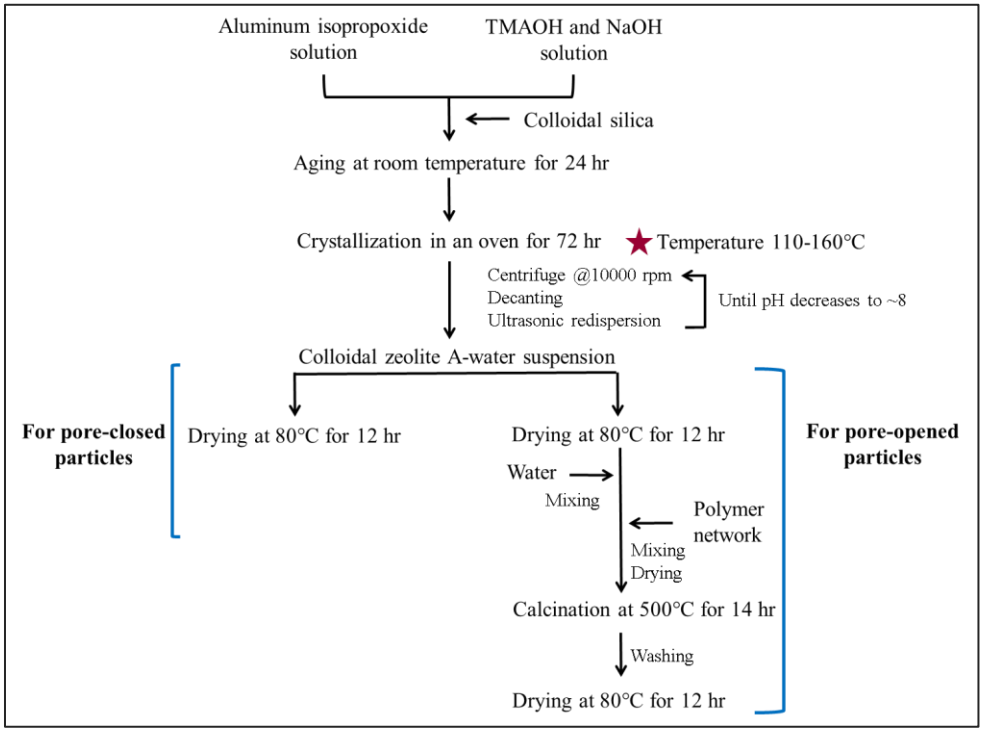

Figure 18: Flowchart of pore-closed and pore-opened zeolite synthesis.

Only crystallization temperatures were different for the zeolite synthesis procedure to adjust the required particle sizes. Also, for pore-closed and pore-opened zeolite particles, the only difference is the post-treatment for the calcination of pore-opened zeolite particles. Figure 18 shows a flowchart of the zeolite synthesis method.

3.2.3. TFC and TFN membrane synthesis

Our casting procedure is based on previously published methods [54, 55, 58]. Thin film composite (TFC) membranes are neat polyamide membranes without nanoparticles. Thin film nanocomposite (TFN) membranes are similar polyamide membranes, with nanoparticles dispersed in the TMC-Isopar-G monomer solution.

For the support preparation before casting, a sheet of polysulfone coated polyester support membrane (8.5” x 4.5”) was sprayed with ethanol (~20 mL), then rinsed with 500 mL running ultra-pure deionized (UPDI) water, and stored in a bottle filled with one liter of UPDI water overnight to ensure the membrane is thoroughly wet before casting. For the casting, first, we prepared the 3.5 wt.% MPD in UPDI water and 0.15 wt.% TMC in organic solvent monomer solutions separately. The solutions were magnetically stirred at 300 rpm at room temperature for at least 3 hours before use. The membrane is removed from the bottle, rinsed with 500 mL UPDI water. Within the twelve minutes of removing from the storage bottle, the membrane was taped on all sides onto a glass plate (9” x 5”) (the timing for the taping can be adjusted based on the temperature and the humidity of the room since support property affects the resulting membrane performance). Then, we soaked the support into 150 mL of MPD in UPDI water monomer solution for two minutes, with the active side (PSf side) facing down in the solution and the back of the plate not submerged. After lifting the plate from the amine solution, to increase the

uniformity of the membrane surface, we removed the excess solution from the surface evenly using an air knife (Super air knife, Exair) operating at 60 psi. Then, we immediately placed the MPD coated membrane vertically into 200 mL of TMC in isopar-G monomer solution in a vertical membrane brick for the interfacial polymerization reaction for one minute. After, we removed the plate from the brick and held it vertically for two minutes. We cured the membrane through a series of post-treatment rinses. First, the membrane was placed in a water bath at ~95 °C with the active side up for two minutes. Then, we applied chlorine-sulfate treatment to remove unreacted MPD in the membrane structure. First, the membrane was removed from the glass plate and placed into 1.5 mL L^{-1} NaOCl in deionized water for two minutes. Next, the membrane was placed into 1 g L^{-1} $NaHSO_4$ in deionized water for 30 seconds. Finally, the membrane was placed in a freshwater bath at ~95 °C with the active side down for two minutes. The resulting membranes placed into one liter of UPDI water in a light-proof Nalgene bottle and stored at 4°C until testing.

The only difference between the TFC and TFN membrane synthesis procedures was that the TMC-isopar G solutions containing 0.15 wt% LTA zeolite nanoparticles were ultra-sonicated at ~20 °C for 30 minutes (ice was added to the sonication bath as necessary to maintain the temperature). The sonicated solution was poured into the membrane brick immediately before the polymerization reaction.

For this work, we synthesized TFC membranes as control and six types of polyamide/LTA zeolite thin film membranes with six different zeolite particles. We had three different particle sizes (called LTA-1, LTA-2, and LTA-3) and two different pore-states (pore-closed (non-porous) and pore-opened (nanoporous)) of each size of the

particle. The names of each membrane set are TFC, $TFN_{1\text{-}PC}$, $TFN_{1\text{-}PO}$, $TFN_{2\text{-}PC,}$ $TFN_{2\text{-}PO}$, and $TFN_{3\text{-}PC,}$ and $TFN_{3\text{-}PO}$. We named the TFN membranes according to the nomenclature $TFN_{X\text{-}PY}$ where X represents particle size (1, 2, or 3) and Y represents pore state (O – opened, or C – closed).

3.2.4. Membrane performance evaluation

The hand-cast membranes were tested for water permeability and sodium chloride (NaCl) salt rejection, using a custom fabricated, cross-flow reverse osmosis test system as depicted in Figure 19. In the cross-flow system, the feed flows across the membrane surface in a direction normal to the direction of transport across the membrane. The tests were run at 200 psi of applied hydraulic pressure with UPDI water and saline waters (2,000 ppm NaCl).

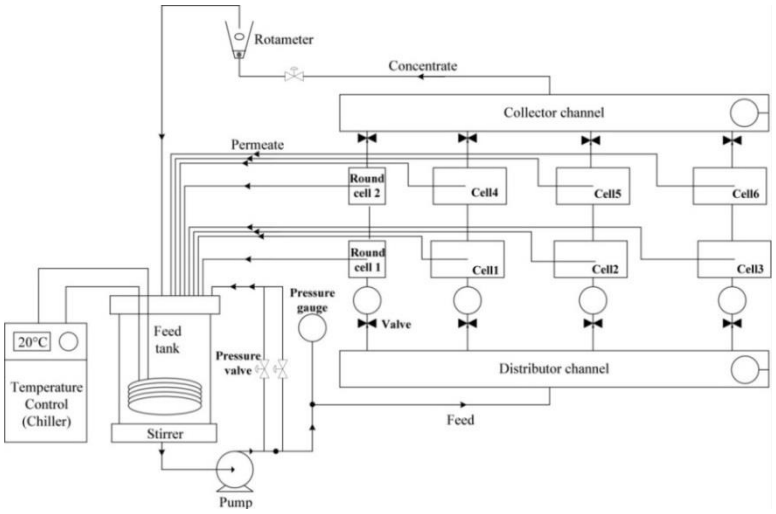

Figure 19: The custom fabricated, cross-flow reverse osmosis test system.

The pressure differences between the cells which are in series have negligible pressure difference (less than three psi when operating at 800 psi). Saltwater feed causes corrosion; therefore all metal parts in the system are corrosion-resistant 316-stainless steel. The testing condition for this study is pure water and 2,000 ppm NaCl feed at 20°C under 200 psi hydraulic pressure.

All tests were conducted at 20 ± 1°C with a cross-flow rate of 0.5 gpm. After stabilization (overnight compaction), the permeate flow rate was measured with a flowmeter (FlowCal 5000; Tovatech). The permeate and the feed conductivities were measured using temperature compensated two-cell conductivity probes, connected to a meter (Accumet Excel XL50; Fisher Scientific), to calculate the observed membrane salt rejection. At least triplicate membrane samples were tested.

3.2.5. Membrane and particle characterization

X-ray diffraction (XRD, X'Pert Pro; PANalytical) were used to identify the crystalline structure of the synthesized zeolite particles. We ground the samples in a mortar dish before diffraction analysis. The diffraction patterns collected at the diffraction angle 2θ from 5° to 60° under a voltage of 40 kV and a current of 40 mA. Dynamic light scattering data were collected (DLS, ZetaPals Analyzer; Brookhaven Instruments) for washed, dried, ground, and re-suspend particles in water after sonication. The measurement provided the dispersed particle size, as well as a particle size distribution. Thermal gravimetric analysis (TGA, Q500; TA Instruments) performed to determine weight difference of pore-opened and pore-closed particles because of the template presence. The nanoparticle size and morphology, and the membranes surface and cross-section morphology were analyzed using scanning electron microscopy (SEM, Amray 1910 field emission scanning electron microscopy; Amray) at a 5-15 kV beam accelerating voltage at various magnifications. Dried membrane samples were sputter coated with gold for 25 seconds using Cressington 108 Auto Sputter Coater before SEM analysis. Atomic force microscopy (AFM, Dimension Multimode 8; Bruker) was used to determine the roughness of the membrane surface. The tapping mode performed because

the tip can easily damage the polymer while scanning the 5x5 μm^2 scan area at a fixed scanning rate of 1 Hz. The probe (FMV-A; Bruker) tip radius was 8—12 nm, the cantilever length was 225—235 µm with a spring constant of 2.8 N m^{-1}. Attenuated total reflectance–Fourier transform infrared (ATR–FTIR, 6700 FTIR; Thermo Nicolet) with diamond crystal smart orbit provided an insight into the functionality of the particles, and a thin film of the adhesion, adhesion-particle, model, and TFN membranes. We dried the membrane samples in a desiccator overnight before ATR-FTIR measurement. The contact angles of the membranes were measured using de-ionized water sessile drop contact angle analysis (Easy Drop; Krűss) to evaluate surface hydrophilicity of all membranes. The drop volume of the water was two µL. On each air-dried membrane sample, we measured twelve spots. We removed the highest and the lowest values and reported the average value of the remaining measurements.

3.3. Results

3.3.1. Characterization of zeolite particles

The x-ray diffraction pattern can identify the crystalline structure. The peak positions reveal the unit cell dimension and the width of peaks can differentiate the crystallite size [145]. Figure 20 shows that the synthesized particles exhibited the characteristic XRD pattern of LTA crystalline structure (the three strong 2θ characteristic peaks for LTA: 7.20°, 10.19°, 12.49° [146]). The XRD patterns confirmed that the synthesized particles had an LTA crystalline structure. Also, the particles maintained the crystalline structure after removal of the synthesis template. Moreover, the composition of the particles during the synthesis was the same. However, the reaction temperatures

were different, as the temperature increases, larger particles forms. Different particle sizes result in changes in the intensity of the different particles peaks.

Figure 21 presents the SEM images of synthesized particles: LTA-1, LTA-2, and LTA-3, as synthesized, pore-closed, and after the calcination, pore-opened particles. The structures of the particles were visually similar before and after the calcination. Also, the images clearly show the larger particle sizes with the reaction temperature increase. However, as the reaction temperature increase, the size distribution becomes wider, especially for LTA-3 particles. DLS measurements also confirmed a similar trend and similar polydispersity index (PDI) for all particles.

Thermal analysis can provide information about the water content and organic template content in the particle structure. Figure 22 presents the thermal gravimetric analysis of pore-closed and pore-opened LTA-2 particles. Both particles exhibited the water loss with increasing the temperature up to 200°C, whereas only pore-closed showed weight loss starting from 300°C. Thus, TGA confirmed the successful removal of the organic cation from pore-opened particles. Moreover, the thermal analysis indicated that LTA-2 pore-opened particles lost ~20.5% weight up to 200°C and ~1.5% more weight from 200°C to 500°C. The water content matched the fully hydrated zeolite A particle ($Na_{12}((AlO_2)_{12}(SiO_2)_{12})\cdot 27H_2O$), which is ideally 22 wt%. On the other hand, LTA-2 pore-closed particles lost ~15.0% weight up to 200°C and ~7.5% more weight from 200°C to 500°C.

This weight loss trend can be explained by using the TMA^+ number per LTA unit cell given in [147]. In the unit cell, there are eight α cages and eight β cages. Fan et al.

studied the local environments of the template cation in zeolite A [147]. They determined that four α cages and 7.5 β cages are occupied by a TMA^+ cation. Thus, there can be four α cages and 0.5 β cages available for water molecules for pore-closed particles. As explained earlier in Chapter 3.1.1, each α cage can accommodate 20 water molecules, and each β cage can accommodate 4 water molecules, and the ring can hold 3 more. This means that there can be up to 106 water molecules per LTA unit cell for pore-closed particles. Considering molecular formula of the TMA^+ cation, $(CH_3)_4N^+$, with a molecular weight of 74 g mol^{-1}, the total weight of the cation and water molecules in a unit cell can be obtained as 851 g mol^{-1} and 1908 g mol^{-1}. This corresponds to ~16.8 wt% water content given that the template content is ~7.5 wt%. This result is very close to water content which was obtained TGA analysis. Moreover, the TGA plot of the pore-closed LTA particles given in [147] exhibits a very similar behavior with our TGA analysis of the pore-closed particles.

When the zeolites were added into the organic casting solution, the same weight amount (0.15 wt%) was added for all types of particles. For a given weight, the pore-closed particles contain a larger number of particles compared to pore-opened particles because of the weight difference between the template and water molecules. We took this into account when estimating the number of particles used in the water permeability analysis. Nevertheless, the actual amount of particles incorporated in the structure cannot be easily quantified.

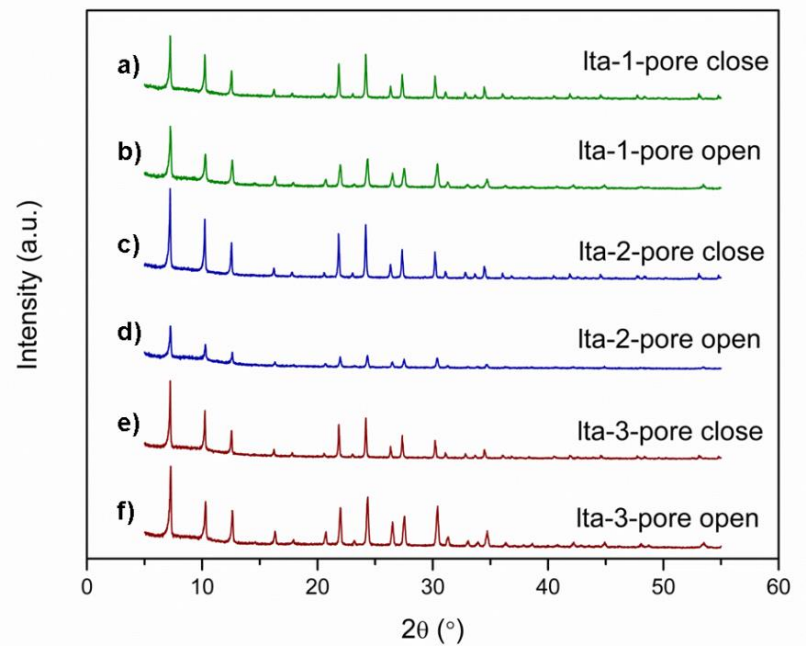

Figure 20: XRD pattern of synthesized zeolite A particles.
The diffraction patterns of particles LTA-1 are (a, b), particles LTA-2 are (c, d), and particles LTA-3 are (e, f). (a, c, d) shows the patterns of as-synthesized particles and (b, d, f) shows the patterns of calcined particles.

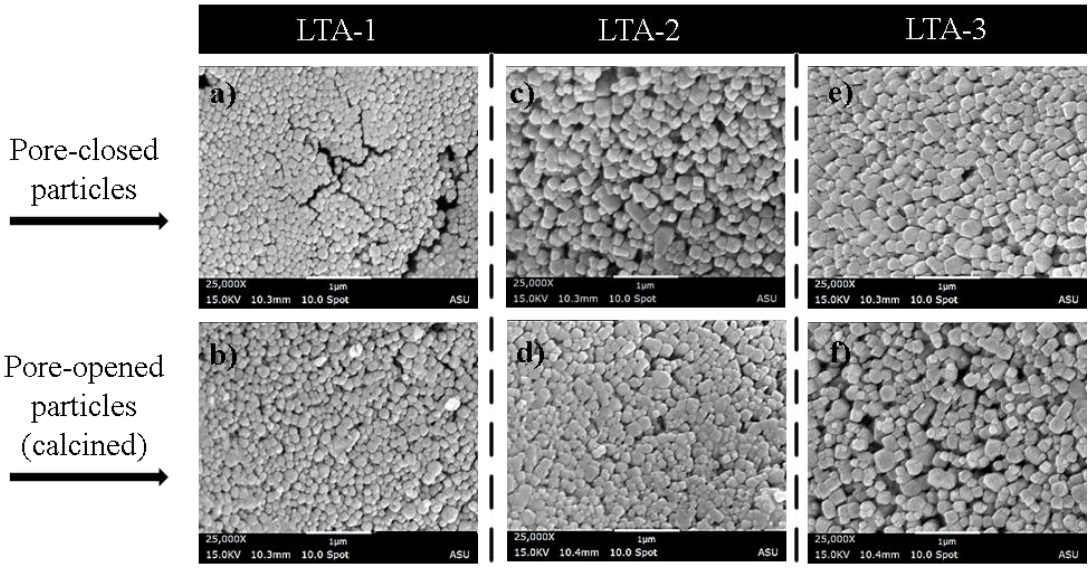

Figure 21: SEM images of synthesized pore-closed and pore-opened particles.
The particles LTA-1 (a, b), LTA-2 (c, d), and LTA-3 (e, f) were synthesized at different crystallization temperatures, i.e., 110°C, 130°C, and 150°C (the size of the particles increases with the crystallization temperature, i.e., ~100 nm, ~150 nm, and ~200 nm). The top row depicts the particles included the organic cation in the pores and the bottom row depict the particles after calcination.

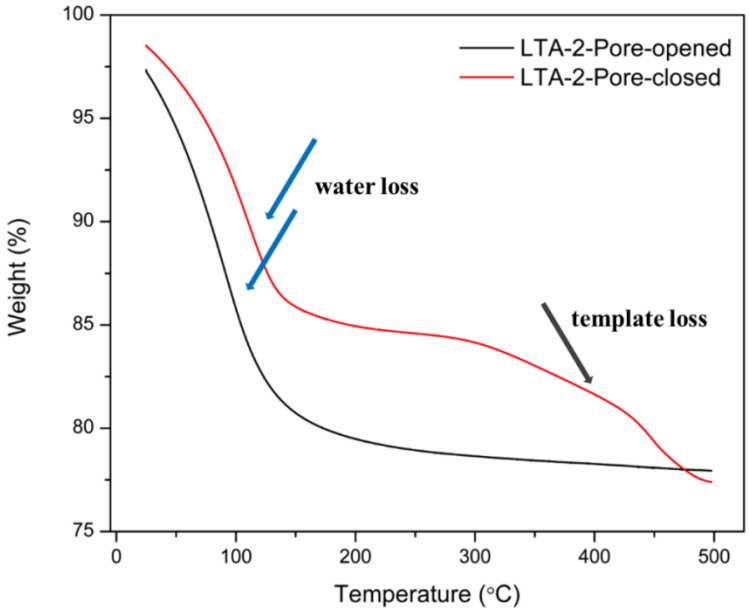

Figure 22: TGA of the particles showing the water loss and the template loss.

3.3.2. Membrane morphology and structure

The crosslinked polyamide TFC and TFN polymer membranes were synthesized via the MPD/TMC interfacial polymerization reaction. As mentioned earlier, this reaction is complex and highly sensitive to the synthesis conditions. We assessed the impact of the particle addition on the polymer. To investigate the surface hydrophilicity of the membranes, we performed contact angle analysis. A hydrophilic surface has a contact angle lower than 90°, and the surface hydrophilicity enhances with the contact angle decreases. Because of the presence of hydrophilic nanoparticles, other researchers have found that TFN membranes show a lower pure water contact angle than corresponding thin film polymer membranes [54, 57, 58, 148]. As discussed in Chapter 3.1.1., Si:Al ratio determines the hydrophilicity of zeolite particles. Our synthesized particles exhibited ~1.6 in the SEM-EDAX analysis. The ratio is very close to the ratio in a previous study where we adapted our zeolite synthesis procedure [143]. In the study, the film of the particles showed 2° contact angle for water. If we assume a similar water

contact angle value for our single particles, the particle presence should lower contact angle value of the membrane. However, the membrane surfaces have an estimated particle surface area coverages of ~1.3, 0.9, and 0.7 % for TFN-1, TFN-2, and TFN-3 membranes. At this low particle surface coverage, in the membrane, the actual contribution of the hydrophilic particles on the water contact may not be observed. However, our TFN membranes demonstrated higher average water contact angles than corresponding TFC membranes. Figure 23 shows measured contact angles of the membranes. TFC membranes exhibit the lowest contact angle whereas TFN membranes embedded with LTA-2 particles have the highest. Surface roughness has a strong effect on the wetting property of a material, and corresponding contact angle even when R_q is less than 100 nm [149, 150]. Duan et al. applied the Wenzel model to correct the measured TFN membrane contact angle considering the surface roughness [102]. The Wenzel equation defines the corrected contact angle (θ^*) of a rough surface as the product of roughness factor (r) and the measured contact angle (θ), $\cos\theta^* = (\cos\theta)/r$ [151]. Based on the equation, a hydrophilic ($\theta<90°$) rough surface becomes more hydrophilic with the increase in roughness. The roughness area factor can be estimated from AFM surface area difference (SAD) measurement (r = 1+SAD) [152]. Figure 23 shows the roughness corrected contact angles using the Wenzel equation. TFN membranes with incorporated LTA-2 particles have the highest corrected contact angles compared to the other TFN and TFC membranes. The membrane preparation method has a significant effect on the surface hydrophilicity [55]. Lind et al. observed also increase in contact angle with the addition of zeolite A particles for one of their synthesis method [55].

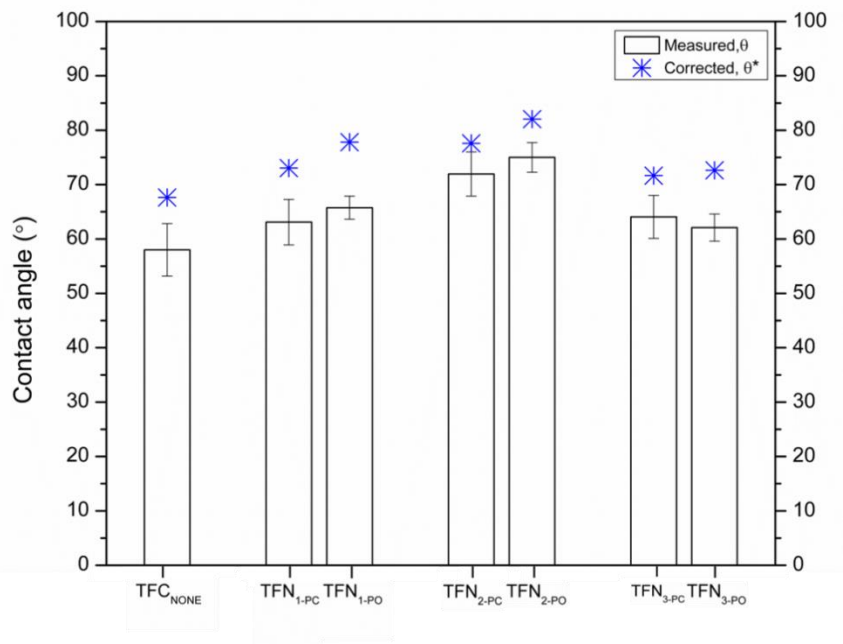

Figure 23: Measured and roughness corrected contact angles of hand-casted TFC and TFN membranes.

AFM analysis provided the quantitative surface roughness morphology. TFN membranes that incorporated the pore-opened particles exhibited more rough structure compared to corresponding TFN membranes with pore-closed particles and TFC membranes. Moreover, TFN membranes with pore-closed particles showed similar average roughness surface morphology with the TFC membranes. $TFN_{2\text{-}PO}$ membrane surfaces have the highest average roughness, R_a, of 98.6 ± 2.0 nm whereas $TFN_{2\text{-}PC}$ and TFC membrane surfaces have R_a of 66.2 ± 8.2 nm and 69.3 ± 5.6 nm. Figure 26 presents representative three dimensional AFM images for TFC, $TFN_{2\text{-}PC}$, and $TFN_{2\text{-}PO}$ membranes. Table 4 provides a summary of the contact angle and AFM characterization results.

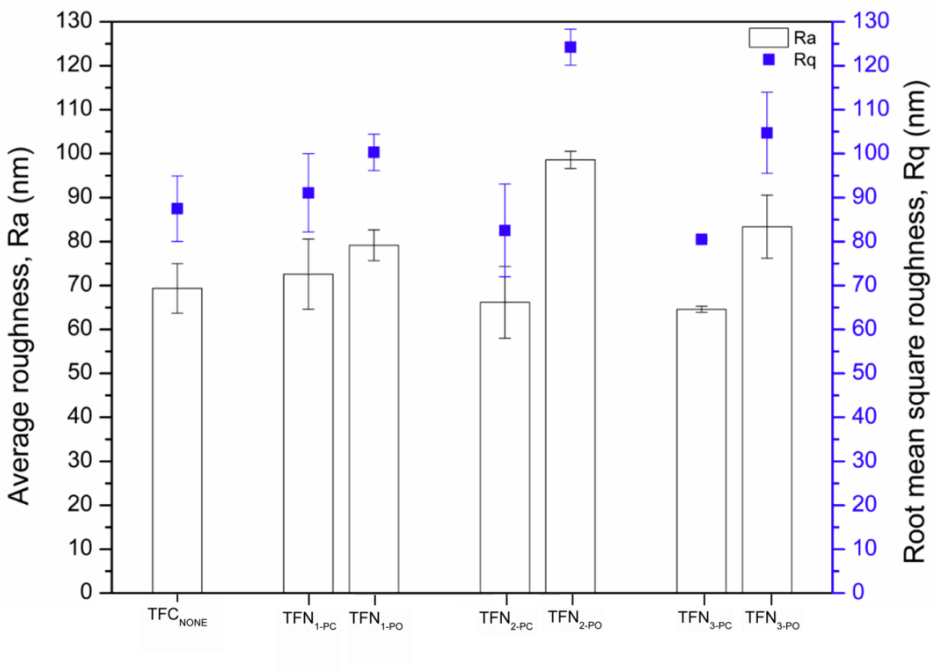

Figure 24: AFM results of TFC and TFN membranes for roughness.
Average roughness, Ra, represents the mean roughness and root mean square roughness, Rq, is the standard deviation of the measured values.

FTIR analysis provides an insight into the chemical functionality of our TFC and TFN membranes. Figure 25 depicts the FTIR spectra of the polysulfone support and hand-cast TFC and TFN membranes. For the polyamide structure, we focused on the characteristic peaks at ~1,540 cm^{-1}, at ~1,609 cm^{-1}, and ~1,663 cm^{-1}, and at 1,734 cm^{-1}, which correspond to the C─N stretch of amide II band, the aromatic amide band, the amide I band, and the C═O carboxylic acid band [58, 59]. The FTIR spectra of the TFC and TFN membranes confirm the successful polyamide formation on the polysulfone support.

Based on the chemical structure of polyamide formation (using MPD and TMC monomers), the linear polymer structure has more carboxylic acid functionality (peak at ~1,734 cm^{-1}) than the crosslinked structure [58]. Previously, Lind et al. observed that TFN RO membranes exhibit an increase in absorbance of the corresponding to the C=O

carboxylic functionality characteristic peak compared to TFC RO membranes. [58] Additionally, Lind et al. measured extent of crosslinking of these membranes using X-ray photoelectron spectroscopy and found less cross-linking in the TFN membranes compared to the TFC membranes. Ma et al. also observed that TFN forward osmosis membranes exhibit an increase in absorbance of the characteristic peaks at 1,734 cm^{-1} as compared to TFC membranes [59]. These results combined with the knowledge that the linear structure of the polyamide formed from MPD-TMC has more carboxylic acid functionality.

We observed insignificant changes in absorbance of the carboxylic acid peak for our membranes (the chlorine-sulfate post-treatment may remove the unreacted or hydrolyzed monomers in the structure). Therefore, it may semi-quantitatively indicate a fully cross-linked polyamide structure for our membranes. Also, the peak at ~1,540 cm^{-1} appears to begin splitting for TFN membranes especially for the membranes including LTA-1 particles. It means that our TFN membranes have fewer C─N bonds, which corresponds to a less polyamide polymer formation. Moreover, the absorbance of the polyamide characteristic peaks at ~1,540 cm^{-1}, at ~1,609 cm^{-1}, and ~1,663 cm^{-1} decreases with the addition of particles, especially in LTA-1 particles.

SEM image visual analysis revealed that all membrane surfaces have similar characteristic MPD/TMC polyamide thin film structure known as “hill and valley” or “ridge and valley” structures [54, 59, 153]. We did not observe a noticeable polymer structure change with the addition of particles or particle pore state. Figure 26 shows representative SEM images of for TFC, $TFN_{2\text{-}PC}$, and $TFN_{2\text{-}PO}$ membranes.

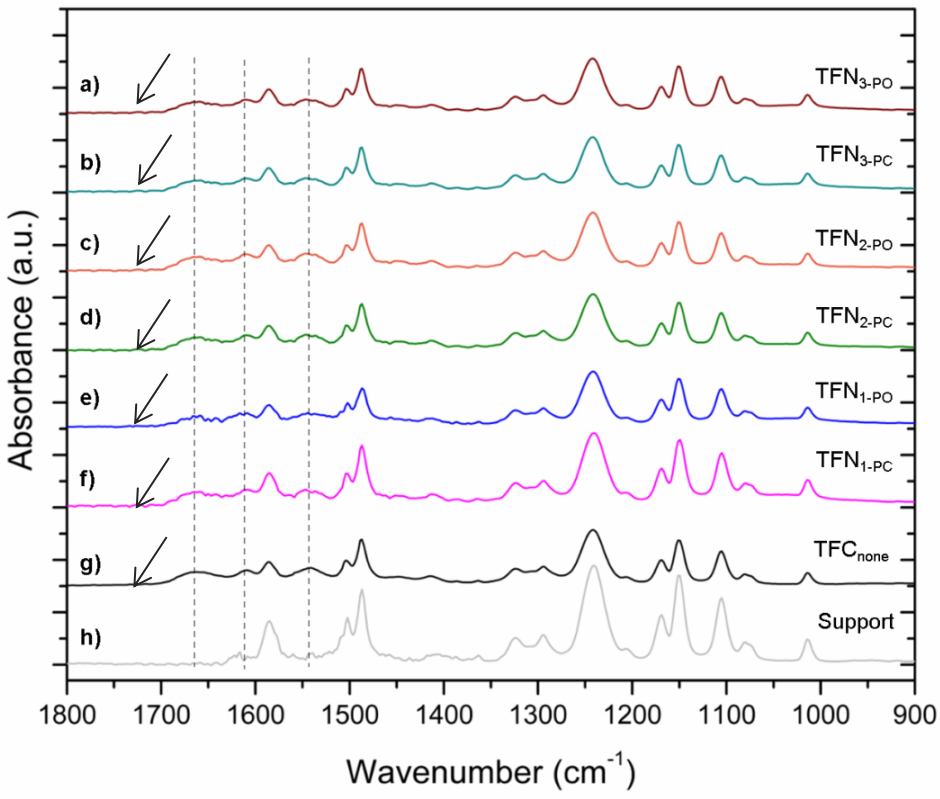

Figure 25: FTIR spectra of the support, TFC and TFN membranes for functionality.

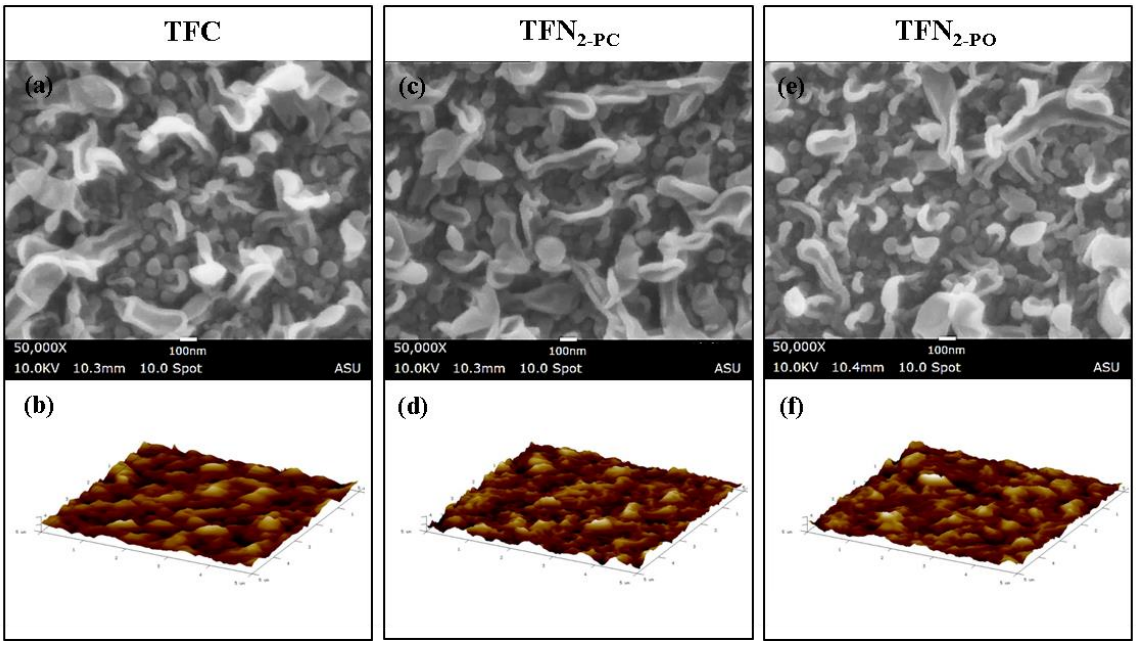

Figure 26: Representative SEM and 3-D AFM images of TFC, $TFN_{2\text{-}PC}$, and $TFN_{2\text{-}PO}$ membranes.

Table 4: Summary of membrane characterization results for contact angle and AFM.

Membrane set	LTA loading wt %	LTA sample #	Pore state	θ (°)	R_a (nm)	R_q (nm)	SAD (%)
TFC	0	none	n/a	58 ± 5	69 ± 6	88 ± 7	39 ± 9
TFN1-PC	0.15	LTA-1	closed	63 ± 4	73 ± 8	91 ± 9	55 ± 6
TFN1-PO	0.15	LTA-1	opened	66 ± 2	79 ± 4	100 ± 4	95 ± 15
TFN2-PC	0.15	LTA-2	closed	72 ± 4	66 ± 8	83 ± 11	44 ± 9
TFN2-PO	0.15	LTA-2	opened	75 ± 3	99 ± 2	124 ± 4	87 ± 7
TFN3-PC	0.15	LTA-3	closed	64 ± 4	65 ± 1	80 ± 1	39 ± 0
TFN3-PO	0.15	LTA-3	opened	62 ± 3	83 ± 7	104 ± 9	57 ± 15

3.3.3. Membrane performances

Figure 27 presents pure water permeance and salt rejection for all hand-cast membranes. For every particle type and particle state, TFN membrane water permeance was higher than the base TFC membrane. For TFN with pore-closed particles, TFN water permeance was decreased with increasing size of the particles. $TFN_{1\text{-}PC}$, $TFN_{2\text{-}PC}$, and $TFN_{3\text{-}PC}$ membranes showed 24%, 12%, and 7% increase in water permeance over TFC membrane. However, this decreasing water permeance with increasing particle size pattern is not valid for TFN with pore-open particles. $TFN_{3\text{-}PO}$ deviates from the pattern. $TFN_{1\text{-}PO}$, $TFN_{2\text{-}PO}$, and $TFN_{3\text{-}PO}$ membranes showed 32%, 19%, and 25% increase in water permeance over TFC membrane.

We used the same weight concentration of zeolites in organic monomer solution for all TFN membranes. Therefore, the particles in $TFN_{1\text{-}PO}$ solution is approximately eight times higher in particle number than $TFN_{3\text{-}PO}$ membranes. Moreover, the number of pore-closed particles in TFN membranes is higher than the corresponding TFN with pore-opened membranes because the total template weight in zeolite cages is smaller than the total weight of water molecules in pore-opened particles. All the membranes have similar salt rejection performances, ~97.5% except $TFN_{1\text{-}PO}$ membrane (lower) and $TFN_{3\text{-}PO}$ membrane (higher) performances.

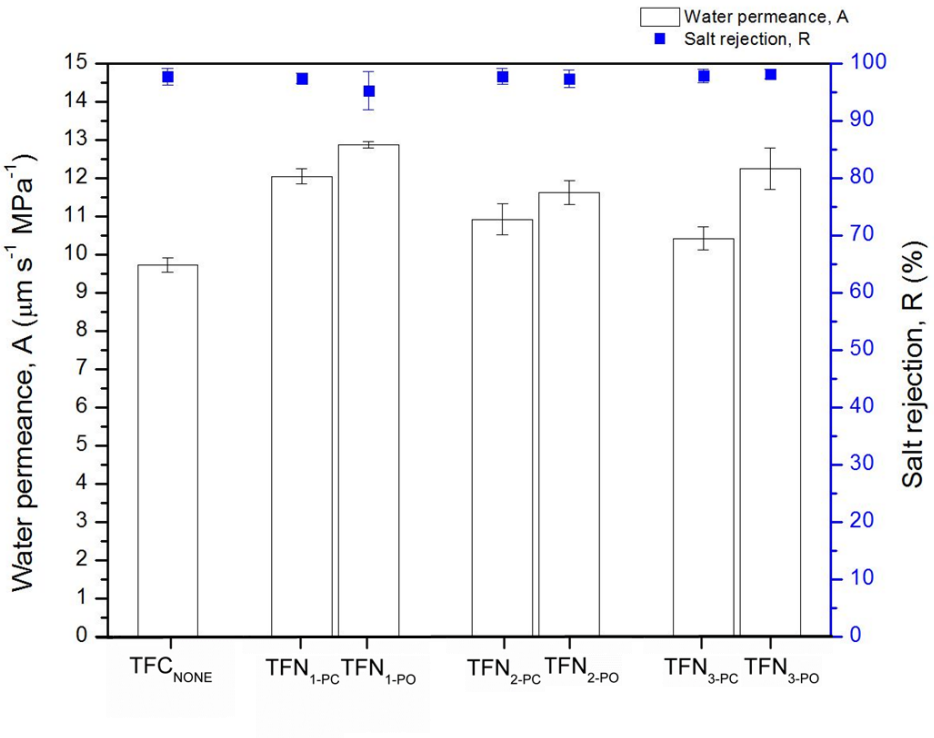

Figure 27: Water permeance and salt rejection performances of TFC and TFN membranes.
The membrane synthesis occurred at 50% relative humidity and 22°C room temperature. The membranes were tested in the custom build cross-flow testing system at 200 psi. Salt rejection test performed using a 2000 ppm NaCl feed solution. The feed temperature during testing was at 20 ± 1°C.

To further evaluate the performance enhancements for the impact of the particle pore-state and particle size, we compared water-salt perm-selectivity and water permeance performance of the membranes. Figure 28 depicts the comparison for all membranes. $TFN_{3\text{-}PO}$ membrane showed the ideal MMM performance enhancement, both permeance, and selectivity enhancement. The performance difference between $TFN_{2\text{-}PC}$ and $TFN_{2\text{-}PO}$ membranes is less than the between $TFN_{3\text{-}PC}$ and $TFN_{3\text{-}PO}$ membranes, and between $TFN_{1\text{-}PC}$ and $TFN_{1\text{-}PO}$ membranes. Because of the smaller particle size and the higher number of particle in the casting solution, $TFN_{1\text{-}PO}$ membranes may have higher particle aggregation probability.

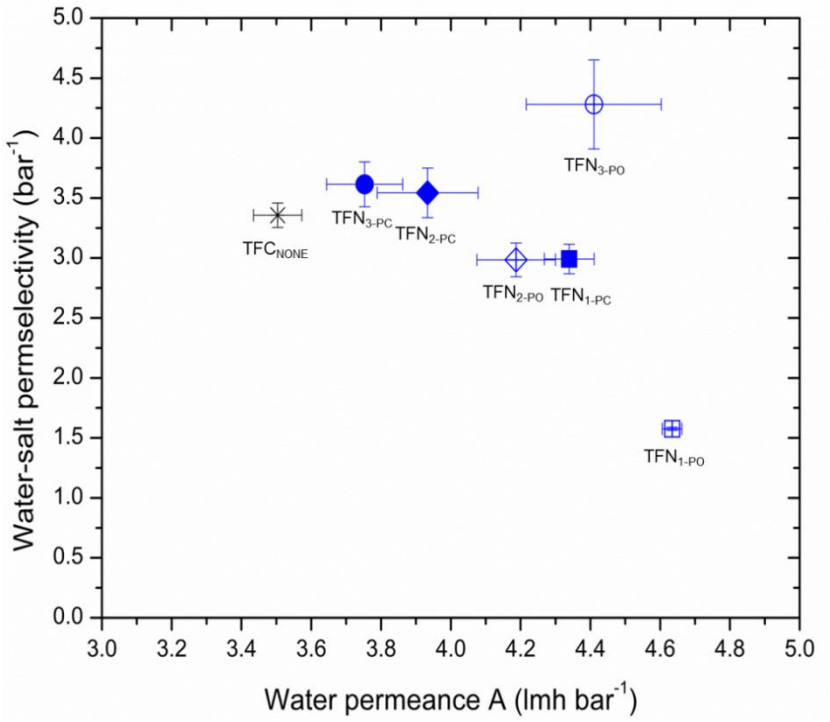

Figure 28: Water-salt permselectivity vs. water permeance of the tested membranes.

3.4. Conclusion

We investigated thin film nanocomposite membranes synthesized via conventional interfacial polymerization method for the impact of zeolite crystal size and pore-state on the membrane performance (water permeance, salt rejection, and water-salt perm-selectivity), membrane surface morphology, and structure. Membranes with incorporated smaller particles exhibited higher water permeance, however, lower water-salt permselectivity than membranes with larger incorporated particles. Membranes with pore-opened particles showed higher water permeance compared to corresponding membranes with pore-closed particles. However, the number of particles in the casting solution was different (template presence in the pore structure). Therefore, more analysis is required for a better understanding of the particle impact on the performance. All TFN pore-open membranes exhibited less hydrophilic and rougher surface structure than TFC

and TFN pore-closed membranes. It is difficult to distinguish the surface hydrophilicity and roughness differences because of the polymer, the pore-state of the particle, and possible particle aggregation. The lower salt rejection performance of $TFN_{1\text{-}PO}$ membranes may indicate defects possibly because of particle aggregation of the small size of LTA-1 particles. The high desalination performance difference between $TFN_{3\text{-}PC}$ and $TFN_{3\text{-}PO}$ may because of the wide particle size distribution. Considering the performance and characterization results, LTA-2 particles (~150 nm particle size) can be a better fit to start for further permeability analysis.

4. MODEL MEMBRANES

4.1. Introduction

4.1.1 Polydopamine adhesion layer onto a microporous support membrane

Dopamine, a catecholic compound with a primary amine functional group, is a small protein inspired by mussels' adhesive proteins, as depicted in Figure 29 [154]. It can bind any organic and inorganic solid substrates under wet conditions (the catechol compound for the inorganic adhesion and the amine groups for the organic adhesion). Lee et al. showed a spontaneous film formation of dopamine solution via a self-polymerization process, in a typical marine environment, i.e., 2 mg of dopamine per milliliter of 10 mM Trizma Hydrochloride (Tris-HCl), pH 8.5 [154]. Furthermore, it allows secondary treatment for several applications, such as self-assembled monolayers, thermosetting adhesives, metal films, bioactive and bioinert surfaces, Figure 29 [155].

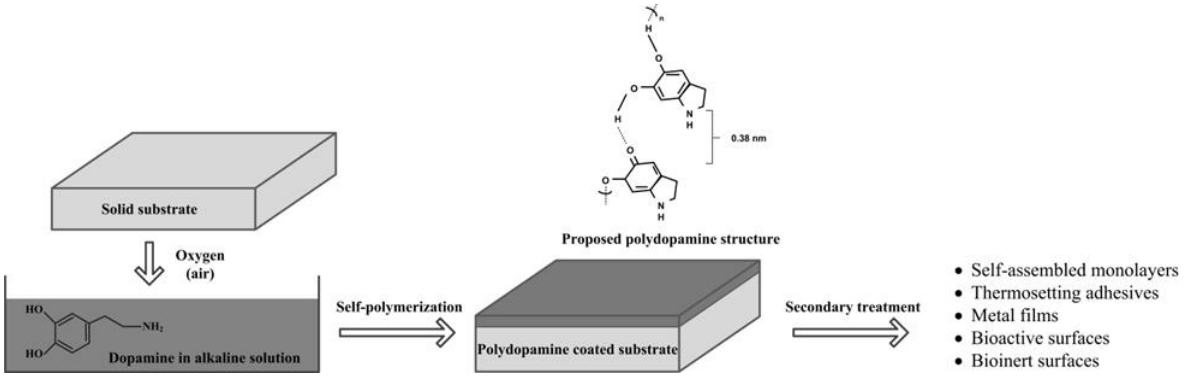

Figure 29: Schematic of dopamine self-polymerization on solid substrates and secondary treatment application areas.
The schematic is modified from [155], and a proposed polydopamine structure is reproduced from [156].

Figure 30 schematically depicts a polydopamine polymerization reaction and film deposition including a proposed polydopamine structure by Jiang et al. [157]. However, the actual polydopamine structure and the film deposition mechanism are not well

known. Dreyer et al. proposed another oxidation mechanism for polydopamine [156]. The dopamine self-polymerization occurs through oxidation steps in alkaline environments, and the resulting proposed polydopamine structure with non-covalent bonds is in Figure 29. In this structure, the non-covalent forces; charge transfer, π-stacking, and hydrogen bonding, holds the dopamine monomers together. Hence, the polydopamine coatings are insoluble and highly stable [156]. Conversely, Liebscher et al. proposed the covalent bonding in the structure [158]. The proposed covalent bonds link the benzene rings of dihydroxyindole and indoledione units in the structure through C−C bonds [158]. In the literature, there are at least ten different proposed polydopamine structures as summarized in [158].

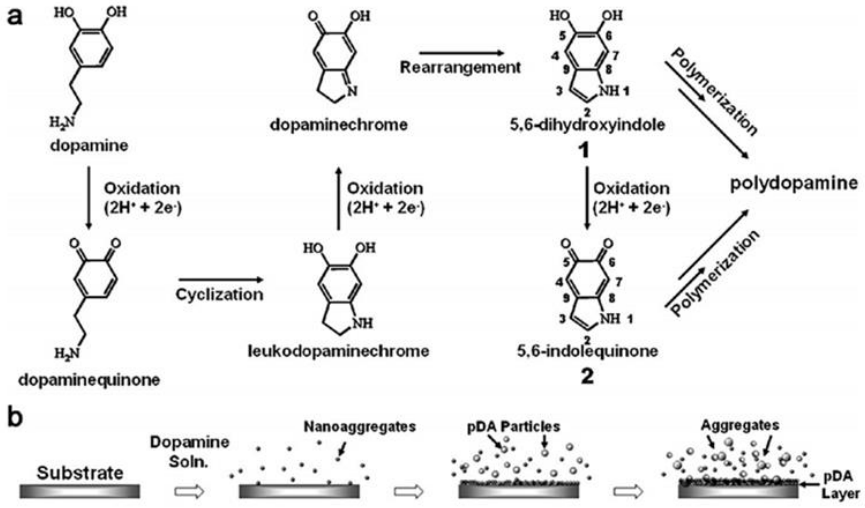

Figure 30: Dopamine polymerization mechanism (a) and the film deposition (b).
The figure is from [157].

The dopamine self-polymerization reaction kinetics are a function of the oxidant employed [159, 160], the solution pH, dopamine concentration [161], and the temperature [157]. Oxidant presence, such as potassium chlorate (weak oxidant) and sodium periodate (strong oxidant), increases the reaction speed in alkaline medium and

allows the reaction to occur in an acidic or neutral environment [159]. Under an oxygen environment, the reaction kinetics are faster, and the resulting film is highly uniform and smooth compared to polymerization under ambient air [160]. However, there is a maximum thickness limit for oxygen as an oxidant in the reaction [162]. The film becomes thicker and rougher with the dopamine concentration between 0.1 and 5 mg L^{-1} [161] (2 mg L^{-1} is the standard concentration for dopamine studies). Moreover, Jiang et al. observed that the polymerization rate and film thickness increased with temperature from 20°C to 60°C, without any significant change in surface morphology [157].

The thickness of the layer is also a function of the substrate immersion time in the alkaline solution. McCloskey et al. studied the pure water permeability of polysulfone ultrafiltration membrane as a function of dopamine deposition time, as given in Figure 31(a). For the deposition time of fewer than 4 hours, the polydopamine-coated polysulfone has high water permeance, >100 L m^{-2} h^{-1} atm^{-1}, to serve as a support membrane for polyamide thin film composite membranes (commercial polyamide TFC membrane water permeance: 2.0-3.0 L m^{-2} h^{-1} atm^{-1} for seawater and 3.0-5.1 L m^{-2} h^{-1} atm^{-1} for brackish water desalination [79]). Furthermore, Zangmeister et al. deposited polydopamine films at short deposition times, $\leq$ 10 min, and found a linear relationship between the film thickness and the deposition times, as shown in Figure 31(b) [163].

Recently, researchers have developed TFC membranes functionalized with a polydopamine coating to enhance the antifouling resistance of RO membranes [164, 165]. In these membranes, “mussel-inspired” [166] bio-coating, polydopamine is applied on the polyamide TFC membrane surfaces. These membranes exhibit improved

antifouling performance while maintaining similar separation performances to their uncoated counterparts.

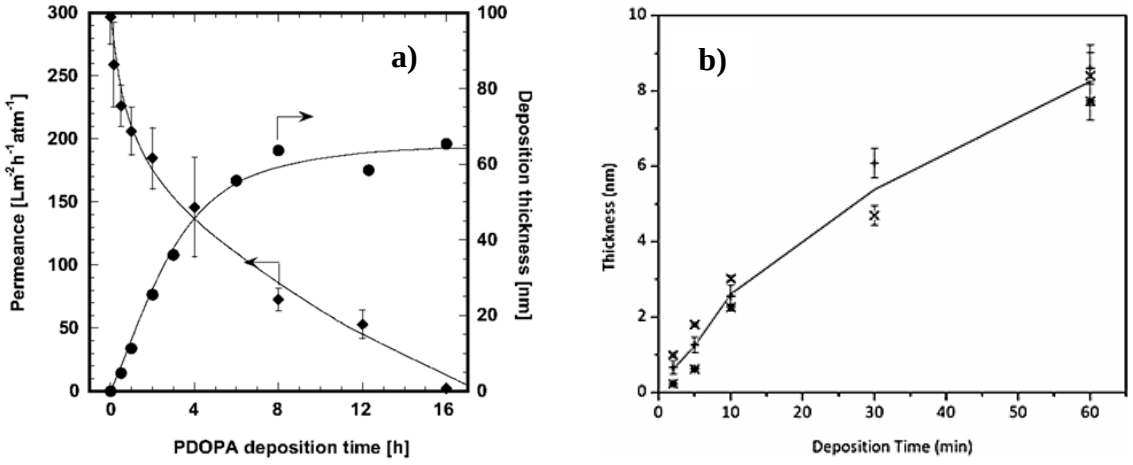

Figure 31: Polydopamine film thickness as a function of deposition time.
The figures are reproduced from (a) McCloskey et al. study on deposition time effect on the permeance of polysulfone ultrafiltration membrane [164] and (b) Zangmeister et al. study on the thickness of the polydopamine for short deposition times [163].

In this study, we use the polydopamine coating to adhere to the molecular sieve particles before the film formation (for the model membrane, on anodisc, inorganic support membrane and/or on polysulfone, polymeric support membrane) and the interfacial polymerization reaction (for thin film nanocomposite membrane, on polysulfone, polymeric support membrane). Ideally, this adhesion layer should be thin to minimize the hydraulic resistance of this layer, thick enough to create a uniform film and hold the particles.

4.1.2 Adhesion of particles on a polydopamine-coated support membrane

Immobilization of particles via polydopamine coating enables a facile method for various applications. For instance, Zhang et al. stabilized TiO_2 nanoparticles [167] and

Yang et al. immobilized silver particles [168] on TFC membranes via polydopamine coating to enhance the antimicrobial property. Also, GhavamiNejad et al. coated ZSM-5 zeolite with polydopamine to immobilize silver nanoparticles on the surface of the mesoporous zeolite [169]. Moreover, Fei et al. applied the polydopamine coating on carbon nanotubes to disperse gold on the outer surface of the nanotube [170].

Therefore, to anchor the molecular sieves to the support, in this study, we used the polydopamine film coating on the porous support with the particles immobilized as a secondary treatment on that layer. We adapted the dip-coating method used for polydopamine and molecular sieves particles on various types of support membranes from a previously published report [167]. In this research, we synthesized the layer with pore-opened and pore-closed LTA particles on polydopamine-coated ultrafiltration polysulfone organic membrane with a pore size less than 0.01 µm and Anodisc inorganic membrane with 0.02 µm pores. We studied the layer with various particle sizes (100-300 nm, polyamide active layer thickness limits the range) and particle contents (depends on the particle size and overall membrane performance). We tested the membranes to identify the optimum particle size and content for resistance analysis based on the overall membrane performance results. Furthermore, to enhance the particle stability on the polydopamine layer, the grafting of amine functional groups on the zeolites with 3-aminopropylmethyldiethoxysilane (APMDES) silane agent can be used in future, described by Nik et al. [171].

4.1.3 Thin film nanocomposite model membrane

The ultrathin, highly selective aromatic polyamide layer typically synthesizes *in situ* by the interfacial polymerization reaction of m-phenylenediamine (MPD) and

trimesoyl chloride (TMC) monomers. The amine in water and acid chloride in an organic solvent react at the liquid-liquid interface, close to the organic phase [40] on a microporous support. As a result of the bifunctional amine and the trifunctional acid chloride monomers reaction on the support, the aromatic polyamide film has a crosslinked structure, as shown in Figure 10(b).

In a conventional polyamide interfacial polymerization membrane synthesis, as discussed in Chapter 3, first the microporous support is soaked in an aqueous diamine solution, and then the excess solution is removed by various methods such as air drying, rolling, applying air-knife for a uniform surface. Then, the amine saturated support contacts an acid chloride in the organic phase to form the polyamide, followed by curing and rinsing steps to enhance the structure.

We have developed a synthesis protocol and optimized parameters for the TFC and TFN membrane synthesis in our laboratory. For this polyamide TFN-model membrane synthesis, we updated the synthesis protocol. Figure 32 summarizes membrane synthesis stages with the significant parameters of each step. For the TFN-model membrane synthesis, the first three steps are critical because of the presence of the polydopamine adhesion layer. This layer holds water more than uncoated support and the layer changes the support porosity which can affect the MPD coating performance. Therefore, we focused on the three steps at the beginning. After several modifications; we achieved successful polyamide film formation on the particle coated adhesion layer.

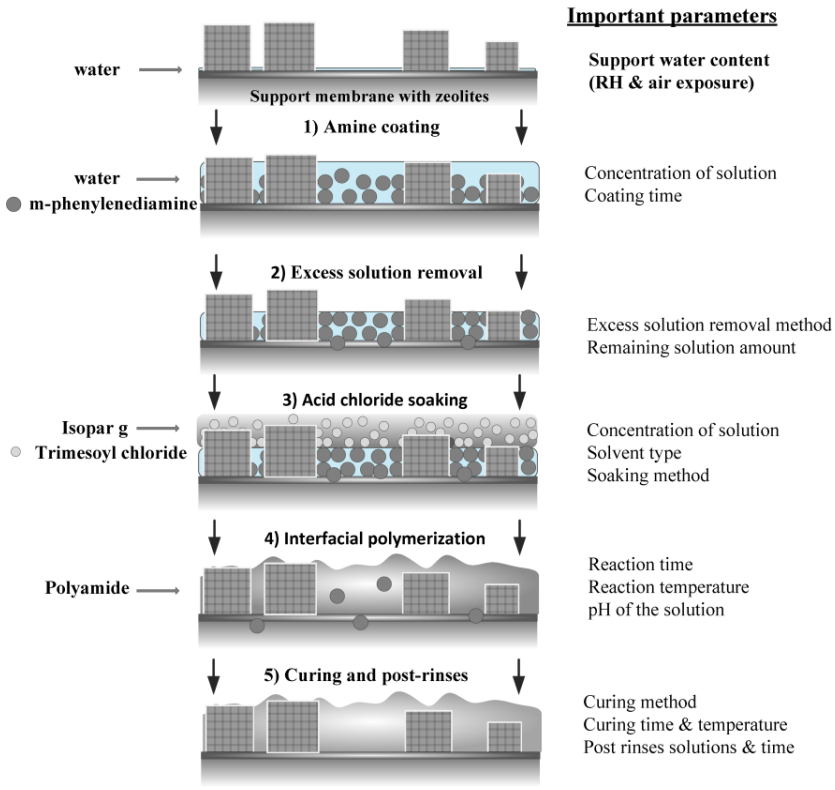

Figure 32: Interfacial polymerization synthesis stages for TFN-model membranes. The significant parameters of each step are at the right. For the model membranes, the water content of the support before and after amine coating is critical.

4.1.4 The water-impermeable polymer matrix model membrane

The impermeable polymer can simplify the resistance model analysis for determining the particle permeability, also can reduce the experimental error caused by the polymer water permeation in TFN-model membrane experiment. For the impermeable polymer, we selected Poly(vinylidene chloride-co-acrylonitrile) (P(VDC-co-AN) polymer material because of its optical transparency, excellent barrier property to water, and mechanical strength. We developed a free-standing model membrane to study transport behavior of mixed matrix membranes containing molecular sieve particles. In our preliminary studies, to synthesize model membranes, we were using the solution

casting method via spin coating. We dissolved 18 wt% P(VDC-co-AN) polymer powder in a solvent of tetrahydrofuran (THF) and dimethylformamide (DMF) organic solvents (60:40 in wt%). To suspend the zeolites in the solution, we had to use this high polymer content which may cause a particle/polymer gap in the structure. We could control the thickness of the membrane by changing the spin rate and acceleration of the spin coater. Decreasing the particle size enhances the particle-polymer adhesion [172] (the surface area to volume ratio increases and more interfacial area between the filler particles and polymer occurs). Furthermore, it may increase the water permeation performance of the membrane because of the shorter permeation path. However, the freestanding membrane feature limits the minimum thickness of a defect-free model membrane as 5 μm. Thus, the particles within the membrane had to be ~5-10 μm size. After drying in the humidity controlled box at room temperature for two days, we peeled-off the film by rolling on a high radius beaker under water to eliminate the defects. Finally, we applied oxygen plasma etching to remove the barrier polymer on the surface of the zeolites on both sizes. Figure 33 depicts the summary of the free-standing model membrane synthesis.

We conducted dead-end hydraulic permeation testing to determine the pure water flux of the model membranes. Before loading the membranes into the dead-end cell, we transferred the membranes on polysulfone support to provide additional mechanical strength. After the performance test, we could determine the zeolite content in the membrane structure by selectively staining the particles with Nile Blue A dye. The dye can stain the FCC matrix of the zeolite (red color) under a high fluorescence at 638 nm laser [173]. The method could optically image the membrane structure with depth profiling using confocal microscopy, as shown in Figure 34. The optical section analysis

could provide the actual number of zeolite particles incorporated into the water transport during permeation test. The zeolite content determination with confocal microscopy could enhance the accuracy of our approach for the permeability analysis of the freestanding water impermeable model membranes.

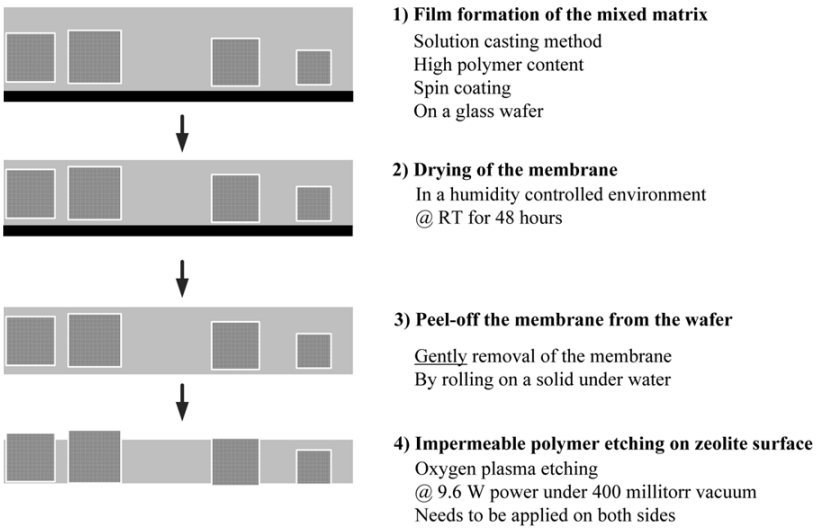

Figure 33: The free-standing water impermeable polymer model membrane synthesis.

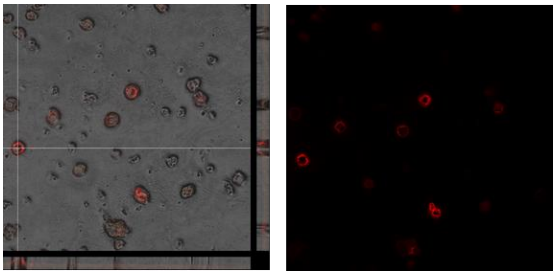

Figure 34: Confocal microscopy image of a free-standing water impermeable polymer model membrane contains stained pore-opened zeolite.

We observed salt selectivity on the interface (~30% salt rejection), but in our early design, the permeability and selectivity results were not reproducible. We have identified the possible reasons for this issue; (1) the thick film and the big particles may cause the poor adhesion, (2) peeling-off the membranes from the wafer may create

defects, (3) applying oxygen plasma etching on both sides of the membrane may damage the film integrity. Therefore, we have modified the model membrane to address the issues. Our revised model membrane design includes; support instead of a free-standing film, sub-layer holds stabilized particles on the support and an impermeable polymer top-layer which contains the stabilized particles. In the modified design; (1) the film thickness and the particle sizes can in nano-size range (~300-500 nm) (particle size reduction from the micrometer scale to this nanometer scale affects the particle performance because as the particle size decreases the particles' surface area and surface activity increases [135]), (2) the support usage eliminates the peeling off step (the peeling-off step increases the risk of defects), (3) the impermeable polymer cannot be underneath of the stabilized particle, and so only top layer oxygen plasma etching is required (provides easier membrane synthesis).

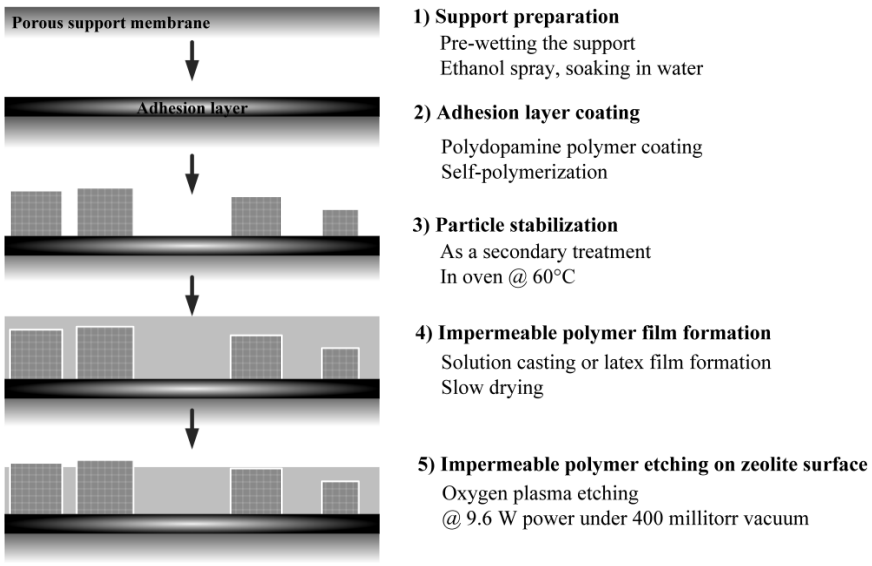

Figure 35: The modified water impermeable polymer model membrane synthesis.

For our modified model membrane, after the particle immobilization, we applied the water impermeable polymer. In a free-standing model design, we had to coat using

solution casting method with high polymer content. Conversely, in this design, we can cover with lower polymer content solution (1-5 wt%) because there is no need to suspend the particles in the solution anymore. Nevertheless, we need to investigate the polydopamine coating stability for the solvents in the solution casting method. Alternatively, the modified design enables to coat the impermeable layer via latex film formation. Since water is the dispersion medium during the latex film formation and polydopamine is a water-resistant material, we do not need to investigate the stability of the adhesion layer vigorously. Therefore, latex film formation is a viable option for the modified design.

A continuous latex film formation from water impermeable latex particles mainly comprises (1) water evaporation, (2) latex particle deformation, and (3) film coalescence steps [174], schematically described in Figure 36. In the water evaporation step, the deposited latex solution onto porous support loses water at a constant rate and becomes a dense pack of spheres. In the second stage, the concentrated latex particles deformation into rhombic dodecahedra occurs [175]. Because, as water evaporation rate decreases, the resulting drying forces create capillary pressure between the latex particles. As a result of this pressure, diffusion across particle-particle boundaries occurs, and fragile void-free film formation starts in this stage [175]. In the third stage, because the thin film has a lower surface area than the individual particles, to reduce the total surface area, the deformed latex particles coalesce into a continuous film. The coalescence of the polymer chains provides mechanical strength to latex film [176]. Moreover, annealing above Tg increases the degree of chain inter-diffusion, thus enhances the strength of the latex film [176]. Furthermore, to have even film formation, the ambient temperature needs close to

the minimum film formation temperature (MFFT, which is related to thermal glass transition temperature, Tg) [176]. This latex film formation principle is similar for soft (low Tg) and hard (high Tg) latex polymers, except the latex particle deformation stage. For hard latex polymers, initially, void formation appears before the diffusion across the particle boundaries than after successive annealing the voids disappear with the evaporation of all water [177]. In addition to the void formation in hard latex polymers, annealing may take a long time for hard latexes film formation [176].

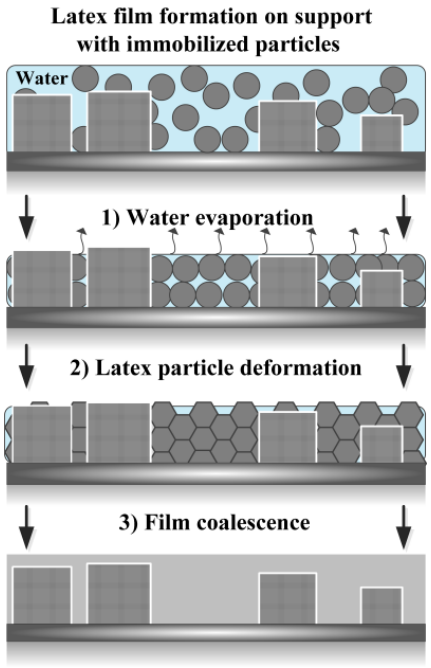

Figure 36: The water impermeable latex film formation for the model membrane.
The support with the immobilized particles is dip coated with the latex solution. The latex film forms after (1) water evaporation, (2) particle deformation, and (3) film coalescence stages. Oxygen plasma etching is necessary to remove the impermeable top layer on the zeolites after the film formation. Polymer nanoparticles are spherical and hexagonal, and porous molecular sieve particles are cubic.

In our group, Khosravi et al. studied the latex film formation on porous materials [178]. Latex particle type, size, and crystallinity; latex concentration; pore size of the support; and water evaporation rate profoundly affect the resulting film quality [178].

Soft latex particles on small pore size support with slow evaporation rate exhibited continuous, homogenous film, such as the latex film of PVDC latex on polysulfone or anodisc membrane under high humidity drying environment (the film presented an excellent water barrier property) [178]. Furthermore, Ugur et al. examined the latex particle size and inorganic particle content on the polystyrene latex/TiO_2 nanocomposite latex film formation [177]. They observed continuous film formation with small latex particles and low and moderate inorganic content. The high inorganic content does not allow to form a continuous film mainly because the particles hinder the chain interdiffusion [177].

In this study, to make defect-free impermeable polymer layer within the thickness of the particle, we were planning to study a water impermeable PVDC soft latex film formation with different latex concentration (<10 %), at different drying and annealing conditions. After oxygen plasma etching, we could conduct stirred dead-end cell tangential flow, hydraulic permeation testing at 200 psi to determine the pure water flux (their salt selectivity can indicate the defect-free nature of the membranes). However, the studied pore-closed-and pore-opened particle size range was outside the thickness range for defect-free water impermeable PVDC membrane synthesis. Therefore, the water impermeable model membrane was developed but not studied for water permeance.

4.2. TFN-Model membrane experimental methodology

4.2.1. Materials

Chemicals used in this study are referred to with the following nomenclature. For dopamine polymerization, a polysulfone coated non-woven polyester ultrafiltration membrane (PSf; NanoH_2O) was used as a support membrane. Dopamine hydrochloride

(dopa; Sigma-Aldrich), Trizma hydrochloride (Tris-HCl, reagent grade; Sigma-Aldrich), and sodium hydroxide (NaOH; Sigma-Aldrich) were used for dopamine solution.

For the membrane synthesis, monomer solutions: meta-phenylenediamine (MPD, 99%; Sigma-Aldrich) in ultrapure deionized water (UPDI water, Milli-Q Advantage A10; Millipore), and trimesoyl chloride (TMC, 98%; Spectrum) in organic solvent Isoparrafin-G (Isopar-G, technical grade; Gallade chemical) were prepared for the synthesis of the thin polyamide film. The post-cure rinses consisted of solutions of sodium hypochlorite (NaOCl, reagent grade; Sigma-Aldrich) and sodium bisulfate (NaHSO4, reagent grade; Sigma-Aldrich). The salt rejection performance test was run with sodium chloride (NaCl, ACS grade; Sigma-Aldrich).

4.2.2. Polydopamine adhesion layer synthesis

For the support preparation before polydopamine coating, a sheet of polysulfone coated polyester support membrane (8.5" x 4.5") was sprayed with ethanol (~20 mL), then rinsed with 500 mL running ultra-pure deionized (UPDI) water, and stored in a bottle filled with one liter of UPDI water overnight to ensure the membrane is thoroughly wet before casting. For the adhesion layer synthesis, first, we prepared 10 mM Tris-HCl buffer solution in UPDI water at pH 8.5 (pH electrode, double junction ATC; Fisher Scientific) using sodium hydroxide. The dopamine solution was prepared as a concentration of 2 mg mL^{-1} dopamine hydrochloride in the buffer solution. The membrane is removed from the bottle, rinsed with 500 mL UPDI water. Within the ten minutes of removing from the storage bottle, the membrane was taped on all sides onto a glass plate (9" x 5"). Then, we soaked the support into 100 mL of dopamine hydrochloride solution for two minutes with the active side (PSf side) facing down in the

solution under ambient air. We also investigated the impact of one, four, and ten minute deposition times under ambient air. After lifting the plate from the dopamine solution, the plate was held vertically at ambient air for two minutes to further polymerization. Then, the membrane rinsed with UPDI water to remove unreacted monomers. After, the plate was held vertically for five minutes before the particle adhesion.

4.2.3. Particle adhesion on polydopamine

To immobilize the molecular sieves to the support, we applied the secondary treatment method on the polydopamine film coated support membrane. The procedure was adapted from a previously published report [167].

After the five minutes of polydopamine coating procedure, the plate was placed horizontally as active side up, into a conventional oven at 60°C. Immediately after, the coating solution was poured on the membrane. The membrane was held for 30 minutes (the solution still covers on the membrane surface after the 30 minutes). The remaining solution was poured into a waste bottle and the membrane placed into a one-liter UPDI water dish to rinse. Next, the membrane was lifted from the water, and the plate was held vertically at ambient air for five minutes. The resulting support membrane was removed from the plate and was placed into one liter of UPDI water in a light-proof Nalgene bottle for an overnight before the polyamide polymerization.

The only difference for the TFC_{dopa} support synthesis procedure from TFN_{dopa} support synthesis procedures is that the coating solution does not contain particles, only Tris-HCl solution. The coating solution for particles in a Tris-HCl solution containing 5 mg zeolite particles ultra-sonicated at ~20 °C for 30 minutes and sonicated with

probe (FS-300N; Shanghai Shengxi Ultrasonic Instrument) for 3 minutes. The sonicated solution was poured immediately on the polydopamine-coated support in the oven.

4.2.4. TFN-model membrane synthesis

Our casting procedure is based on previously published methods [54, 55, 58]. All the membranes were cast based on the same polyamide interfacial polymerization. Thin film composite (TFC) membranes are neat polyamide membranes without nanoparticles, and dopamine coating, (TFC_{dopa}) membranes are thin film composite on polydopamine-coated support, (TFN_{dopa}) membranes are thin film nanocomposite on polydopamine-coated support with immobilized particles. The only difference is the support property, i.e., polydopamine coating, the presence of particles, and pore-state of particles.

For the casting, first, we prepared the 3.5 wt.% MPD in UPDI water and 0.15 wt.% TMC in organic solvent monomer solutions separately. The solutions were magnetically stirred at 300 rpm at room temperature for at least 3 hours before use. The membrane is removed from the bottle, rinsed with 500 mL UPDI water. Within the twelve minutes of removing from the storage bottle, the membrane was taped on all sides onto a glass plate (9” x 5”) (the timing for the taping can be adjusted based on the temperature and the humidity of the room since support property affects the resulting membrane performance). The polydopamine coated membranes hold water on the surface. To remove the water on the membrane surface, we applied air knife air knife (Super air knife, Exair) operating at 40 psi. Then, we soaked the support into 150 mL of MPD in UPDI water monomer solution for two minutes, with the active side (PSf side) facing down in the solution and the back of the plate not submerged. After lifting the plate from the amine solution, to increase the uniformity of the membrane surface, we

removed the excess solution from the surface evenly using an air knife (Super air knife, Exair) operating at 60 psi. Then, we immediately placed the MPD coated membrane vertically into 200 mL of TMC in isopar-G monomer solution in a vertical membrane brick for the interfacial polymerization reaction for one minute. After, we removed the plate from the brick and held it vertically for two minutes. We cured the membrane through a series of post-treatment rinses. First, the membrane was placed in a water bath at ~95 °C with the active side up for two minutes. Then, we applied chlorine-sulfate treatment to remove unreacted MPD in the membrane structure. First, the membrane was removed from the glass plate and placed into 1.5 mL L^{-1} NaOCl in deionized water for two minutes. Next, the membrane was placed into 1 g L^{-1} $NaHSO_4$ in deionized water for 30 seconds. Finally, the membrane was placed in a freshwater bath at ~95 °C with the active side down for two minutes. The resulting membranes placed into one liter of UPDI water in a light-proof Nalgene bottle and stored at 4°C until testing.

For this work, we synthesized TFC and TFC_{dopa} membranes as control and two types of polyamide/LTA zeolite thin film membranes with different zeolite pore-state (using pore-closed and pore-opened LTA-2 particles in Chapter 3). The names of each membrane set are TFC, TFN_{dopa}, $TFN_{dopa\text{-}PC}$, and $TFN_{dopa\text{-}PO}$. We named the TFN membranes according to the nomenclature $TFN_{dopa\text{-}PX}$ where X represents pore state (O – opened, or C – closed).

4.2.5. Membrane performance for TFN-model membranes

The hand-cast membranes were tested for water permeability and sodium chloride (NaCl) salt rejection, using a custom fabricated, cross-flow reverse osmosis test system as depicted in Figure 19. In the cross-flow system, the feed flows across the membrane

surface in a direction normal to the direction of transport across the membrane. The tests were run at 200 psi of applied hydraulic pressure with UPDI water and saline waters (2,000 ppm NaCl). All tests were conducted at 20 ± 1°C with a cross-flow rate of 0.5 gpm. After stabilization (overnight compaction), the permeate flow rate was measured with a flowmeter (FlowCal 5000; Tovatech). The permeate and the feed conductivities were measured using temperature compensated two-cell conductivity probes, connected to a meter (Accumet Excel XL50; Fisher Scientific), to calculate the observed membrane salt rejection. At least triplicate membrane samples were tested.

4.2.6. Characterization methods

The support membranes and the polyamide membranes surface and cross-section morphology were analyzed using scanning electron microscopy (SEM, Amray 1910 field emission scanning electron microscopy; Amray) at a 5-15 kV beam accelerating voltage at various magnifications. Dried membrane samples were sputter coated with gold for 25 seconds using Cressington 108 Auto Sputter Coater before SEM analysis. Atomic force microscopy (AFM, Dimension Multimode 8; Bruker) was used to determine the roughness of the membrane surface. The tapping mode performed because the tip can easily damage the polymer while scanning the 5x5 μm^2 scan area at a fixed scanning rate of 1 Hz. The probe (FMV-A; Bruker) tip radius was 8—12 nm, the cantilever length was 225—235 µm with a spring constant of 2.8 N m^{-1}. Attenuated total reflectance–Fourier transform infrared (ATR–FTIR, 6700 FTIR; Thermo Nicolet) with diamond crystal smart orbit provided an insight into the functionality of the particles, and a thin film of the adhesion, adhesion-particle, model, and TFN membranes. We dried the membrane samples in a desiccator overnight before ATR-FTIR measurement. The contact angles of

the membranes were measured using de-ionized water sessile drop contact angle analysis (Easy Drop; Krűss) to evaluate surface hydrophilicity of all membranes. The drop volume of the water was two μL. On each air-dried membrane sample, we measured twelve spots. We removed the highest and the lowest values and reported the average value of the remaining measurements.

4.3. Results for TFN-model membrane experiment

The crosslinked polyamide polymer TFC and TFN membranes synthesized via the MPD/TMC interfacial polymerization reaction. As mentioned earlier, this reaction is complex and highly sensitive to the synthesis conditions. Moreover, the polydopamine self-polymerization reaction is also a complex reaction. Before the interfacial polymerization, we characterized the surface morphology of polydopamine coated supports. For this study, our aim was the synthesis of the model membrane with low particle content to ensure the minimum particle aggregation. We also coated the polydopamine at short coating time (2 minutes), to lower the polydopamine effect on the polyamide polymerization. Figure 37 depicts the representative SEM and AFM images of the supports in this study. The particles on the polydopamine-coated layer were single particles. We could easily count the particles on the support surface through SEM analysis. The distribution of the particles was uniform. Moreover, the AFM analysis indicated a similar pattern with slightly increased roughness for the polydopamine-coated supports.

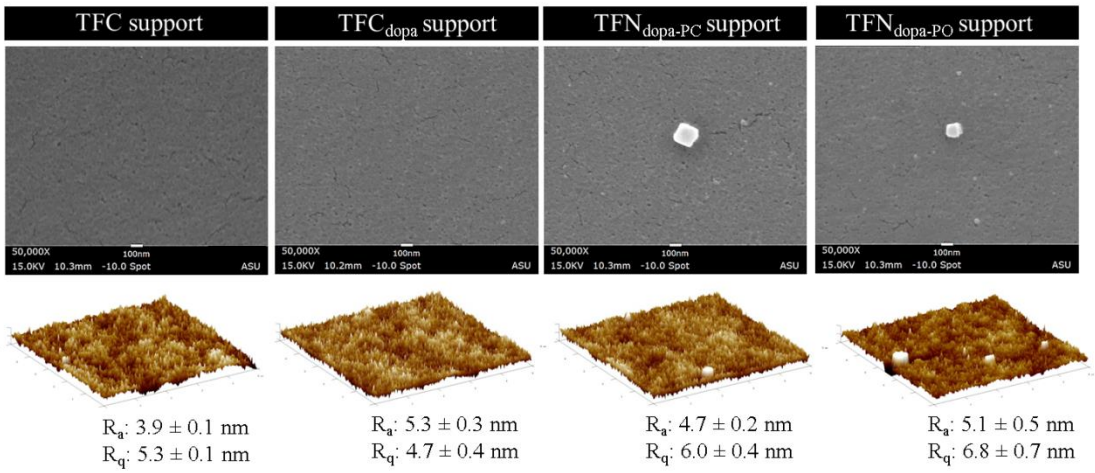

Figure 37: Representative SEM surface images and AFM 3-D images of the supports. The neat microporous polysulfone support (TFC support), the support with a polydopamine coating layer (TFC$_{dopa}$ support), the polydopamine-coated support with pore-closed particles (TFN$_{dopa-PC}$ support), and the polydopamine-coated support with pore-opened particles (TFN$_{dopa-PC}$ support).

We assessed the impact of the polydopamine coating and particle addition on the resulting polyamide polymer. First, we analyzed the membrane surface morphology using SEM to confirm the polyamide film formation. Figure 38 shows the resulting polymer structure on the supports (pictured in Figure 37). The membranes exhibit similar MPD/TMC polyamide surface morphology and successful polyamide formation on the supports.

AFM analysis provided the quantitative surface roughness morphology for the resulting membranes. The membranes with polydopamine-coated support have higher roughness compared to TFC membranes. TFC$_{dopa}$ membrane surface has highest average roughness with large standard deviation, Ra, of 92 ± 19 nm whereas TFC membrane surface has Ra of 66 ± 8 nm. Moreover, TFN$_{dopa}$ membranes with pore-closed particles exhibited similar average roughness surface morphology 73 ± 8 nm and 72 ± 8 nm and

within the TFC membrane roughness range. Figure 39 presents AFM surface roughness results and representative three dimensional AFM images for the membranes.

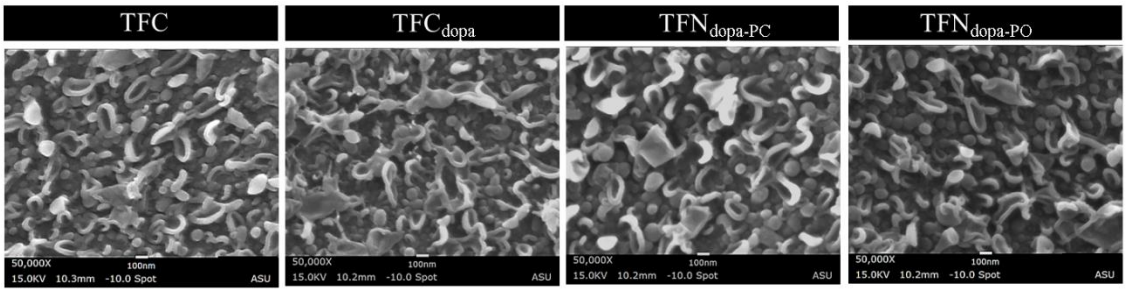

Figure 38: SEM images of the membranes on neat, polydopamine-coated, and polydopamine with pore-closed and pore-opened particles support.

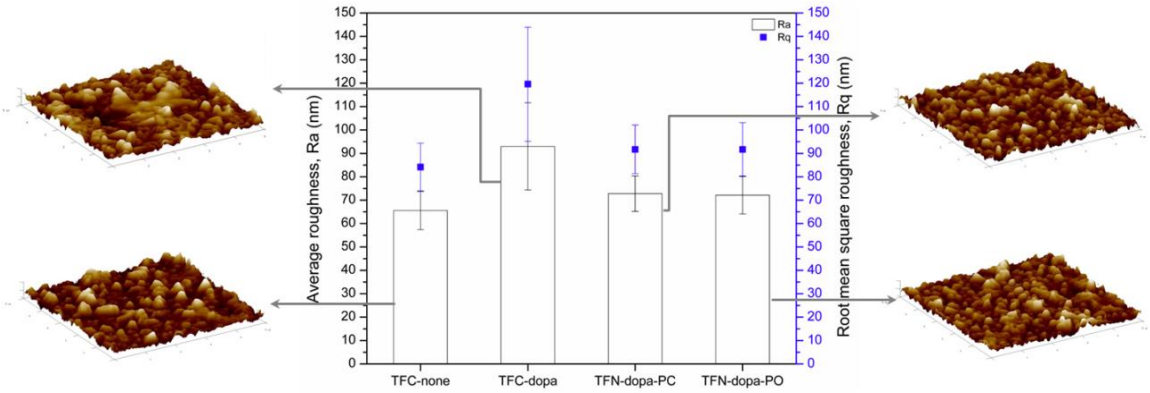

Figure 39: AFM results of hand-casted TFC, TFC$_{dopa}$, and TFN$_{dopa}$ membranes for roughness including representative three-dimensional images.

To investigate the surface hydrophilicity of the membranes, we performed contact angle analysis. A hydrophobic surface has a contact angle higher than 90°, and the surface hydrophobicity enhances with the contact angle increases. Because of the presence of hydrophobic polydopamine coating, other researchers have found that the material shows a high pure water contact angle than corresponding neat support polymer. Figure 40 shows measured contact angles of the membranes. TFC membranes exhibit the lowest contact angle compared to TFC$_{dopa}$ and TFN$_{dopa}$ membranes incorporated pore-

closed and pore-opened LTA-2 particles. Therefore, the polydopamine-coated support membranes are more hydrophobic compared to neat support membranes. Moreover, a hydrophilic surface has a contact angle lower than 90°, and the surface hydrophilicity enhances with the contact angle decreases. Because of the presence of hydrophilic nanoparticles in the structure, TFN_{dopa} membranes exhibited lower contact angles compared to TFC_{dopa} membranes. The contact angle can be lowered with high hydrophilic zeolite content. However, in this study, we chose to employ low particle content in the structure to minimize the aggregated particle in the permeability analysis.

As discussed in Chapter 3, surface roughness has a strong effect on the wetting property of a material, and corresponding contact angle even when Rq is less than 100 nm [149]. The measured contact angle can be corrected considering the surface roughness [149]. However, in this study, the membranes exhibited contact angle within a transition state of the hydrophilicity-hydrophobicity surface property. Therefore, we did not apply the contact angle correction for rough surfaces in this study.

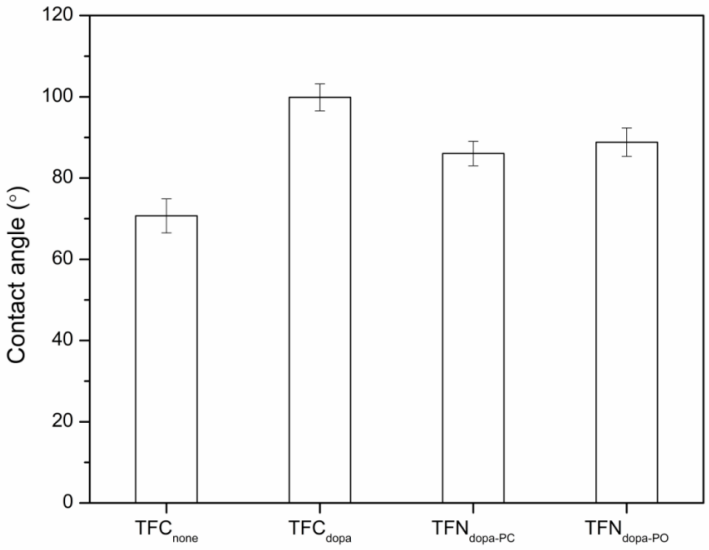

Figure 40: Measured contact angles hand-casted of TFC, TFC_{dopa}, and TFN_{dopa} membranes for hydrophilicity.

For the chemical functionality of membranes, an FTIR analysis was performed. Figure 41 depicts the FTIR spectra of the polysulfone support and hand-cast TFC, TFC_{dopa}, $TFN_{dopa\text{-}PC}$ and $TFN_{dopa\text{-}PO}$ membranes. For polyamide structure, we focused on characteristic peaks at ~1,540 cm^{-1}, at ~1,609 cm^{-1}, and ~1,663 cm^{-1}, and at 1,734 cm^{-1}, which correspond to the C─N stretch of amide II band, the aromatic amide band, the amide I band, and the C═O carboxylic acid band [58, 59]. The FTIR spectra of the TFC and TFN membranes confirm the successful polyamide formation on the polysulfone support. However, TFC_{dopa} membrane has a broken spectrum at the polyamide characteristic peaks. The film formation for this membrane might not be uniform and/or thinner than the other membranes. For TFN_{dopa} membranes, we observed an increase in polyamide characteristic peaks at ~1,540 cm^{-1}, at ~1,609 cm^{-1}, and ~1,663 cm^{-1}. We did not observe significant signal for the absorbance of the carboxylic acid peak of the membranes.

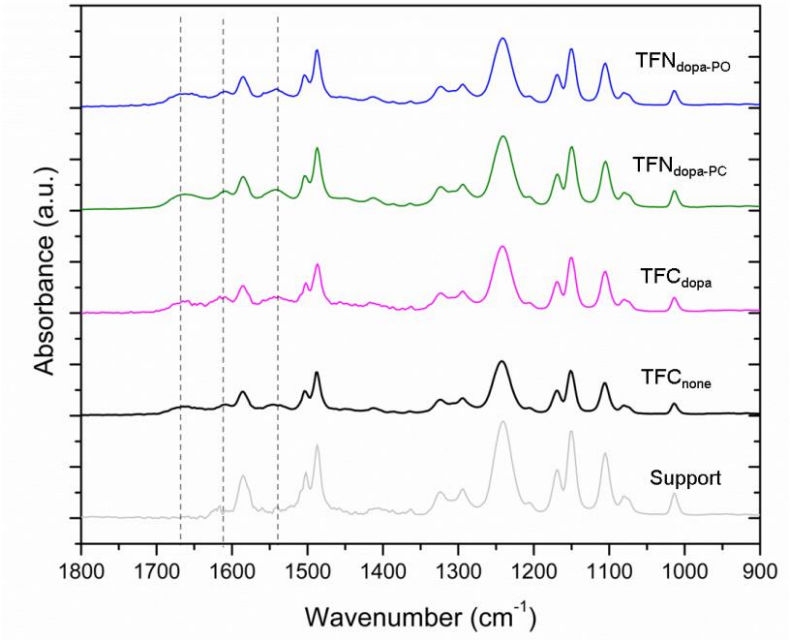

Figure 41: FTIR spectra of the support and the hand-casted TFC, TFC_{dopa}, and TFN_{dopa} membranes for functionality.

Figure 42 presents pure water permeance and salt rejection for all hand-cast membranes. The membranes with polydopamine-coated support exhibited higher water permeance than the base TFC membrane. However, TFC membrane showed the highest salt rejection, the dopa membrane performance can be improved with additional synthesis optimization. The water permeance increased with the particle presence. The dopa membranes have similar salt rejection performances, ~92% and 4% lower than TFC membrane salt rejection performances.

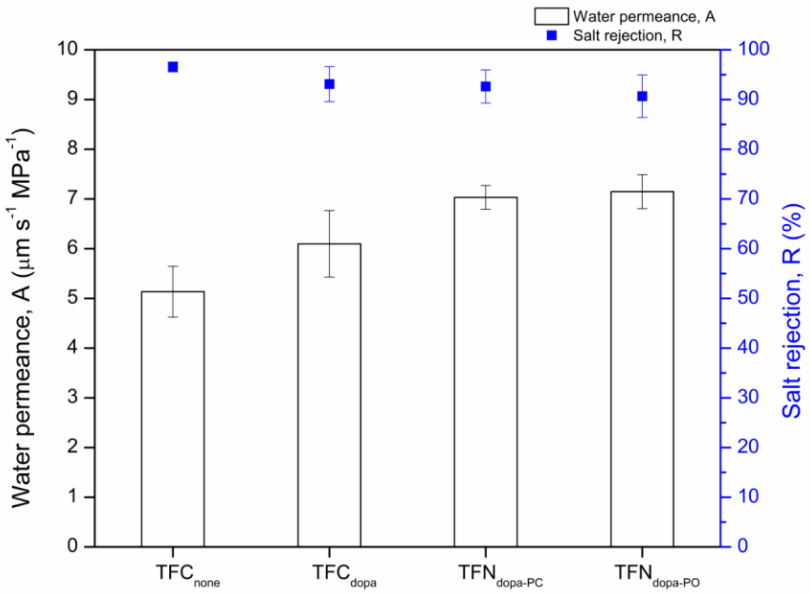

Figure 42: Water permeance and salt rejection performances of the hand-casted TFC, TFC_{dopa}, and TFN_{dopa} membranes.
The membrane synthesis occurred at 28% relative humidity and 20°C room temperature.

4.4. Conclusion

Thin film nanocomposite membranes synthesized via interfacial polymerization on particle immobilized support method were investigated for the impact of zeolite pore-state on the membrane performance (water permeance and salt rejection), membrane surface morphology, and structure. To minimize the effect of the aggregated particle on

the performance and the particle number differences between the pore-closed and pore-opened particles, we used low particle coverage for the particle immobilized support. Pore-opened of the particles on the water permeance was slightly higher than the pore-closed particles. However, more analysis is required for determining the particle permeance. The polydopamine coated support with immobilized particles might provide additional freedom to tune for TFN membranes, however, the coating may increase the complexity of the membrane synthesis processes.

5. INVESTIGATION OF WATER PERMEATION

5.1. Introduction

Chapter 3 discusses the conventional synthesis methods of TFN membranes incorporated with non-porous and nanoporous zeolite particles and reports water permeance values of these membranes. As previously mentioned, challenges like particle aggregation, non-uniform dispersion, possible particle leaching, and unknown particle content may increase the uncertainty of water permeance analysis. To address this, in Chapter 4 we developed a TFN-model membrane synthesis methodology (which has immobilized particles on the polydopamine-coated support) and evaluated the performance of these membranes. However, the work presented in Chapter 3 and Chapter 4 does not isolate the individual contributions (of nanoporous materials, the interface with the polymer, and the polymer) to the water transport. Therefore, in this chapter, to describe and isolate the impact of each possible pathway, we apply the resistance model to the results of Chapter 3 (TFN) and Chapter 4 (TFN-model).

The resistance model describes water transport through multi-phase or multi-component membranes, such as thin film composites for water and gas separations and has been applied to mixed matrix membranes [179-183]. This model treats fluid flow through multi-component membranes as analogous to the flow of current through resistors [180] in the presence of a potential difference. As illustrated in Figure 43, the water flow occurs in one direction through the membrane. The resistance of a material, *R* (s MPa μm^{-1}), is related to the water permeance, A (μm s^{-1} MPa^{-1}), and active layer thickness, L (μm), as defined in equation 5.1.

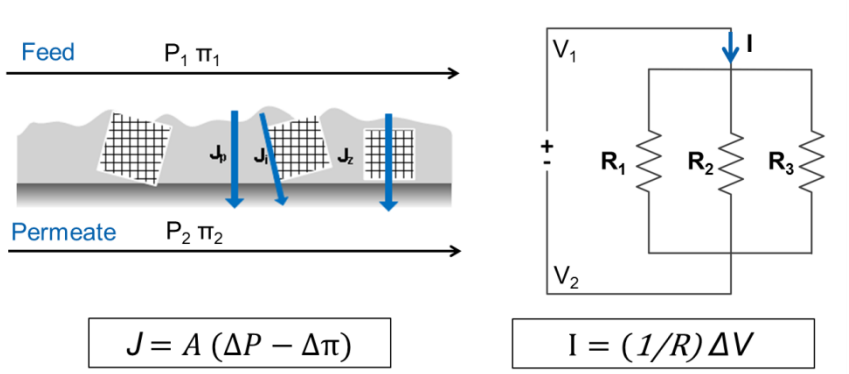

Figure 43: Water flow through TFN membranes is analogous to the current flow through the resistors.

$$R = \frac{L}{P} = \frac{1}{A} \qquad \text{Equation (5.1)}$$

In TFN membranes, the average size of the zeolite nanoparticles is nearly equal to the thickness of the polyamide layer [54]. Therefore, we first considered the thin film polymer and the nanoparticles as parallel resistances, otherwise called the *resistance in parallel* model, which is mathematically described in our publication and in Equation 5.2 [76].

$$\frac{1}{R_{membrane}} = \frac{\nu_{polymer}}{R_{polymer}} + \frac{\nu_{interface}}{R_{interface}} + \frac{\nu_{z\ pores}}{R_{z\ pores}} \qquad \text{Equation (5.2)}$$

In the equation, $R_{polymer}$, $R_{interface}$, and $R_{z\ pores}$ are the individual resistances of the polymer matrix, polymer-particle interface, and zeolite interior pore, and ν represents the percent occupied area by a particular component; the polymer ($\nu_{polymer}$), the interface ($\nu_{interface}$), and the zeolite pores ($\nu_{z\ pores}$). $R_{membrane}$ is the overall resistance of the membrane which is directly calculated from the measured data.

Although the parallel resistance model is a reasonable approximation for TFN membranes, it does not take particle size and the polymer thickness differences into account. Since in TFN membranes, the membrane integrity at high pressure is essential for effective desalination, the probability of having a polymer thickness significantly smaller than the particle size is low. Hence, as an alternative model, we considered that the polymer thickness can be slightly larger than the particle size. In this case, any polymer on the top or bottom particle surfaces can be considered as a series resistance. Figure 44 depicts the hybrid (series-parallel) resistance model.

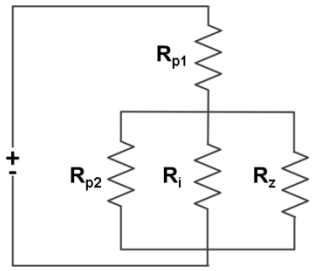

Figure 44: Hybrid resistance model of the membrane which takes particle and polymer thickness into account.

5.2. Application of resistance model to TFN and TFN-model membranes

For the parallel resistance model, we first obtained $R_{polymer}$ from the TFC membrane water permeance. Then, we assumed that $R_{polymer}$ for the TFC is identical to $R_{polymer}$ for the TFN membranes. For pore-closed TFN, the flow occurs only possibly through the polymer and the polymer-particle interface. So, $R_{membrane}$ is a function of only $R_{polymer}$ and $R_{interface}$. Finally, from the pore-opened TFN water permeance results, we can estimate $R_{z\ pores}$ through rearranging Equation (5.2):

$$R_{z\,pores} = \frac{\nu_{z\,pores}}{\frac{1}{R_{membrane}} - \frac{\nu_{polymer}}{R_{polymer}} - \frac{\nu_{interface}}{R_{interface}}} \qquad \text{Equation (5.3)}$$

For TFN-model membranes, we applied the same procedure with the conventional TFN except that we used the polymer resistance value $R_{polymer}$ obtained from TFC_{dopa} membrane, instead of TFC membrane. Also, the particle percent occupied area can be determined before the polymerization using characterization techniques. In this study, we analyzed the surface coverage through SEM analysis.

5.3. Results for zeolite water permeance in TFN and TFN-model membranes

In the TFN membranes, the total amount of zeolite (N_p) added into the TMC casting solution was calculated with the known weight of the added particles, average particle size, and density of the zeolite. However, the amount of zeolite incorporated in the TFN membrane structure is related to the number of particles in the reaction zone during the polymerization reaction. The number of particle in the reaction zone (N) is proportional to the thickness of the reaction zone (δ), which depends on the thickness of the boundary diffusion layer (L_B). Therefore, N can be estimated as a function of δ and the total thickness of the casting solution on the membrane (z), which is easily obtained by the ratio of the solution volume to the membrane area ($N \sim N_p\delta/z$).

The thickness of the reaction zone for the polymerization scales with the thickness of the diffusion boundary layer and can be estimated using FS equation [184]. FS equation defines the reaction zone considering the reaction of the MPD/TMC monomers and bimolecular reaction rate [184]. The number of particles in the reaction zone was calculated by using the known volume of the solution, the total number of particles, and

the thickness of the reaction zone. For this calculation, we assumed that the particles are well-dispersed in the casting the solution because of the ultrasonication.

It is important to mention that the weight difference of pore-opened and pore-closed particles changes the actual number of particles in the solutions. We estimated the number of particles for pore-closed zeolites considering the weight of the templating agent in the pores. For instance, for LTA-2 particles, the difference between the number of pore-closed and pore-opened particles in the reaction zone was estimated to be on the order of ~10^8. Therefore, the $R_{interface}$ was calculated by considering the pore-closed particle number, and the $R_{z\ pores}$ was calculated by considering the pore-opened particle number.

The total zeolite area on the membrane can be calculated with the known particle size, cubic structure and the number of particles in the reaction zone. The polymer area is the remaining area from the membrane area excluding the interface area and the zeolite area. Then, the estimated areas were used to calculate the percent occupied area by a particular component, $\nu_{polymer}$, $\nu_{interface}$, and $\nu_{z\ pores}$. On the other hand, we need to estimate the average interface width (*w)* between the particle and the polymer to calculate the interface area.

Since we cannot measure the particle/polymer interface width (*w*) accurately, instead of giving a specific number for the width, we plotted the estimated water permeance of zeolite and the interface for a given constant total membrane permeance over a range of *w,* particle/polymer interface. In Figure 45, the water permeance results of TFN membranes with LTA-2 particles from Chapter 3 is illustrated Figure 45 depicts

that, for conventional TFN membrane incorporated with ~150 nm zeolite particles, if the polymer-particle interface width is smaller than 100 Å, water permeance of the interface is substantially larger than that of zeolite interior cages. On the other hand, the water permeability of the interface and zeolite pores becomes almost equal when the interface width is around 900 Å.

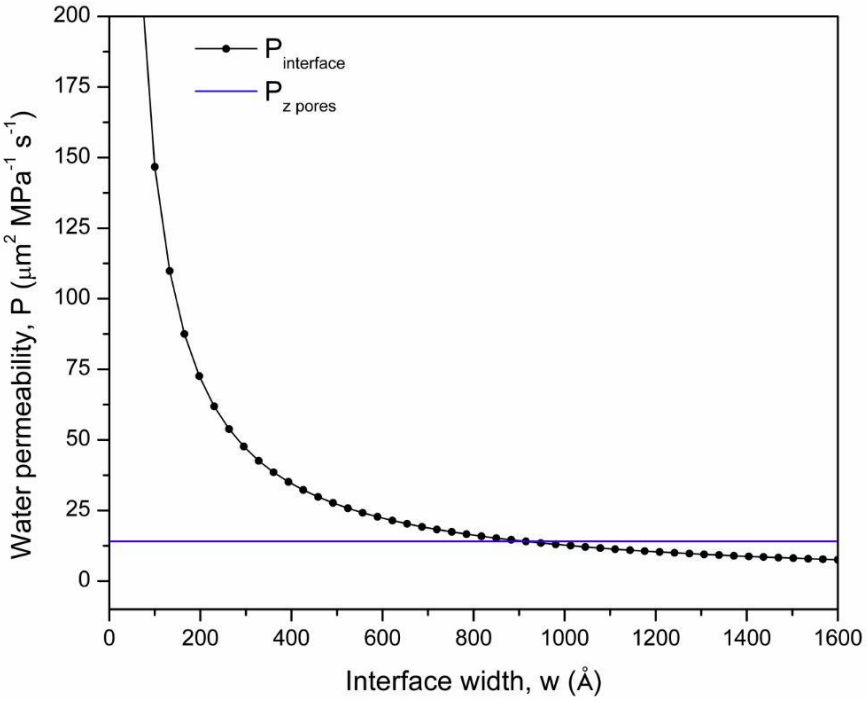

Figure 45: Water permeability of the interface and zeolite pores estimation with respect to the polymer-particle interface width.
TFN membranes incorporated with ~150 nm LTA-2 particles. This plot shows if everything remains same, i.e., the water permeance of the tested membranes TFC, $TFN_{2\text{-}PC}$, and $TFN_{2\text{-}PO}$ and the polymer permeance, the polymer-particle interface width impact on the water permeance of the interface and the water permeability of the zeolite pores.

At this point, to accurately estimate the interface and pore permeabilities, it is important to know the physically reasonable range of the interface width. However, because the thin structure of TFN membranes and relatively lower particle loading (less than 1 wt%) in desalination applications, it is challenging to study the interface

properties. Moore and Koros investigated the particle/polymer interface in mixed matrix gas separation membranes and postulated that there can be five different non-ideal interface morphologies [70]. These are (1) rigidified polymer layer, (2) sieve in a cage, (3) effective void or high free volume phase, (4) clogged zeolite, and (5) reduced permeability region within sieve surface [70]. From these cases, (1) and (5) result in lower water permeability with the addition of the filler. Since in our experiments, we observed a water permeability increase, for all investigated TFN membranes, with particle addition, cases (1) and (5) cannot represent the interface morphology of our membranes. Furthermore, case (4) is also unlikely as our membrane synthesis solutions do not involve solvents smaller than zeolite pore size.

Finally, considering the nanoparticle size and the thickness of the film structure, as shown in Figure 6(b), case (2) cannot be physically possible. Large void formation between the particle and the polymer may result in membrane failure under high pressure for such thin structures. This will also result in a dramatic decrease in salt rejection. Indeed, the salt rejection performance of TFN membranes is similar to that of TFC membranes. Figure 28 shows the water perm-selectivity of TFN membranes with the addition of non-porous and nanoporous particles. Non-porous particle addition into the membrane structure does not impair the water–salt selectivity of the membranes. Therefore, case (3) remains as the only reasonable morphology.

In case (3), the interface is an effective void or high free volume polymer with very small impact on salt selectivity. For effective desalination, the interface width can be considered to be larger than the molecular size of water (2.8 Å) and less than the hydrated diameter of salts (7 Å). Table 5 summarizes the water permeability estimates of the

zeolite pores and the interface when the effective width is 6 Å. This assumption gives unrealistically high water permeability for the interface.

Table 5: Water permeability estimation for the components at w = 6 Å.
Using the resistance model the interface permeability was calculated at w = 6 Å for efficient desalination. However, the interface width does not have any effect on the result of the zeolite water permeability through the interior cage.

Membrane set	Particle	zeolite size nm	$P_{overall}$ $\mu m^2\ MPa^{-1}\ s^{-1}$	$P_{polymer}$ $\mu m^2\ MPa^{-1}\ s^{-1}$	$P_{interface}$ $\mu m^2\ MPa^{-1}\ s^{-1}$	$P_{z\ pores}$ $\mu m^2\ MPa^{-1}\ s^{-1}$
$TFN_{1\text{-}PC/PO}$	LTA-1	~100	1.29 ± 0.01	1.0 ± 0.1	1451 ± 123	7.7 ± 3.3
$TFN_{2\text{-}PC/PO}$	LTA-2	~150	1.74 ± 0.05	1.5 ± 0.1	2532 ± 444	14.0 ± 3.9
$TFN_{3\text{-}PC/PO}$	LTA-3	~200	2.44 ± 0.1	1.9 ± 0.8	3489 ± 556	58.0 ± 45.0
$TFN_{d\text{-}PC/PO}$	LTA-2	~150	1.1 ± 0.05	1.0 ± 0.1	770 ± 325	4.9 ± 2.3

This leaves us with the only option where the interface is a high free volume polymer with an effective width much larger than the molecular size of water. This means that the water permeability and the salt selectivity of the polymer locally change in the vicinity of the particles. As mentioned in Chapter 3.1.2., such a change is possible because the particle presence in the organic casting solution may impact the polymerization reaction. However, the polymer property change should be confined to a very small region around the particles, since the bulk polymer properties are known to be not impacted by particle addition. Indeed, according to Perry's recent study, no significant polymer property changes (i.e., water diffusivity, or microstructure) were observed when NaA and ZIF-8 nanoparticles were incorporated into polyamide TFC membranes [142]. We made conventional NaA TFN membranes that Perry studied in detail for phyico-chemical property and performance relations. Furthermore, the salt rejection is expected to reduce as the interface width increases. Because we did not observe a significant drop in salt rejection of our TFN membranes, we can conclude that the effective interface width is on the order of 100 Å.

Table 6 shows the water permeability estimates of the interface and pores for an effective width of 100 Å. According to Table 6, the interface permeability is significantly higher than the zeolite pores.

Table 6: Water permeability estimation using parallel resistance model for the components of possible transport pathways in TFN membranes when w = 100 Å.

Membrane set	Particle	zeolite size nm	$P_{overall}$ $\mu m^2\ MPa^{-1}\ s^{-1}$	$P_{polymer}$ $\mu m^2\ MPa^{-1}\ s^{-1}$	$P_{interface}$ $\mu m^2\ MPa^{-1}\ s^{-1}$	$P_{z\ pores}$ $\mu m^2\ MPa^{-1}\ s^{-1}$
$TFN_{1\text{-}PC/PO}$	LTA-1	~100	1.29 ± 0.01	1.0 ± 0.1	84 ± 7	7.7 ± 3.9
$TFN_{2\text{-}PC/PO}$	LTA-2	~150	1.74 ± 0.05	1.5 ± 0.1	149 ± 26	14.0 ± 3.9
$TFN_{3\text{-}PC/PO}$	LTA-3	~200	2.44 ± 0.1	1.9 ± 0.8	206 ± 33	58.0 ± 45.0
$TFN_{d\text{-}PC/PO}$	LTA-2	~150	1.1 ± 0.05	1.0 ± 0.1	42 ± 17	4.9 ± 2.3

In conventional TFN membrane synthesis, the hydrophilic LTA particles are dispersed into a hydrophobic (nonpolar) organic solution. Therefore, for these hydrophilic, fine particles, aggregation is thermodynamically favorable to minimize interfacial free energy. Although it is still likely to exist, the degree of particle aggregation may be minimized at low zeolite loading. As nanoparticle aggregation increases in a membrane, the idealized resistance model becomes less applicable. The flow path through the aggregated zeolites across the membrane becomes longer, increasing the resistance of flow. In TFN-model membrane synthesis, the particles were dispersed into an aqueous solution which results in a better particle dispersion in the solution. Moreover, we can easily examine the particle dispersion and aggregation on the support before the IP reaction.

The polymer permeance is less impacted by the presence of the particles because the particles are not introduced into the acid chloride/organic solvent casting solution, in the case that they are the particles may interfere with the functionality of the acid chloride. In the TFN-model membranes the particles are pre-attached to the support

membrane surface before the polyamide interfacial polymerization. Thus, we hypothesize that TFN-model membranes can give more accurate water permeability estimates.

Figure 46 depicts the water permeability of the interface and the zeolite pores for different interface width values for TFN-model membranes. According to this plot, the interface water permeability becomes equal to the zeolite water permeability when the width is larger than 2900 Å. Since this is a physically unrealistic value for the interface width, we can conclude that the water permeability of the interface is higher than that of the pore, regardless of the interface width.

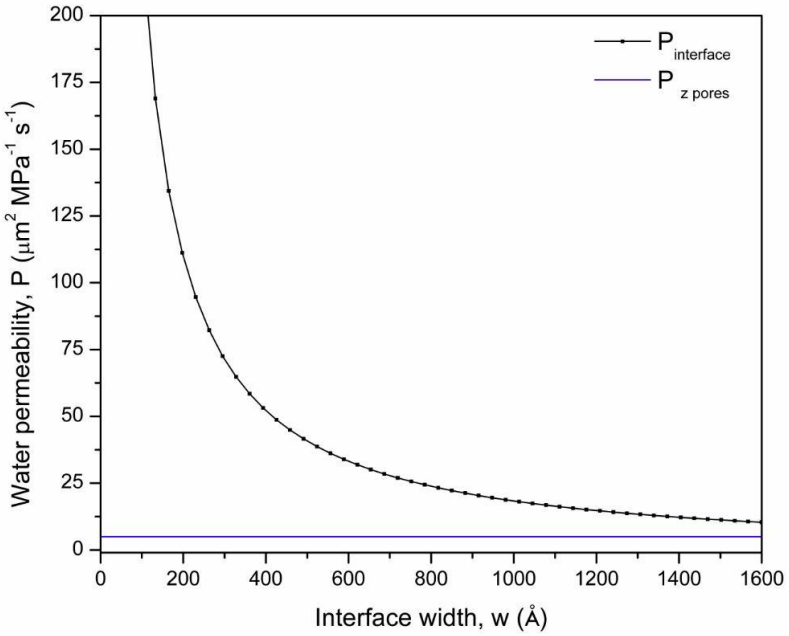

Figure 46: Water permeability of the interface and zeolite pores estimation for TFN-model membrane with respect to the interface width.

Similar results can be obtained with the hybrid resistance model. As opposed to the parallel resistance model, the hybrid resistance model gives us information about how water permeability changes with respect to polymer thickness on and/or under the particle surface. Figure 47 and Figure 48 illustrate water permeability of the interface and the

zeolite pores as a function of interface width and polymer thickness. In these figures, permeability values are plotted in 10log scale, because the dynamic range of the permeability is too large. It is clear that the permeability behavior does not significantly change with polymer thickness on and/or under the particles.

According to the hybrid resistance model, when the polymer thickness on and/or under the particle is larger than 100 Å, either the interface permeability or the zeolite pore permeability becomes negative. This is because of the series resistance added to the model. This provides additional information about the maximum polymer thickness. Another difference between the two resistance models is that there is a lower bound for the interface width in the hybrid resistance model. This lower bound is also determined by the series resistance, and hence, is a function of polymer thickness. The hybrid resistance model converges to the parallel resistance model as the polymer thickness gets closer to the particle size.

At this point, we would like to remind the reader that both resistance models are idealized by several assumptions. For instance, the polyamide membranes have an asymmetric double layer and a highly non-uniform polymer density structure [184]. The polymer has voids in the double layer structure as shown in Figure 49 [185]. Therefore, the thin film does not have a uniform thickness. However, for this analysis, we assumed a uniform polymer density and thickness. In fact, this assumption can be valid for our study since both particle, and the active layer thicknesses are on the order of 100 nm.

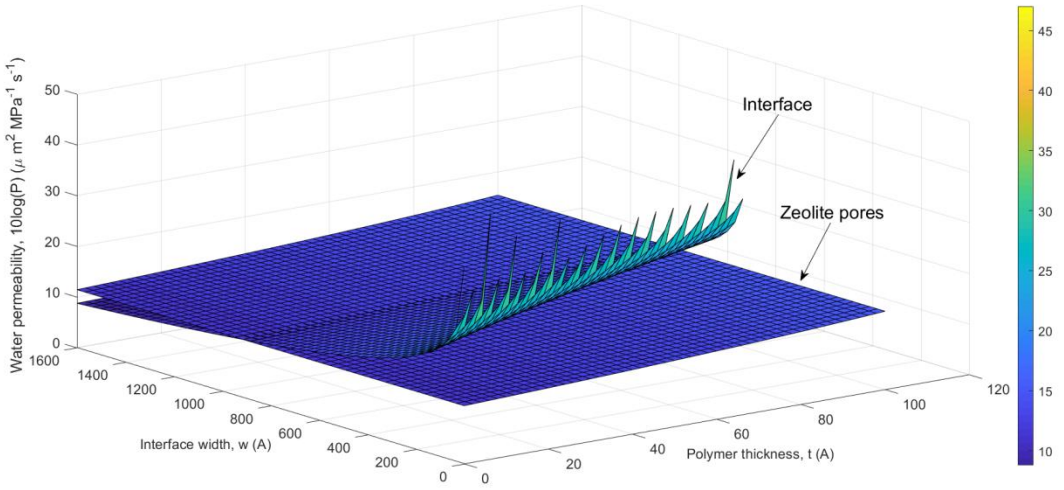

Figure 47: Water permeability of the interface and zeolite pores estimation with respect to the polymer-particle interface width (w) and the polymer thickness on the particles (t) in hybrid resistance model.
The result is for ~150 nm LTA-2 particles in conventional TFN membranes.

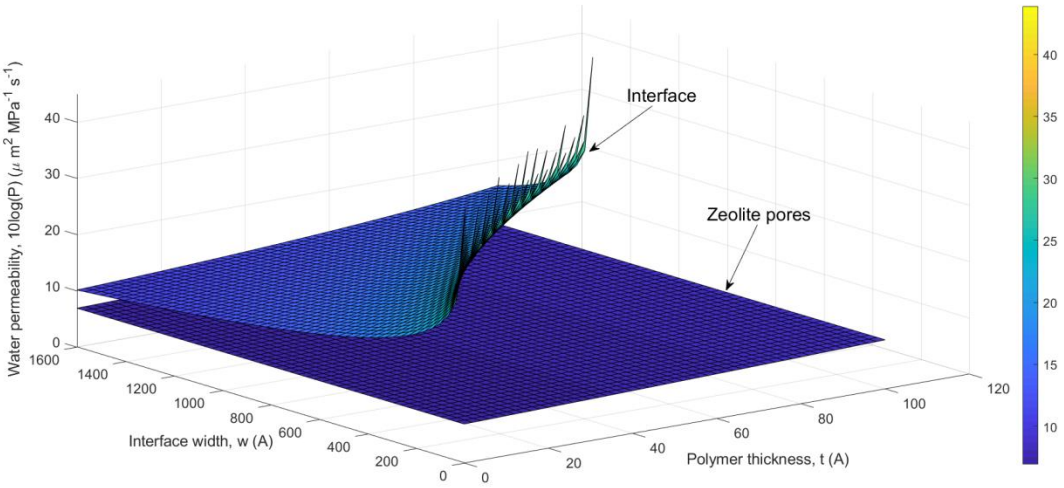

Figure 48: Water permeability of the interface and zeolite pores estimation with respect to the polymer-particle interface width (w) and the polymer thickness on the particles (t) in hybrid resistance model.
The result is for ~150 nm LTA-2 particles in TFN-model membranes.

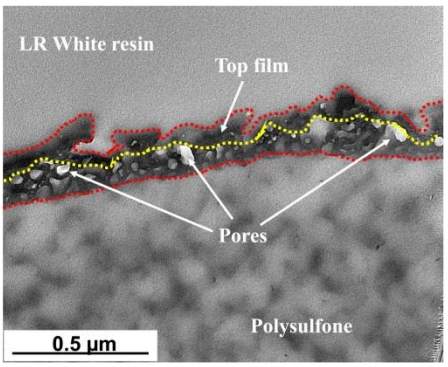

Figure 49: Cross-section TEM image of commercial brackish water RO membrane (ESPA3) as an example for active layer thickness and the void structure.
The polyamide active layer is the region within the red dotted line. The pores are in the active layer are under the yellow dotted line. The image is taken from [185].

For the analysis, we made the following assumptions. (1) The pure polyamide thin film and thin film nanocomposite membranes (TFN and TFN-model) are continuous and defect-free. Under this assumption, the only pathways for transport through the membranes are through the polymer, the polymer matrix-particle interface, and the zeolite particle. The salt rejection performances of the membranes support this assumption. (2) For the parallel resistance model, the inverse of the total resistance ($R_{membrane}$) is equal to the sum of inverses of the resistance through each phase as described previously in Equation 5.2. Each of the three phases has an intrinsic permeability and a corresponding resistance. (3) The permeability of the matrix-particle interface is independent of the state of the zeolite pores (i.e., whether the zeolite pores are opened or closed). The pores of the pore-filled zeolites retain the templating agent, around which the zeolites nucleate and grow, which can change the surface property as well as particle-polymer interface property. (4) Incorporation of zeolites does not change the permeability of the bulk polymer. (5) The zeolite nanoparticles are single crystals and uniformly distributed in the structure. The analysis does not account for the aggregated

particles. (6) The analysis does not account for the mechanical changes in the membranes with the addition of the particles under hydraulic pressure. The addition of nanoparticles can change the mechanical compaction and water permeance of the membranes [36]. However, in this study, nanoparticle content in the structure was very low, so we considered a minimal mechanical change with the addition of particles.

5.4. Conclusion

The resistance model analysis of the conventional TFN and TFN-model membranes, to investigate the individual component contributions to water transport, shows that the water permeability of zeolites through the interior cage is within 2.6—103 $\mu m^2\ MPa^{-1}\ s^{-1}$. The estimated interface permeability is at least four times higher than that of the zeolite pores and the polymer even for the TFN-model membrane. This indicates that the preferential water pathway is through the particle-polymer interface. The results also show that the interface permeability, as expected, strongly depends on the interface width. However, since we cannot readily measure the interface width and validate the assumptions regarding the polymer structure, more work is still required to probe the permeability of TFN components accurately. This includes the investigation of the local polymer permeability change with particle addition, pore-state of the particles, and a detailed characterization of the particle-polymer interface with advanced techniques.

6. SUMMARY AND RECOMMENDATIONS

In this dissertation, we investigated the water transport mechanisms through zeolite A molecular sieve particles in thin film nanocomposite membranes. Our meta-analysis of nanoporous material (zeolites, MOFs, and graphene-based materials) addition in polyamide-based osmotic TFN membranes showed no uniform performance change as a result of particle addition. Although TFN membranes exhibit great promise for permeance enhancement and the addition of new features such as chlorine and fouling resistance, a consistency between performance improvement of polyamide-based osmotic membranes, and type, size, and pore size of embedded nanoporous materials (zeolites, MOFs, and graphene-based materials) was not observed. This results from the inherent complexity of the polyamide interfacial polymerization reaction, which is compounded by the various researchers' slight changes in interfacial polymerization steps, and the actual presence of nanoporous materials during the reaction. Thus, we conducted an experimental study on TFN membranes to provide an understanding of the impact of nanoporous particles to water transport. Further, this is the first report to directly experimentally probe whether water transport occurs through single crystal zeolites in a pressure-driven osmotic process.

First, we synthesized and studied non-porous (pore-closed) and nanoporous (pore-opened) zeolite particles at three different crystal sizes as fillers in TFN membranes. The results show that membranes with smaller particles exhibited higher water permeance and lower water-salt permselectivity than the membranes with larger particles and TFC membranes. The most significant impact of the pore-state of the particles on the water

permeance was observed on the membranes with the largest particles. Moreover, membranes with pore-opened particles showed higher water permeance compared to the corresponding membrane with pore-closed particles. However, the membrane surface properties (i.e., roughness and hydrophilicity) differed from that of the membrane without the particles, and the incorporated amount of particles in the structure was unknown.

For further analysis, we developed two different model membrane designs which can provide a better understanding of the role of nanoporous materials in water transport. First, we studied the non-porous and nanoporous particles in the TFN-model membrane design. Water permeance of the membrane with nanoporous particles was slightly, but insignificantly, higher than that of the membrane with non-porous particles. The membranes' contact angles, roughnesses, and functionalities were similar regardless of the nanoparticles' pore-state. The polyamide permeability can be similar for the TFN-model membranes and the TFC_{dopa} membranes. However, introducing the polydopamine adhesion layer increases the complexity of the reaction and heterogeneity of the structure. As a second design, a water impermeable polymer model membrane design, based on latex film formation, was developed but not tested for this study because our synthesized particle size range was smaller than the minimum thickness of defect-free membrane synthesis with this method.

To estimate the water permeability of molecular sieve particles in TFN membranes, we applied two resistance models to the conventional TFN and TFN-model membranes. We observed that water permeance of the particle-zeolite interface is substantially higher than that of the zeolite pores for small interface width (<10 nm). We concluded that the zeolite pores and the particle/polymer interface provide additional

water transport pathways in thin film nanocomposite membranes, but the preferential pathway for the water flow is the particle-polymer interface. Our analysis was based on the assumption that the polyamide permeability does not change with the addition of the particles and with the state of the particles. Although TFN-model membranes introduce particles in such a way to minimize possible interference with the interfacial polymerization reaction, there may be additional structure changes because of mechanical stress under high pressure. For instance, Pendergast et al. showed that nanoparticle presence in the membrane structure could lower the membrane compaction during hydraulic testing which alters the membrane permeability because of the change in the mechanical structure of the membrane [36]. Yet, our analysis does not include any study of the mechanical compaction with the particle presence. The water impermeable model membrane could have addressed the mechanical structure change with the addition of particles in the water impermeable polymer in the matrix.

The TFN-model membrane study was a proof of concept experiment. This study conducted at low particle coverage and ~150 nm size particles. Future work could expand this study to include more particle coverage, particle sizes, and various nanoporous/ mesoporous particle incorporation. Although the adhesion layer polymerization increases the complexity of the membrane synthesis and characterization, it enables more systematic analysis through controlled particle incorporation. Further, the water impermeable polymer model membrane can be studied using bigger sized particles (~300-500 nm) for water permeability analysis.

REFERENCES

[1] M. Mulder, Basic Principles of Membrane Technology, 2nd Ed. ed., Kluwer, Dordrecht, Neth., 1996.

[2] A. Lee, J.W. Elam, S.B. Darling, Membrane materials for water purification: design, development, and application, Environmental Science: Water Research & Technology, 2 (2016) 17-42.

[3] B. Van der Bruggen, C. Vandecasteele, T. Van Gestel, W. Doyen, R. Leysen, A review of pressure-driven membrane processes in wastewater treatment and drinking water production, Environmental progress, 22 (2003) 46-56.

[4] D. Li, H.T. Wang, Recent developments in reverse osmosis desalination membranes, J Mater Chem, 20 (2010) 4551-4566.

[5] N. Ghaffour, T.M. Missimer, G.L. Amy, Technical review and evaluation of the economics of water desalination: current and future challenges for better water supply sustainability, Desalination, 309 (2013) 197-207.

[6] M.W. Shahzad, M. Burhan, L. Ang, K.C. Ng, Energy-water-environment nexus underpinning future desalination sustainability, Desalination, 413 (2017) 52-64.

[7] A. Subramani, J.G. Jacangelo, Emerging desalination technologies for water treatment: a critical review, Water Res, 75 (2015) 164-187.

[8] T.Y. Cath, A.E. Childress, M. Elimelech, Forward osmosis: principles, applications, and recent developments, Journal of membrane science, 281 (2006) 70-87.

[9] Q. Wang, N. Li, B. Bolto, M. Hoang, Z. Xie, Desalination by pervaporation: a review, Desalination, 387 (2016) 46-60.

[10] A. Alkhudhiri, N. Darwish, N. Hilal, Membrane distillation: a comprehensive review, Desalination, 287 (2012) 2-18.

[11] A. Deshmukh, C. Boo, V. Karanikola, S. Lin, A.P. Straub, T. Tong, D.M. Warsinger, M. Elimelech, Membrane distillation at the water-energy nexus: limits, opportunities, and challenges, Energ Environ Sci, 11 (2018) 1177-1196.

[12] M. Sadrzadeh, T. Mohammadi, Sea water desalination using electrodialysis, Desalination, 221 (2008) 440-447.

[13] D.L. Shaffer, J.R. Werber, H. Jaramillo, S. Lin, M. Elimelech, Forward osmosis: where are we now?, Desalination, 356 (2015) 271-284.

[14] J.-P. Mericq, S. Laborie, C. Cabassud, Vacuum membrane distillation of seawater reverse osmosis brines, Water Res, 44 (2010) 5260-5273.

[15] S. Al-Obaidani, E. Curcio, F. Macedonio, G. Di Profio, H. Al-Hinai, E. Drioli, Potential of membrane distillation in seawater desalination: thermal efficiency, sensitivity study and cost estimation, Journal of Membrane Science, 323 (2008) 85-98.

[16] S. Thampy, G.R. Desale, V.K. Shahi, B.S. Makwana, P.K. Ghosh, Development of hybrid electrodialysis-reverse osmosis domestic desalination unit for high recovery of product water, Desalination, 282 (2011) 104-108.

[17] R.K. McGovern, On the potential of forward osmosis to energetically outperform reverse osmosis desalination, Journal of Membrane Science, 469 (2014) 245-250.

[18] S.S. Shenvi, A.M. Isloor, A. Ismail, A review on RO membrane technology: developments and challenges, Desalination, 368 (2015) 10-26.

[19] L. Malaeb, G.M. Ayoub, Reverse osmosis technology for water treatment: state of the art review, Desalination, 267 (2011) 1-8.

[20] G.M. Geise, D.R. Paul, B.D. Freeman, Fundamental water and salt transport properties of polymeric materials, Progress in Polymer Science, 39 (2014) 1-42.

[21] J. Wang, D.S. Dlamini, A.K. Mishra, M.T.M. Pendergast, M.C. Wong, B.B. Mamba, V. Freger, A.R. Verliefde, E.M. Hoek, A critical review of transport through osmotic membranes, Journal of Membrane Science, 454 (2014) 516-537.

[22] G.M.P. Geise, H. B.; Sagle, A. C.; Freeman, B. D.; McGrath, J. E., Water permeability and water/salt selectivity tradeoff in polymers for desalination, Journal of Membrane Science, 369 (2011) 130-138.

[23] L. Wang, M.S. Boutilier, P.R. Kidambi, D. Jang, N.G. Hadjiconstantinou, R. Karnik, Fundamental transport mechanisms, fabrication and potential applications of nanoporous atomically thin membranes, Nature nanotechnology, 12 (2017) 509-522.

[24] P.L.T. Brian, Concentration Polar zation in Reverse Osmosis Desalination with Variable Flux and Incomplete Salt Rejection, Industrial & Engineering Chemistry Fundamentals, 4 (1965) 439-445.

[25] L. Song, S. Yu, Concentration polarization in cross-flow reverse osmosis, American Institute of Chemical Engineers. AIChE Journal, 45 (1999) 921.

[26] S. Kim, E.M. Hoek, Modeling concentration polarization in reverse osmosis processes, Desalination, 186 (2005) 111-128.

[27] L.M. Robeson, Correlation of Separation Factor Versus Permeability for Polymeric Membranes, J Membrane Sci, 62 (1991) 165-185.

[28] L.M. Robeson, The upper bound revisited, Journal of Membrane Science, 320 (2008) 390-400.

[29] H. Zhang, G.M. Geise, Modeling the water permeability and water/salt selectivity tradeoff in polymer membranes, Journal of Membrane Science, 520 (2016) 790-800.

[30] W. Chen, S. Chen, T. Liang, Q. Zhang, Z. Fan, H. Yin, K.-W. Huang, X. Zhang, Z. Lai, P. Sheng, High-flux water desalination with interfacial salt sieving effect in nanoporous carbon composite membranes, Nature nanotechnology, 13 (2018) 345.

[31] Y.-x. Shen, W.C. Song, D.R. Barden, T. Ren, C. Lang, H. Feroz, C.B. Henderson, P.O. Saboe, D. Tsai, H. Yan, Achieving high permeability and enhanced selectivity for Angstrom-scale separations using artificial water channel membranes, Nature communications, 9 (2018).

[32] J.R. Werber, C.O. Osuji, M. Elimelech, Materials for next-generation desalination and water purification membranes, Nature Reviews Materials, 1 (2016) 16018.

[33] B. Tansel, J. Sager, T. Rector, J. Garland, R.F. Strayer, L. Levine, M. Roberts, M. Hummerick, J. Bauer, Significance of hydrated radius and hydration shells on ionic permeability during nanofiltration in dead end and cross flow modes, Separation and Purification Technology, 51 (2006) 40-47.

[34] S.H. Jamali, T.J. Vlugt, L.-C. Lin, Atomistic Understanding of Zeolite Nanosheets for Water Desalination, The Journal of Physical Chemistry C, (2017).

[35] Y. Liu, X. Chen, High permeability and salt rejection reverse osmosis by a zeolite nano-membrane, Physical Chemistry Chemical Physics, 15 (2013) 6817-6824.

[36] M.T.M. Pendergast, J.M. Nygaard, A.K. Ghosh, E.M. Hoek, Using nanocomposite materials technology to understand and control reverse osmosis membrane compaction, Desalination, 261 (2010) 255-263.

[37] M. Fasano, T. Humplik, A. Bevilacqua, M. Tsapatsis, E. Chiavazzo, E.N. Wang, P. Asinari, Interplay between hydrophilicity and surface barriers on water transport in zeolite membranes, Nature communications, 7 (2016) 12762.

[38] B.J. Feinberg, E. Hoek, Interfacial Polymerization, Encyclopedia of Membrane Science and Technology, (2013).

[39] A. Soroush, J. Barzin, M. Barikani, M. Fathizadeh, Interfacially polymerized polyamide thin film composite membranes: Preparation, characterization and performance evaluation, Desalination, 287 (2012) 310-316.

[40] A.K. Ghosh, B.-H. Jeong, X. Huang, E. Hoek, Impacts of reaction and curing conditions on polyamide composite reverse osmosis membrane properties, J Membrane Sci, 311 (2008) 34-45.

[41] A.K. Ghosh, E.M.V. Hoek, Impacts of support membrane structure and chemistry on polyamide-polysulfone interfacial composite membranes, Journal of Membrane Science, 336 (2009) 140-148.

[42] D.M. Stevens, J.Y. Shu, M. Reichert, A. Roy, Next-Generation Nanoporous Materials: Progress and Prospects for Reverse Osmosis and Nanofiltration, Industrial & Engineering Chemistry Research, (2017).

[43] H.B. Park, B.D. Freeman, Z.B. Zhang, M. Sankir, J.E. McGrath, Highly Chlorine-Tolerant Polymers for Desalination, Angewandte Chemie, 120 (2008) 6108-6113.

[44] P. Goh, W. Lau, M. Othman, A. Ismail, Membrane fouling in desalination and its mitigation strategies, Desalination, 425 (2018) 130-155.

[45] M. Goosen, S. Sablani, H. Al-Hinai, S. Al-Obeidani, R. Al-Belushi, D. Jackson, Fouling of reverse osmosis and ultrafiltration membranes: a critical review, Separation Science and Technology, 39 (2005) 2261-2297.

[46] E.M. Hoek, A.S. Kim, M. Elimelech, Influence of crossflow membrane filter geometry and shear rate on colloidal fouling in reverse osmosis and nanofiltration separations, Environmental Engineering Science, 19 (2002) 357-372.

[47] S. Jiang, Y. Li, B.P. Ladewig, A review of reverse osmosis membrane fouling and control strategies, Science of The Total Environment, 595 (2017) 567-583.

[48] R. Verbeke, V. Gómez, I.F. Vankelecom, Chlorine-resistance of reverse osmosis (RO) polyamide membranes, Progress in Polymer Science, 72 (2017) 1-15.

[49] J.M. Gohil, A.K. Suresh, Chlorine attack on reverse osmosis membranes: Mechanisms and mitigation strategies, Journal of Membrane Science, 541 (2017) 108-126.

[50] B. Khorshidi, T. Thundat, B.A. Fleck, M. Sadrzadeh, A novel approach toward fabrication of high performance thin film composite polyamide membranes, Scientific reports, 6 (2016) 22069.

[51] C.M. Zimmerman, A. Singh, W.J. Koros, Tailoring mixed matrix composite membranes for gas separations, J Membrane Sci, 137 (1997) 145-154.

[52] S. Al Aani, C.J. Wright, M.A. Atieh, N. Hilal, Engineering nanocomposite membranes: Addressing current challenges and future opportunities, Desalination, 401 (2017) 1-15.

[53] J. Wu, K.R. Zodrow, P.B. Szemraj, Q. Li, Photothermal nanocomposite membranes for direct solar membrane distillation, J Mater Chem A, 5 (2017) 23712-23719.

[54] B.H. Jeong, E.M.V. Hoek, Y.S. Yan, A. Subramani, X.F. Huang, G. Hurwitz, A.K. Ghosh, A. Jawor, Interfacial polymerization of thin film nanocomposites: A new concept for reverse osmosis membranes, J Membrane Sci, 294 (2007) 1-7.

[55] M.L. Lind, A.K. Ghosh, A. Jawor, X.F. Huang, W. Hou, Y. Yang, E.M.V. Hoek, Influence of Zeolite Crystal Size on Zeolite-Polyamide Thin Film Nanocomposite Membranes, Langmuir, 25 (2009) 10139-10145.

[56] M. Fathizadeh, A. Aroujalian, A. Raisi, Effect of added NaX nano-zeolite into polyamide as a top thin layer of membrane on water flux and salt rejection in a reverse osmosis process, J Membrane Sci, 375 (2011) 88-95.

[57] H. Dong, X.Y. Qu, L. Zhang, L.H. Cheng, H.L. Chen, C.J. Gao, Preparation and characterization of surface-modified zeolite-polyamide thin film nanocomposite membranes for desalination, Desalin Water Treat, 34 (2011) 6-12.

[58] M.L. Lind, D.E. Suk, T.V. Nguyen, E.M.V. Hoek, Tailoring the Structure of Thin Film Nanocomposite Membranes to Achieve Seawater RD Membrane Performance, Environmental Science & Technology, 44 (2010) 8230-8235.

[59] N. Ma, J. Wei, R.H. Liao, C.Y.Y. Tang, Zeolite-polyamide thin film nanocomposite membranes: Towards enhanced performance for forward osmosis, Journal of Membrane Science, 405 (2012) 149-157.

[60] H. Huang, X. Qu, X. Ji, X. Gao, L. Zhang, H. Chen, L. Hou, Acid and multivalent ion resistance of thin film nanocomposite RO membranes loaded with silicalite-1 nanozeolites, J Mater Chem A, 1 (2013) 11343-11349.

[61] H. Huang, X. Qu, H. Dong, L. Zhang, H. Chen, Role of NaA zeolites in the interfacial polymerization process towards a polyamide nanocomposite reverse osmosis membrane, RSC Advances, 3 (2013) 8203-8207.

[62] E.-S. Kim, G. Hwang, M.G. El-Din, Y. Liu, Development of nanosilver and multi-walled carbon nanotubes thin-film nanocomposite membrane for enhanced water treatment, J Membrane Sci, 394 (2012) 37-48.

[63] J. Park, W. Choi, S.H. Kim, B.H. Chun, J. Bang, K.B. Lee, Enhancement of chlorine resistance in carbon nanotube based nanocomposite reverse osmosis membranes, Desalin Water Treat, 15 (2010) 198-204.

[64] S. Roy, S.A. Ntim, S. Mitra, K.K. Sirkar, Facile fabrication of superior nanofiltration membranes from interfacially polymerized CNT-polymer composites, J Membrane Sci, 375 (2011) 81-87.

[65] W.-F. Chan, H.-y. Chen, A. Surapathi, M.G. Taylor, X. Shao, E. Marand, J.K. Johnson, Zwitterion functionalized carbon nanotube/polyamide nanocomposite membranes for water desalination, ACS nano, 7 (2013) 5308-5319.

[66] J. Yin, E.-S. Kim, J. Yang, B. Deng, Fabrication of a novel thin-film nanocomposite (TFN) membrane containing MCM-41 silica nanoparticles (NPs) for water purification, J Membrane Sci, 423 (2012) 238-246.

[67] G.L. Jadav, P.S. Singh, Synthesis of novel silica-polyamide nanocomposite membrane with enhanced properties, J Membrane Sci, 328 (2009) 257-267.

[68] M. Bao, G. Zhu, L. Wang, M. Wang, C. Gao, Preparation of monodispersed spherical mesoporous nanosilica–polyamide thin film composite reverse osmosis membranes via interfacial polymerization, Desalination, 309 (2013) 261-266.

[69] C. Kong, T. Kamada, T. Shintani, M. Kanezashi, T. Yoshioka, T. Tsuru, Enhanced performance of inorganic-polyamide nanocomposite membranes prepared by metal-alkoxide-assisted interfacial polymerization, J Membrane Sci, 366 (2011) 382-388.

[70] T.T. Moore, W.J. Koros, Non-ideal effects in organic–inorganic materials for gas separation membranes, Journal of Molecular Structure, 739 (2005) 87-98.

[71] D.Q. Vu, W.J. Koros, S.J. Miller, Mixed matrix membranes using carbon molecular sieves: I. Preparation and experimental results, J Membrane Sci, 211 (2003) 311-334.

[72] D. Breck, W. Eversole, R. Milton, T. Reed, T. Thomas, Crystalline zeolites. I. The properties of a new synthetic zeolite, type A, Journal of the American chemical society, 78 (1956) 5963-5972.

[73] B. Van der Bruggen, J. Schaep, D. Wilms, C. Vandecasteele, Influence of molecular size, polarity and charge on the retention of organic molecules by nanofiltration, J Membrane Sci, 156 (1999) 29-41.

[74] P. Cay-Durgun, C. McCloskey, J. Konecny, A. Khosravi, M.L. Lind, Evaluation of thin film nanocomposite reverse osmosis membranes for long-term brackish water desalination performance, Desalination, 404 (2017) 304-312.

[75] S. Turgman-Cohen, J.C. Araque, E.M. Hoek, F.A. Escobedo, Molecular dynamics of equilibrium and pressure-driven transport properties of water through LTA-type zeolites, Langmuir, 29 (2013) 12389-12399.

[76] P. Cay-Durgun, S.G. Fink, A. Shabilla, H. Yin, K.A. Sasaki, M.L. Lind, Analysis of the Water Permeability of Linde Type A Zeolites in Reverse Osmosis, Separation Science and Technology, 49 (2014) 2824-2833.

[77] J. Cui, X. Zhang, H. Liu, S. Liu, K.L. Yeung, Preparation and application of zeolite/ceramic microfiltration membranes for treatment of oil contaminated water, Journal of Membrane Science, 325 (2008) 420-426.

[78] W. Lau, S. Gray, T. Matsuura, D. Emadzadeh, J.P. Chen, A. Ismail, A review on polyamide thin film nanocomposite (TFN) membranes: History, applications, challenges and approaches, Water Research, 80 (2015) 306-324.

[79] J.R. Werber, A. Deshmukh, M. Elimelech, The critical need for increased selectivity, not increased water permeability, for desalination membranes, Environmental Science & Technology Letters, 3 (2016) 112-120.

[80] N. Fridman-Bishop, V. Freger, What Makes Aromatic Polyamide Membranes Superior: New Insights into Ion Transport and Membrane Structure, Journal of Membrane Science, (2017).

[81] M. Shen, S. Keten, R.M. Lueptow, Dynamics of water and solute transport in polymeric reverse osmosis membranes via molecular dynamics simulations, Journal of Membrane Science, 506 (2016) 95-108.

[82] L. Lin, R. Lopez, G.Z. Ramon, O. Coronell, Investigating the void structure of the polyamide active layers of thin-film composite membranes, Journal of Membrane Science, 497 (2016) 365-376.

[83] P.D. Dongare, A. Alabastri, S. Pedersen, K.R. Zodrow, N.J. Hogan, O. Neumann, J. Wu, T. Wang, A. Deshmukh, M. Elimelech, Nanophotonics-enabled solar membrane distillation for off-grid water purification, Proceedings of the National Academy of Sciences, 114 (2017) 6936-6941.

[84] K. Dutta, S. De, Smart responsive materials for water purification: an overview, J Mater Chem A, 5 (2017) 22095-22112.

[85] D. Cohen-Tanugi, R.K. McGovern, S.H. Dave, J.H. Lienhard, J.C. Grossman, Quantifying the potential of ultra-permeable membranes for water desalination, Energ Environ Sci, 7 (2014) 1134-1141.

[86] D. Li, Y. Yan, H. Wang, Recent advances in polymer and polymer composite membranes for reverse and forward osmosis processes, Progress in Polymer Science, 61 (2016) 104-155.

[87] M.J. Raaijmakers, N.E. Benes, Current trends in interfacial polymerization chemistry, Progress in Polymer Science, 63 (2016) 86-142.

[88] X.-H. Ma, Z.-K. Yao, Z. Yang, H. Guo, Z.-L. Xu, C.Y. Tang, M. Elimelech, Nanofoaming of Polyamide Desalination Membranes To Tune Permeability and Selectivity, Environmental Science & Technology Letters, 5 (2018) 123-130.

[89] B. Ukrainsky, G.Z. Ramon, Temperature measurement of the reaction zone during polyamide film formation by interfacial polymerization, Journal of Membrane Science, 566 (2018) 329-335.

[90] M.C. Wong, L. Lin, O. Coronell, E.M. Hoek, G.Z. Ramon, Impact of liquid-filled voids within the active layer on transport through thin-film composite membranes, Journal of Membrane Science, 500 (2016) 124-135.

[91] B. Khorshidi, T. Thundat, B. Fleck, M. Sadrzadeh, Thin film composite polyamide membranes: parametric study on the influence of synthesis conditions, RSC Advances, 5 (2015) 54985-54997.

[92] V. Vatanpour, M. Sheydaei, M. Esmaeili, Box-Behnken design as a systematic approach to inspect correlation between synthesis conditions and desalination performance of TFC RO membranes, Desalination, 420 (2017) 1-11.

[93] M.L. Lind, B.H. Jeong, A. Subramani, X.F. Huang, E.M.V. Hoek, Effect of mobile cation on zeolite-polyamide thin film nanocomposite membranes, J Mater Res, 24 (2009) 1624-1631.

[94] H. Dong, L. Zhao, L. Zhang, H. Chen, C. Gao, W.W. Ho, High-flux reverse osmosis membranes incorporated with NaY zeolite nanoparticles for brackish water desalination, Journal of Membrane Science, 476 (2015) 373-383.

[95] B.S. Lalia, V. Kochkodan, R. Hashaikeh, N. Hilal, A review on membrane fabrication: Structure, properties and performance relationship, Desalination, 326 (2013) 77-95.

[96] M.L. Lind, D. Eumine Suk, T.-V. Nguyen, E.M.V. Hoek, Tailoring the Structure of Thin Film Nanocomposite Membranes to Achieve Seawater RO Membrane Performance, Environ Sci Technol, 44 (2010) 8230-8235.

[97] L.-x. Dong, X.-c. Huang, Z. Wang, Z. Yang, X.-m. Wang, C.Y. Tang, A thin-film nanocomposite nanofiltration membrane prepared on a support with in situ embedded zeolite nanoparticles, Sep Purif Technol, 166 (2016) 230-239.

[98] M. Safarpour, V. Vatanpour, A. Khataee, H. Zarrabi, P. Gholami, M.E. Yekavalangi, High flux and fouling resistant reverse osmosis membrane modified with plasma treated natural zeolite, Desalination, 411 (2017) 89-100.

[99] J. Zhu, L. Qin, A. Uliana, J. Hou, J. Wang, Y. Zhang, X. Li, S. Yuan, J. Li, M. Tian, Elevated Performance of Thin Film Nanocomposite Membranes Enabled by Modified Hydrophilic MOFs for Nanofiltration, Acs Appl Mater Inter, 9 (2017) 1975-1986.

[100] Y. Xu, X. Gao, X. Wang, Q. Wang, Z. Ji, X. Wang, T. Wu, C. Gao, Highly and stably water permeable thin film nanocomposite membranes doped with MIL-101 (Cr) nanoparticles for reverse osmosis application, Materials, 9 (2016) 870.

[101] C. Van Goethem, R. Verbeke, S. Hermans, R. Bernstein, I. Vankelecom, Controlled positioning of MOFs in interfacially polymerized thin-film nanocomposites, Journal of Materials Chemistry A, 4 (2016) 16368-16376.

[102] J. Duan, Y. Pan, F. Pacheco, E. Litwiller, Z. Lai, I. Pinnau, High-performance polyamide thin-film-nanocomposite reverse osmosis membranes containing hydrophobic zeolitic imidazolate framework-8, Journal of Membrane Science, 476 (2015) 303-310.

[103] I.H. Aljundi, Desalination characteristics of TFN-RO membrane incorporated with ZIF-8 nanoparticles, Desalination, 420 (2017) 12-20.

[104] H.-R. Chae, J. Lee, C.-H. Lee, I.-C. Kim, P.-K. Park, Graphene oxide-embedded thin-film composite reverse osmosis membrane with high flux, anti-biofouling, and chlorine resistance, Journal of Membrane Science, 483 (2015) 128-135.

[105] M.E. Ali, L. Wang, X. Wang, X. Feng, Thin film composite membranes embedded with graphene oxide for water desalination, Desalination, 386 (2016) 67-76.

[106] S. Bano, A. Mahmood, S.-J. Kim, K.-H. Lee, Graphene oxide modified polyamide nanofiltration membrane with improved flux and antifouling properties, J Mater Chem A, 3 (2015) 2065-2071.

[107] H. Li, W. Shi, Q. Du, R. Zhou, H. Zhang, X. Qin, Improved separation and antifouling properties of thin-film composite nanofiltration membrane by the incorporation of cGO, Applied Surface Science, 407 (2017) 260-275.

[108] M. Safarpour, A. Khataee, V. Vatanpour, Thin film nanocomposite reverse osmosis membrane modified by reduced graphene oxide/TiO 2 with improved desalination performance, Journal of Membrane Science, 489 (2015) 43-54.

[109] H.M. Hegab, A. ElMekawy, T.G. Barclay, A. Michelmore, L. Zou, D. Losic, C.P. Saint, M. Ginic-Markovic, A Novel Fabrication Approach for Multifunctional Graphene-based Thin Film Nano-composite Membranes with Enhanced Desalination and Antibacterial Characteristics, Scientific reports, 7 (2017).

[110] P. Wen, Y. Chen, X. Hu, B. Cheng, D. Liu, Y. Zhang, S. Nair, Polyamide thin film composite nanofiltration membrane modified with acyl chlorided graphene oxide, Journal of Membrane Science, 535 (2017) 208-220.

[111] P. Cay-Durgun, M.L. Lind, Nanoporous materials in polymeric membranes for desalination, Current opinion in chemical engineering, 20 (2018) 19-27.

[112] H.-C. Yang, J. Hou, V. Chen, Z.-K. Xu, Surface and interface engineering for organic–inorganic composite membranes, J Mater Chem A, 4 (2016) 9716-9729.

[113] H.L. Jamieson, H. Yin, A. Waller, A. Khosravi, M.L. Lind, Impact of acids on the structure and composition of Linde Type A zeolites for use in reverse osmosis membranes for recovery of urine-containing wastewaters, Microporous and Mesoporous Materials, 201 (2015) 50-60.

[114] L.-x. Dong, H.-w. Yang, S.-t. Liu, X.-m. Wang, Y.F. Xie, Fabrication and anti-biofouling properties of alumina and zeolite nanoparticle embedded ultrafiltration membranes, Desalination, 365 (2015) 70-78.

[115] S. Wang, Y. Peng, Natural zeolites as effective adsorbents in water and wastewater treatment, Chemical Engineering Journal, 156 (2010) 11-24.

[116] A. Ates, C. Hardacre, The effect of various treatment conditions on natural zeolites: Ion exchange, acidic, thermal and steam treatments, J Colloid Interf Sci, 372 (2012) 130-140.

[117] M.S. Denny Jr, J.C. Moreton, L. Benz, S.M. Cohen, Metal–organic frameworks for membrane-based separations, 1 (2016) 16078.

[118] C. Wang, X. Liu, N.K. Demir, J.P. Chen, K. Li, Applications of water stable metal–organic frameworks, Chemical Society Reviews, 45 (2016) 5107-5134.

[119] K. Zhang, R.P. Lively, C. Zhang, R.R. Chance, W.J. Koros, D.S. Sholl, S. Nair, Exploring the framework hydrophobicity and flexibility of ZIF-8: from biofuel recovery to hydrocarbon separations, The Journal of Physical Chemistry Letters, 4 (2013) 3618-3622.

[120] M.C. Duke, B. Zhu, C.M. Doherty, M.R. Hill, A.J. Hill, M.A. Carreon, Structural effects on SAPO-34 and ZIF-8 materials exposed to seawater solutions, and their potential as desalination membranes, Desalination, 377 (2016) 128-137.

[121] Y. Xu, X. Gao, Q. Wang, X. Wang, Z. Ji, C. Gao, Highly stable MIL-101 (Cr) doped water permeable thin film nanocomposite membranes for water treatment, RSC Advances, 6 (2016) 82669-82675.

[122] H. Ang, L. Hong, Polycationic Polymer-Regulated Assembling of 2D MOF Nanosheets for High-Performance Nanofiltration, Acs Appl Mater Inter, 9 (2017) 28079-28088.

[123] S.P. Surwade, S.N. Smirnov, I.V. Vlassiouk, R.R. Unocic, G.M. Veith, S. Dai, S.M. Mahurin, Water desalination using nanoporous single-layer graphene, Nature nanotechnology, 10 (2015) 459-464.

[124] S.C. O'Hern, D. Jang, S. Bose, J.-C. Idrobo, Y. Song, T. Laoui, J. Kong, R. Karnik, Nanofiltration across defect-sealed nanoporous monolayer graphene, Nano letters, 15 (2015) 3254-3260.

[125] J. Abraham, K.S. Vasu, C.D. Williams, K. Gopinadhan, Y. Su, C.T. Cherian, J. Dix, E. Prestat, S.J. Haigh, I.V. Grigorieva, Tunable sieving of ions using graphene oxide membranes, Nature nanotechnology, 12 (2017) 546-550.

[126] J. Chong, B. Wang, K. Li, Graphene oxide membranes in fluid separations, Current Opinion in Chemical Engineering, 12 (2016) 98-105.

[127] A. Nicolaï, B.G. Sumpter, V. Meunier, Tunable water desalination across graphene oxide framework membranes, Phys Chem Chem Phys, 16 (2014) 8646-8654.

[128] H.-R. Chae, C.-H. Lee, P.-K. Park, I.-C. Kim, J.-H. Kim, Synergetic effect of graphene oxide nanosheets embedded in the active and support layers on the performance of thin-film composite membranes, Journal of Membrane Science, 525 (2017) 99-106.

[129] H.B. Park, J. Kamcev, L.M. Robeson, M. Elimelech, B.D. Freeman, Maximizing the right stuff: The trade-off between membrane permeability and selectivity, Science, 356 (2017) eaab0530.

[130] D.W. Breck, Zeolite molecular sieves, (1974).

[131] M. Pera Titus, Preparation, characterization and modeling of zeolite NaA membranes for the pervaporation dehydration of alcohol mixtures, (2006).

[132] H.C. Hu, T.Y. Lee, Synthesis kinetics of zeolite A, Industrial & engineering chemistry research, 29 (1990) 749-754.

[133] C. Catlow, A. George, C. Freeman, Ab initio and molecular-mechanics studies of aluminosilicate fragments, and the origin of Lowenstein's rule, Chemical Communications, (1996) 1311-1312.

[134] C. Baerlocher, L. McCusker, Database of Zeolite Structures: http://www.iza-structure.org/databases/, Framework Types, the information for the accesible volume Treacy, M.M.J. , in, 2017.

[135] L. Tosheva, V.P. Valtchev, Nanozeolites: synthesis, crystallization mechanism, and applications, Chemistry of Materials, 17 (2005) 2494-2513.

[136] M.E. Davis, R.F. Lobo, Zeolite and molecular sieve synthesis, Chemistry of Materials, 4 (1992) 756-768.

[137] S. Mintova, J.-P. Gilson, V. Valtchev, Advances in nanosized zeolites, Nanoscale, 5 (2013) 6693-6703.

[138] M. Jafari, T. Mohammadi, M. Kazemimoghadam, Synthesis and characterization of ultrafine sub-micron Na-LTA zeolite particles prepared via hydrothermal template-free method, Ceramics International, 40 (2014) 12075-12080.

[139] H. Wang, Z. Wang, Y. Yan, Colloidal suspensions of template-removed zeolite nanocrystals, Chemical Communications, (2000) 2333-2334.

[140] J. Grand, H. Awala, S. Mintova, Mechanism of zeolites crystal growth: new findings and open questions, CrystEngComm, 18 (2016) 650-664.

[141] M. Jafari, A. Nouri, M. Kazemimoghadam, T. Mohammadi, Investigations on hydrothermal synthesis parameters in preparation of nanoparticles of LTA zeolite with the aid of TMAOH, Powder technology, 237 (2013) 442-449.

[142] L. Perry, Understanding the property-performance relationships of membrane active layers containing porous nanoparticles, in: University of North Carolina at Chapel Hill Graduate School, 2017.

[143] A. Jawor, B.-H. Jeong, E.M. Hoek, Synthesis, characterization, and ion-exchange properties of colloidal zeolite nanocrystals, Journal of Nanoparticle Research, 11 (2009) 1795-1803.

[144] H. Wang, B.A. Holmberg, Y. Yan, Homogeneous polymer–zeolite nanocomposite membranes by incorporating dispersible template-removed zeolite nanocrystals, Journal of Materials Chemistry, 12 (2002) 3640-3643.

[145] L.B. McCusker, Product characterization by X-ray powder diffraction, in: Verified Syntheses of Zeolitic Materials, Elsevier, 2001, pp. 47-49.

[146] M.M. Treacy, J.B. Higgins, Collection of simulated XRD powder patterns for zeolites fifth (5th) revised edition, Elsevier, 2007.

[147] W. Fan, S. Shirato, F. Gao, M. Ogura, T. Okubo, Phase selection of FAU and LTA zeolites by controlling synthesis parameters, Microporous and mesoporous materials, 89 (2006) 227-234.

[148] Y. Li, S. Li, K. Zhang, Influence of hydrophilic carbon dots on polyamide thin film nanocomposite reverse osmosis membranes, Journal of Membrane Science, 537 (2017) 42-53.

[149] M. Ramiasa-MacGregor, A. Mierczynska, R. Sedev, K. Vasilev, Tuning and predicting the wetting of nanoengineered material surface, Nanoscale, 8 (2016) 4635-4642.

[150] J. Miller, S. Veeramasuneni, J. Drelich, M. Yalamanchili, G. Yamauchi, Effect of roughness as determined by atomic force microscopy on the wetting properties of PTFE thin films, Polymer Engineering & Science, 36 (1996) 1849-1855.

[151] R.N. Wenzel, Resistance of solid surfaces to wetting by water, Industrial & Engineering Chemistry, 28 (1936) 988-994.

[152] G. Hurwitz, G.R. Guillen, E.M. Hoek, Probing polyamide membrane surface charge, zeta potential, wettability, and hydrophilicity with contact angle measurements, Journal of Membrane Science, 349 (2010) 349-357.

[153] S.Y. Kwak, S.G. Jung, Y.S. Yoon, D.W. Ihm, Details of surface features in aromatic polyamide reverse osmosis membranes characterized by scanning electron and atomic force microscopy, J Polym Sci Pol Phys, 37 (1999) 1429-1440.

[154] H. Lee, S.M. Dellatore, W.M. Miller, P.B. Messersmith, Mussel-inspired surface chemistry for multifunctional coatings, science, 318 (2007) 426-430.

[155] J.H. Waite, Surface chemistry: mussel power, Nature materials, 7 (2008) 8-9.

[156] D.R. Dreyer, D.J. Miller, B.D. Freeman, D.R. Paul, C.W. Bielawski, Elucidating the structure of poly (dopamine), Langmuir, 28 (2012) 6428-6435.

[157] J. Jiang, L. Zhu, L. Zhu, B. Zhu, Y. Xu, Surface characteristics of a self-polymerized dopamine coating deposited on hydrophobic polymer films, Langmuir, 27 (2011) 14180-14187.

[158] J.r. Liebscher, R. Mrówczyński, H.A. Scheidt, C. Filip, N.D. Hădade, R. Turcu, A. Bende, S. Beck, Structure of polydopamine: a never-ending story?, Langmuir, 29 (2013) 10539-10548.

[159] Q. Wei, F. Zhang, J. Li, B. Li, C. Zhao, Oxidant-induced dopamine polymerization for multifunctional coatings, Polymer Chemistry, 1 (2010) 1430-1433.

[160] H.W. Kim, B.D. McCloskey, T.H. Choi, C. Lee, M.-J. Kim, B.D. Freeman, H.B. Park, Oxygen concentration control of dopamine-induced high uniformity surface coating chemistry, ACS applied materials & interfaces, 5 (2013) 233-238.

[161] V. Ball, D. Del Frari, V. Toniazzo, D. Ruch, Kinetics of polydopamine film deposition as a function of pH and dopamine concentration: Insights in the polydopamine deposition mechanism, Journal of colloid and interface science, 386 (2012) 366-372.

[162] F. Bernsmann, V. Ball, F. Addiego, A. Ponche, M. Michel, J.J.d.A. Gracio, V. Toniazzo, D. Ruch, Dopamine− melanin film deposition depends on the used oxidant and buffer solution, Langmuir, 27 (2011) 2819-2825.

[163] R.A. Zangmeister, T.A. Morris, M.J. Tarlov, Characterization of polydopamine thin films deposited at short times by autoxidation of dopamine, Langmuir, 29 (2013) 8619-8628.

[164] B.D. McCloskey, H.B. Park, H. Ju, B.W. Rowe, D.J. Miller, B.J. Chun, K. Kin, B.D. Freeman, Influence of polydopamine deposition conditions on pure water flux and foulant adhesion resistance of reverse osmosis, ultrafiltration, and microfiltration membranes, Polymer, 51 (2010) 3472-3485.

[165] S. Azari, L. Zou, Using zwitterionic amino acid l-DOPA to modify the surface of thin film composite polyamide reverse osmosis membranes to increase their fouling resistance, J Membrane Sci, 401 (2012) 68-75.

[166] X. Liu, J. Cao, H. Li, J. Li, Q. Jin, K. Ren, J. Ji, Mussel-inspired polydopamine: a biocompatible and ultrastable coating for nanoparticles in vivo, ACS nano, 7 (2013) 9384-9395.

[167] R.-X. Zhang, L. Braeken, P. Luis, X.-L. Wang, B. Van der Bruggen, Novel binding procedure of TiO 2 nanoparticles to thin film composite membranes via self-polymerized polydopamine, Journal of Membrane Science, 437 (2013) 179-188.

[168] Z. Yang, Y. Wu, J. Wang, B. Cao, C.Y. Tang, In Situ Reduction of Silver by Polydopamine: A Novel Antimicrobial Modification of a Thin-Film Composite Polyamide Membrane, Environmental Science & Technology, 50 (2016) 9543-9550.

[169] A. GhavamiNejad, A. Kalantarifard, G.S. Yang, C.S. Kim, In-situ immobilization of silver nanoparticles on ZSM-5 type zeolite by catechol redox chemistry, a green catalyst for A 3-coupling reaction, Microporous and Mesoporous Materials, 225 (2016) 296-302.

[170] B. Fei, B. Qian, Z. Yang, R. Wang, W. Liu, C. Mak, J.H. Xin, Coating carbon nanotubes by spontaneous oxidative polymerization of dopamine, Carbon, 46 (2008) 1795-1797.

[171] O.G. Nik, M. Sadrzadeh, S. Kaliaguine, Surface grafting of FAU/EMT zeolite with (3-aminopropyl) methyldiethoxysilane optimized using Taguchi experimental design, Chemical Engineering Research and Design, 90 (2012) 1313-1321.

[172] T.-S. Chung, L.Y. Jiang, Y. Li, S. Kulprathipanja, Mixed matrix membranes (MMMs) comprising organic polymers with dispersed inorganic fillers for gas separation, Progress in Polymer Science, 32 (2007) 483-507.

[173] I.L. Buurmans, J. Ruiz-Martínez, W.V. Knowles, D. van der Beek, J.A. Bergwerff, E.T. Vogt, B.M. Weckhuysen, Catalytic activity in individual cracking catalyst particles imaged throughout different life stages by selective staining, Nature chemistry, 3 (2011) 862-867.

[174] Y. Chevalier, C. Pichot, C. Graillat, M. Joanicot, K. Wong, J. Maquet, P. Lindner, B. Cabane, Film formation with latex particles, Colloid and Polymer Science, 270 (1992) 806-821.

[175] M.A. Winnik, Latex film formation, Current opinion in colloid & interface science, 2 (1997) 192-199.

[176] P. Steward, J. Hearn, M. Wilkinson, An overview of polymer latex film formation and properties, Advances in colloid and interface science, 86 (2000) 195-267.

[177] Ş. Uğur, M. Selin Sunay, Ö. Pekcan, Study of film formation from PS latex/TiO2 nanocomposites; Effect of latex size and TiO2 content, Polymer Composites, 35 (2014) 2376-2389.

[178] A. Khosravi, J.A. King, H.L. Jamieson, M.L. Lind, Latex barrier thin film formation on porous substrates, Langmuir, 30 (2014) 13994-14003.

[179] I. Pinnau, J.G. Wijmans, I. Blume, T. Kuroda, K.V. Peinemann, Gas Permeation through Composite Membranes, Journal of Membrane Science, 37 (1988) 81-88.

[180] J.M.S. Henis, M.K. Tripodi, Composite Hollow Fiber Membranes for Gas Separation - the Resistance Model Approach, Journal of Membrane Science, 8 (1981) 233-246.

[181] J.S. Louie, I. Pinnau, I. Ciobanu, K.P. Ishida, A. Ng, M. Reinhard, Effects of polyether-polyamide block copolymer coating on performance and fouling of reverse osmosis membranes, Journal of Membrane Science, 280 (2006) 762-770.

[182] S.A. Hashemifard, A.F. Ismail, T. Matsuura, A new theoretical gas permeability model using resistance modeling for mixed matrix membrane systems, Journal of Membrane Science, 350 (2010) 259-268.

[183] A. Ebneyamini, H. Azimi, F.H. Tezel, J. Thibault, Mixed matrix membranes applications: Development of a resistance-based model, Journal of Membrane Science, 543 (2017) 351-360.

[184] V. Freger, Nanoscale heterogeneity of polyamide membranes formed by interfacial polymerization, Langmuir, 19 (2003) 4791-4797.

[185] L. Lin, T.M. Weigand, M.W. Farthing, P. Jutaporn, C.T. Miller, O. Coronell, Relative importance of geometrical and intrinsic water transport properties of active layers in the water permeability of polyamide thin-film composite membranes, Journal of Membrane Science, 564 (2018) 935-944.